



HAL
open science

Contribution to the elaboration, experimentation and modeling of architected shape memory alloy Nickel-Titanium/silicone rubber composites

Thierry Rey

► **To cite this version:**

Thierry Rey. Contribution to the elaboration, experimentation and modeling of architected shape memory alloy Nickel-Titanium/silicone rubber composites. Civil Engineering. Université de Grenoble, 2014. English. NNT: 2014GRENI105 . tel-02023224v2

HAL Id: tel-02023224

<https://hal.science/tel-02023224v2>

Submitted on 17 May 2021

HAL is a multi-disciplinary open access archive for the deposit and dissemination of scientific research documents, whether they are published or not. The documents may come from teaching and research institutions in France or abroad, or from public or private research centers.

L'archive ouverte pluridisciplinaire **HAL**, est destinée au dépôt et à la diffusion de documents scientifiques de niveau recherche, publiés ou non, émanant des établissements d'enseignement et de recherche français ou étrangers, des laboratoires publics ou privés.

THÈSE

Pour obtenir le grade de

DOCTEUR DE L'UNIVERSITÉ DE GRENOBLE

Spécialité : **Matériaux, Mécanique, Génie Civil, Electrochimie**

Arrêté ministériel : 7 août 2006

Présentée par

Thierry REY

Thèse dirigée par **Denis FAVIER**

et codirigée par **Jean-Benoît LE CAM** et **Grégory CHAGNON**

préparée au sein du **Laboratoire TIMC-IMAG**

et de l'école doctorale **IMEP2**

Contribution to the elaboration, experimentation and modeling of architected shape memory alloy Nickel-Titanium/silicone rubber composites.

Thèse soutenue publiquement le **16 Septembre 2014**,
devant le jury composé de :

M. Gérard Rio

Professeur, Université de Bretagne-Sud, Président

M. Jean-Yves Cavallé

Professeur, INSA Lyon, Rapporteur

M. Yinong Liu

Professeur, University of Western Australia, Rapporteur

M. Patrick Terriault

Professeur, École de Technologie Supérieure de Montréal, Examineur

M. Denis Favier

Professeur, Université Joseph Fourier, Directeur de thèse

M. Jean-Benoît Le Cam

Professeur, Université de Rennes 1, Co-Directeur de thèse

M. Grégory Chagnon

Maitre de conférence HDR, Université Joseph Fourier, Co-Directeur de thèse





Acknowledgments

This manuscript represents the end of three years of works within different laboratories: 3SR followed by TIMC-IMAG as host laboratories in Grenoble, and IPR and SATIE laboratories in Rennes for several short periods. I would like to thank the members of these labs for their wonderful welcome. Thanks too to the French Research National Agency for supporting the project ANiM, and therefore this thesis.

I would also like to thank the jury members: Pr Gérard Rio to be the president of this jury and an examiner of my works, the two reporters of my PhD thesis works Pr Jean-Yves Cavallé and Pr Yinong Liu to accept this task and for their constructive reports, and finally Pr Patrick Terriault to be also an examiner of my works. Special thanks to Pr Yinong Liu and to Pr Patrick Terriault to accept to participate to the PhD defense despite the difficulties due to the jet lag in their countries (Australia and Canada respectively).

Obviously, a PhD thesis is nothing without a great supervisors team, and I think I am very lucky to be supervised by Denis Favier, Jean-Benoît Le Cam and Grégory Chagnon. Thank you for this three wonderful years, I learned a lot from you. Denis, thank you for sharing your NiTi passion and your knowledge with me. Jean-Benoît, thank you for learning me a lot about experimentation and materials science, and to be available for me despite the distance. Thank you too for your wonderful welcome when I came to Rennes, I will not forget this delicious kouign amann of S^t Malo. Grégory, thank you for learning me a lot about modeling and implementation. Your availability and help were very important for my thesis, and I want to thank you for your presence for me all the time.

Many thanks too to the members of the research team (BioMMat), for the fruitful scientific discussions and for the good times out of work with the "cachalot" team. I shared my office with a lot of other PhD student of the team during this thesis: Adeline, Camille, Christopher, Dung, François, Gabriel and Quentin. Thanks to them for the great ambiance in the different offices I had during these three years. But I don't forget for the good ambiance of the team the other team members: Denis, Grégory, Guilherme, Nathanaël, Stephanie, Thierry and Vincent. And obviously, Marie, who supported me during these three years, and who share with me more than our PhD theses.

Special thanks too to Gabrielle Michalowicz for sharing her office with me during a few months when the team BioMMat came to the laboratory TIMC-IMAG, and to Pierre-Yves for his continuously good humour.

I would also like to thank the members of the two laboratories in Rennes who worked with me, Éric, Florence, Pierre and Sylvain. I would also acknowledge Mei Sze Loo for fruitful discussions and valuable suggestions.

I don't forget too my friends, Anthony, Caroline, David, Jean, Jean-Loup and Mathieu, with whom I shared very good times during these three years.

Finally, I would to thanks my parents and sisters for always supporting me.



Abstract

Shape memory alloys Nickel-Titanium are well known for their superelastic properties associated with a martensitic elastic transformation, ferroelasticity due to the reorientation of martensite and finally shape memory effects. The properties of architected NiTi materials, such a knitted NiTi, cellular materials, depend on the constituting NiTi and of the geometry. The study deals with architected composite materials made of architected NiTi materials and silicone rubber elastomer. Such materials present numerous different properties, depending on the constituting materials and also on the interfaces and the topology.

The first part of the study focuses on the interface between NiTi and silicone rubber. Among the tested solutions, plasma treatments were especially studied. The influence of treatment parameters on the interface resistance was firstly investigated by means of pull-out tests carried out on NiTi wires embedded in a silicone rubber matrix. Optimized parameters for plasma treatment were then applied in order to elaborate a tubular architected material made of knitted NiTi and silicone rubber. The mechanical behavior of this composite was characterized by means of tensile and swelling tests.

The second part of the study deals with silicone rubber behavior. Experiments were performed in order to evaluate the influence of temperature on the mechanical behavior of silicone rubbers, especially on the stress softening (Mullins Effect), mechanical hysteresis and stress relaxation. A model taking into account the mechanical hysteresis was then proposed. Based on numerous works in the field of rubber mechanics, the approach used a decomposition of the space in a finite number of directions. A monodimensional constitutive equation including hysteresis effects is written for each direction. This model was implemented in a finite elements software (ABAQUS) and was tested with structure simulations.

In the third part of the study, the previous formalism was used model the mechanical behavior of NiTi, only In case of superelasticity. The results of the simulations carried out are in good agreement with those reported in the literature for tests on isotropic and anisotropic NiTi plates, which highlights the great interest of such an approach.



Contents

Contents	i
Introduction	1
1 Development of an architected NiTi/silicone rubber composite	3
1.1 Improvement of the interface NiTi/silicone rubber	3
1.1.1 Introduction	4
1.1.2 Materials and methods	5
1.1.3 Results and discussion	9
1.1.4 Conclusion	16
1.2 Elaboration of a tubular architected composite	16
1.2.1 Introduction	17
1.2.2 Experimental setup	18
1.2.3 Results and discussion	22
1.2.4 Conclusion	26
1.3 Conclusions of the chapter	27
2 Influence of the temperature on the mechanical behaviour of filled and unfilled silicone rubbers	29
2.1 Introduction	30
2.2 Experimental setup	30
2.2.1 Preparation of the silicone rubbers	30
2.2.2 DSC and DMTA analyses	31
2.2.3 Mechanical tests	33
2.3 Tests results	36
2.4 Discussion	40
2.4.1 Modeling of temperature dependency of the mechanical response . .	40
2.4.2 Mullins effect	41
2.4.3 The mechanical hysteresis	42

2.5	Conclusions	44
2.6	Conclusions of the chapter	46
3	Hyperelasticity with rate-independent microsphere hysteresis model for rubberlike materials	47
3.1	Introduction	48
3.2	Experimental setup	49
3.2.1	Materials	49
3.2.2	Loading conditions	49
3.2.3	Experimental results	50
3.3	Theory	53
3.3.1	Motivation	53
3.3.2	Decomposition of the material behavior	53
3.3.3	Hyperelastic part	53
3.3.4	Hysteresis part	54
3.4	Results and discussion	58
3.5	Extension of the model	62
3.5.1	Finite element implementation	62
3.5.2	Higher hysteresis simulation	63
3.6	Conclusions	66
3.7	Conclusions of the chapter	67
4	A directional approach to model superelastic behavior of NiTi Shape Memory Alloy (SMA)	69
4.1	Introduction	69
4.2	Standard elasto-plasticity model	70
4.2.1	Monodimensional elasto-plastic model	70
4.2.2	3D elasto-plasticity theory	73
4.3	Model of superelasticity	80
4.3.1	Deformations mechanisms	80
4.3.2	1D modeling of the transformation contribution	81
4.3.3	Modeling of the plasticity of SMAs	82
4.3.4	Monodimensional simulations	83
4.3.5	3D modeling of the superelasticity of SMAs	84
4.4	Simulation of an experimental result of the literature	86
4.5	Conclusions	87
	Conclusion and perspectives	89
	A Tensile tests perfomed on NiTi silicone rubber composite	91
	Bibliography	95



Introduction

The present PhD thesis has been carried out in the framework of a project funded by the Research National Agency. This project brings together several laboratories in France and Australia. It is devoted to architected materials made of NiTi wires or tubes, like balls of yarn or honeycombs, and to propose numerical solutions to simulate the behavior of these structures. It addresses numerous issues, among them the elaboration of architected NiTi silicone rubber composites.

Architected materials are increasingly used in many fields, for instance for stents in the biomedical field, plane wing in the aeronautic field or carbon-fiber composite in the automotive field. Materials can be architected by different ways; by modifying their microstructure [Brecht and Embury, 2013], like wood or bone [Dunlop and Fratzl, 2013], by means of particular geometries, such as crenelated silicone membranes [Rebouah and Chagnon, 2014] or porous metallic alloys [Brailovski *et al.*, 2011]. An architected composite can also be elaborated by assembling materials whose shapes are different.

The typical properties of Shape Memory Alloys (SMAs) Nickel-Titanium (NiTi) make them very interesting to elaborate architected materials or composites [Otsuka and Ren, 2005]. Indeed, an initial shape can be given to SMAs by applying an appropriate heat treatment, which offers numerous design possibilities. Moreover, it undergoes relatively large strains (for a metallic material) and can react to several modes of loading (mechanical, thermal or electrical). Finally, the biocompatibility of the NiTi alloy explains its increasing use in the biomechanic field. However, some applications, especially in the biomedical field, need to isolate the NiTi from its external environment. Typically, a NiTi textile introduced in the human body could be damaged by the surrounding tissues. To avoid it, this PhD thesis aims at elaborating a composite made of architected NiTi embedded in a silicone rubber matrix. Such a composite exhibits particular properties: it is a 'soft' structure, it undergoes large deformations, and it could be biocompatible using a suitable silicone rubber and interface treatment.

Nevertheless, the adhesion at the interface of these two materials is a current challenge in order to optimize the behavior of such a composite. This explains why many investigations about the adhesion between both materials were carried out during this PhD thesis, especially by applying surface treatments to the NiTi. Moreover, the mechanical behavior

of the NiTi strongly depends on the temperature. It should be noted that temperature variations also alter the mechanical behavior of silicone rubber and this effect has therefore to be characterized. Also, in order to simulate the mechanical behavior of such a composite and to predict its mechanical response, well-known phenomena exhibited by both the materials have to be taken into account in models. Among these phenomena, the mechanical hysteresis, defined as the difference between the mechanical response between loads and unloads, is observed for both materials. Thus, modeling this phenomenon in the both materials (NiTi and silicone rubber) is a current challenge to predict the mechanical response of such a composite.

Chapter 1 of this PhD thesis investigates the interface between NiTi and silicone rubbers. For this purpose, a device was developed in order to characterize the mechanical resistance of the interface between these materials, and several methods were tested to improve their adhesion. Once the adhesion was ensured, an architected NiTi/silicone rubber tubular composite was elaborated and mechanically tested by means of bulge tests. Results are presented and discussed in this chapter. This chapter corresponds to the papers entitled "Mechanical characterization and comparison of different NiTi/silicone rubber interfaces", which has been published in *International Journal of Adhesion & Adhesives* in 2014 and "An original architected NiTi silicone rubber structure for biomedical applications", which have been submitted for publication in *Materials Science and Engineering: C*.

Chapter 2 investigates the influence of the temperature on the mechanical behavior of silicone rubbers. DSC and DMTA were performed on two silicone rubbers (filled and unfilled) in order to determine their characteristic temperatures. Mechanical tests were performed above their crystallization temperature. Influence of the temperature on their mechanical behavior was then analyzed and discussed. This chapter corresponds to the paper entitled "Influence of the temperature on the mechanical behaviour of filled and unfilled silicone rubbers", which has been published in *Polymer Testing* in 2013.

Chapter 3 presents a model that accounts for the rate-independent mechanical hysteresis of silicone rubbers. This phenomenon was observed with the silicone rubber studied in the range of strain rates investigated. A directional approach was adopted for this model and the hysteresis loops was modeled by using the concept of inversion points. This chapter corresponds to the paper entitled "Hyperelasticity with rate-independent microsphere hysteresis model for rubberlike materials", which has been published in *Computational Materials Science* in 2014.

A model of superelastic behavior of NiTi is proposed in chapter 4. A monodimensional elasto-plasticity model is firstly presented, and an extension to the modeling of the superelastic behavior of SMAs is then proposed. The same formalism than for the model developed for rubberlike materials was used to extend this monodimensional model to a tridimensional modeling, by a directional approach.

Development of an architected NiTi/silicone rubber composite

This chapter deals with the elaboration of an architected NiTi/silicone rubber composite and its mechanical characterization. The properties of such a composite depend on both the constitutive materials and the interface between the materials. Hence, the adhesion between the two constitutive materials is an important issue. The first part of the present chapter deals with the mechanical characterization and improvement of the adhesion between NiTi wire and silicone rubber. This study has been published in International Journal of Adhesion & Adhesives [Rey *et al.*, 2014b]. The results obtained enabled us to choose an adhesion method based on plasma treatment suitable to biomechanical applications. The second part of the chapter deals with the optimization of the plasma treatment in order to improve the mechanical resistance of the interface between NiTi and silicone rubber. A tubular composite was then elaborated and tested by means of bulge tests. This part of the chapter has been submitted for publication in Materials Science and Engineering: C [Rey *et al.*, 2014c]. It should be noted that the tubular composite was first tested under classical cyclic uniaxial tensile conditions. The results are reported in appendix A.

1.1 Improvement of the interface NiTi/silicone rubber

T. Rey, F. Razan, E. Robin, S. Faure, J.-B. Le Cam, G. Chagnon, A. Girard, D. Favier
Published in International Journal of Adhesion & Adhesives 48 (2014) 67-74.

This paper investigates the effects of different surface treatments on the mechanical resistance of interface between wires of NiTi shape memory alloy and silicone rubber. Three different treatments were used; primer, plasma and combination of both. The wires deoxidation effects have also been studied. In order to characterize the interface properties in such composite material, pull-out tests were carried out by means of a home-made device. This test allows us to evaluate the mechanical resistance of the interface in terms of the maximum force reached during the test. First, results show that the debonding force is not higher after the wires deoxidation. This preparation is therefore not necessary. Second, using a primer PM820 and plasma separately leads to a significant improvement of the

mechanical resistance. Third, the combination of these treatments (primer followed by plasma) and a longer time of exposure to the plasma alone get the debonding force higher. Consequently, NiTi/silicone rubber interface improved only by means of plasma offers a new way to obtain biocompatible interfaces in such composite material.

1.1.1 Introduction

Shape Memory Alloys (SMA) and more specifically Nickel-Titanium (NiTi) are increasingly used in many applications due to their typical behavior, *i.e.* their superelasticity and their shape memory behavior. This type of materials undergoes relatively large deformations of about 10% without exhibiting any plasticity in the pseudoelastic domain [Favier *et al.*, 2006]. It allows large deformations too in its shape memory form, but a permanent deformation is observed. In the latter case, it can return to its initial shape by heating. The properties of shape memory alloys can be activated either by mechanical or thermal loadings, that explains their large use, especially in the biomedical field and in the aerospace. New categories of innovative materials can be developed by combining the intrinsic properties of these SMA with purposely engineered topologies [Machado *et al.*, 2013] or with intrinsic properties of other materials such as polymers [de Araùjo *et al.*, 2008] or elastomers [Tissot *et al.*, 2012]. To realize these unique structures, innovative materials processing techniques are applied such as electrical resistance welding to link NiTi tubes [Delobelle *et al.*, 2013], or embedding of NiTi in a polymer matrix [Neuking *et al.*, 2005].

The efficiency of these composites strongly depends on the adhesion between the NiTi and the polymer matrix. Some investigations to improve this adhesion have already been reported in the literature. They highlight that numerous treatments can change the quality of the interface. Neuking *et al.* [2008] observed that the adhesion between NiTi wires and a thermoplastic polymer can be improved by a combination of mechanical, physical and chemical surface treatments. Smith *et al.* [2004] showed the efficiency of silane coupling agents to improve the interface between NiTi wires and a PMMA matrix. For NiTi/epoxy composites, Jonnalagadda *et al.* [1997] showed that the debonding force can be significantly increased by sandblasting the NiTi wires. This treatment is efficient but not suitable for all applications, typically for very little NiTi specimens, due to the sand particles size. In Lau *et al.* [2002], NiTi wires were twisted and next embedded in an epoxy matrix. The geometrical changes and the increase of roughness (by mechanical breaking of the surface oxide film of the wire due to the twisting process) increase the bonding strength. Once again, this treatment seems to be efficient, but it is only possible for the use of wires, and an unrecoverable strain can appear on the wires in the case of a too great number of turns.

Even though numerous studies were carried out on NiTi/polymer interfaces, the interface between NiTi and a silicone rubber has rarely been investigated. Nevertheless, a main result has already been obtained: the interface is improved by acid etching and oxidizing the NiTi wires [Sadrnezhad *et al.*, 2009]. This NiTi/silicone rubber association is often used, as example for smart structure applications [Heller *et al.*, 2012] or for actuators [Garner *et al.*, 2000; Chemisky, 2009]. The interface between silicone rubber and other materials has also been studied. In Chang *et al.* [2009], a primer was used to improve

the adhesion between polyurethane and silicone. In Hauser *et al.* [2009], an argon-oxygen plasma was used to improve adhesion between collagen and silicone.

This paper aims therefore at investigating the interface NiTi/silicone rubber. The materials and devices are presented in section 1.1.2. In section 1.1.3, results obtained from different treatments on the NiTi wires are presented. More precisely, the effects of deoxidation of NiTi wires and the differences between interfaces made with adhesion promoter and plasma treatment are discussed related to the maximum force reached during mechanical tests. Finally, concluding remarks close the paper.

1.1.2 Materials and methods

1.1.2.1 Materials

Wires of commercial pseudoelastic NiTi (with a Ni content of 50.8 at.%) shape memory alloy were used. The diameter of the wires is 0.5 mm. The characteristic temperatures of this material were identified by means of a DSC (Differential Scanning Calorimetry), using a TA Q200 differential scanning calorimeter. It consists in a cooling between 120°C and -90°C followed by a heating between -90°C and 120°C. Cooling and heating rates were set at 10°C per minute. A specimen of 20 mg weight was used. The results of the DSC analysis are presented in Fig. 1.1. Two peaks are observed. They correspond

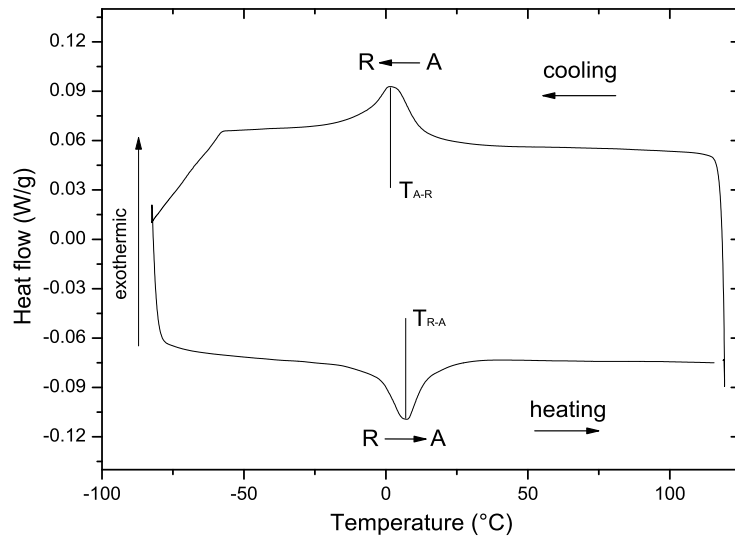


Figure 1.1: DSC analysis of the NiTi wire.

to the austenite (A) to rhombohedral (R) phase transformation (A to R) during the cooling and the reverse transformation (R to A) during the heating. These peaks are interpreted as the A to R and reverse transformations and not as austenite to martensite (M) phase (and reverse) transformation because the small difference between the two peaks ($T_{R-A} - T_{A-R} \approx 10^\circ\text{C}$) and the low latent heats (about 3 J/g) are representative of the A to R and reverse transformations [Favier and Liu, 2000]. The R to M phase transformation (and its reverse) is not visible in the DSC, meaning that the temperature of the R to M transformation is lower than -90°C .

A curve of a classical load-unload tensile test of the NiTi at room temperature is presented in Fig. 1.2. This curve presents a first elastic part, followed by a plateau

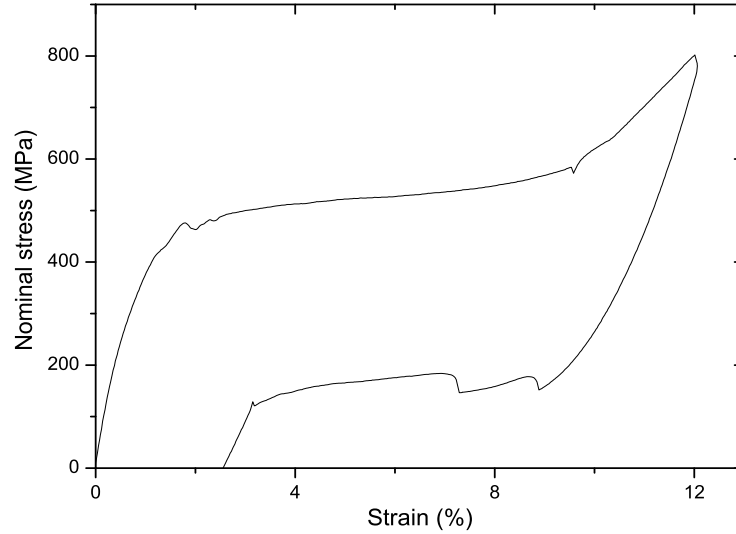


Figure 1.2: Load-unload tensile test on a NiTi wire at room temperature.

corresponding to a phase transformation (A to M), and an elastic response of martensite phase. A hysteresis loop is observed, as the level of the plateau is different during load and unload.

The polymer matrix considered here is a filled silicone rubber (Bluestar RTV 3428). The mechanical and thermal properties of this material were previously investigated in Machado *et al.* [2012]; Rey *et al.* [2013a]. Its crystallization and melting temperatures were identified by a DSC (cooling and heating rates: 2°C per minute) at -66°C and -41°C respectively, and the glass transition temperature is lower than -90°C [Rey *et al.*, 2013a]. The material exhibits a hyperelastic behavior and undergoes high strain levels. Moreover, numerous phenomena take place during its deformation. Results of a tensile test with two load-unload cycles are presented in Fig. 1.3. A stress softening is observed between first and second loads, corresponding to the Mullins effect [Mullins, 1948]. Moreover, a difference between the mechanical response during loads and unloads is observed, it is the mechanical hysteresis. Finally, a little residual elongation is observed after unloading.

A PM820 primer from Bluestar Silicone is used in some cases as an adhesion promoter. It is recommended by Bluestar Silicone to improve the adhesion between a metallic surface and an elastomer.

1.1.2.2 Samples preparation

A home-made mold was designed to ensure the NiTi wire to be located in the center of the silicone rubber pancake. Moreover, the mold enables to control the thickness of the silicone specimen, as illustrated in Fig. 1.4 a). The dimensions of the pancake composite are given by the schematic diagram in Fig. 1.4 b). Once the treated wire was put in the mold, the silicone, which was previously blended with its curing agent and degassed to remove air bubbles, was injected by the way of a medical syringe. Then, the mold was put in an oven for 4 hours at 70°C for the silicone curing.

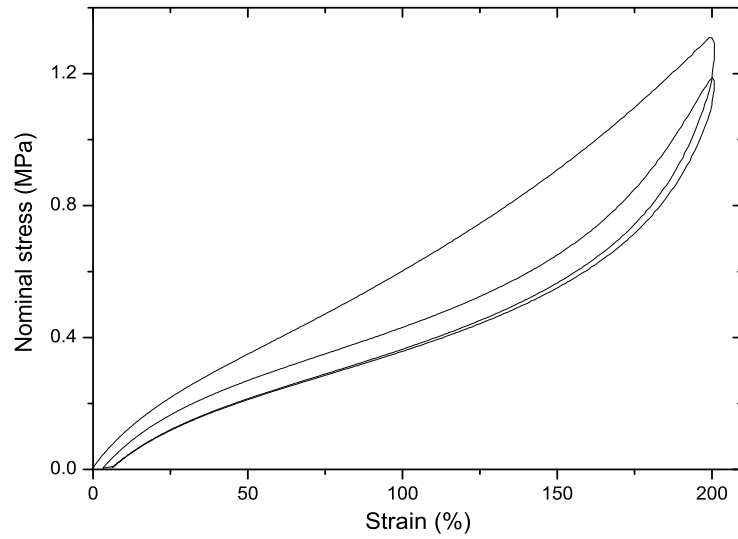


Figure 1.3: Load-unload tensile test (two cycles) on a RTV 3428 silicone rubber at room temperature.

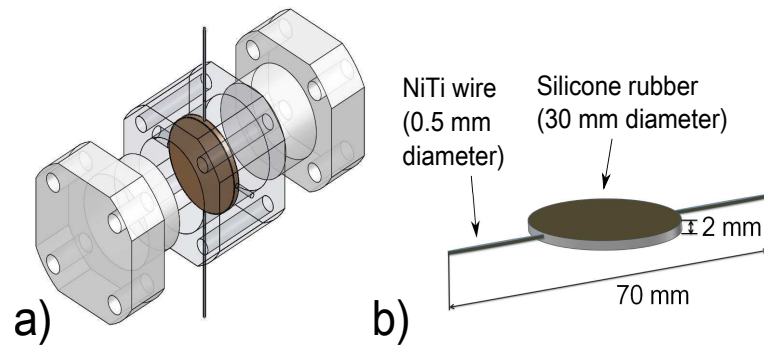


Figure 1.4: Elaboration of the NiTi-silicone composite. a) Home-made mold for elaboration and b) scheme of the NiTi-silicone specimen with dimensions.

1.1.2.3 Surface preparations

The NiTi wires were treated with different techniques: primer, plasma, and combination of both. In order to determine whether oxides at the wire surface affect the interface resistance, a chemical attack is performed to remove the oxides. It consists in immersing the wire in a chemical solution ($1\text{HF}+4\text{HNO}_5+5\text{H}_2\text{O}$) during 50 s, and then cleaning it within distilled water. The aim of this preparation is not really considered as one specific treatment such as primer or plasma, but a cleaning of the wire surface.

The first treatment carried out to improve the mechanical resistance of the interface was the application of a thin and uniform coat of the adhesion promoter previously presented. It was applied with a suitable brush. The second treatment corresponds to plasma, with air as working gas. This treatment is performed with a Harrick Plasma Cleaner equipment in clean room and under vacuum set at 10^{-3} mbar. During the treatment, the power was set at 30 W and the exposure time was set either at 600 s or at 1800 s (in the following, it will be precised when the time of plasma is 1800 s). Plasma treatments were already used with NiTi but not in air, for example the modifications of the NiTi surface by air/ H_2

plasma and oxygen plasma were studied in Ju and Dong [2006] and Tan and Crone [2002] respectively. The use of this treatment to improve interfaces adhesion was already carried out, as in Ting *et al.* [2013] between steel surfaces and an epoxy matrix, using O₂/Ar microwave plasma treatment.

1.1.2.4 Pull-out tests

Pull-out tests were performed to quantify the adhesion between the NiTi wire and the polymer, as classically done in the litterature [Neuking *et al.*, 2008; Smith *et al.*, 2004; Lau *et al.*, 2002; Sadrnezhad *et al.*, 2009], because adhesion strength increase is linked to the increase of the required force to start the debonding.

These tests were carried out using a Instron 5543 testing machine, which load cell capacity is 1 kN. A second load cell, which capacity is 250 N, was also used.

Fig. 1.5 shows the experimental device. As the polymer matrix of the studied com-

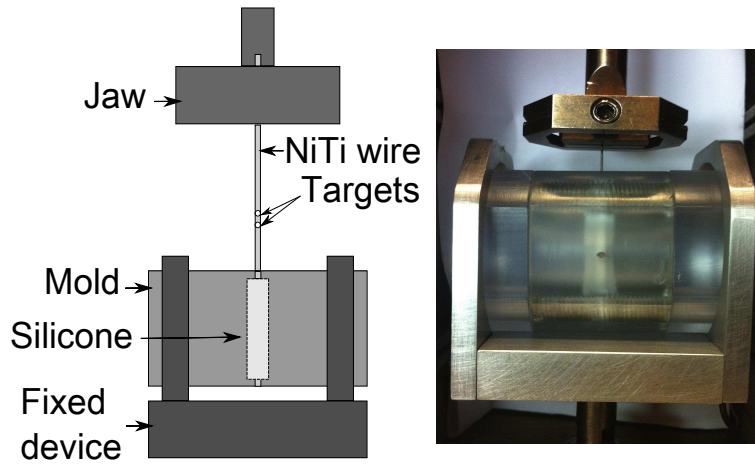


Figure 1.5: Pull out device.

posite is a soft material, its displacements during the pull-out test can alter the measured adhesion strength. That is why the sample was left in the mold during the test. The mold was mounted in a home-made device, which avoids the translations but allows the mold to rotate. Thus, no flexion is induced in the wire at the beginning of the test. The wire was gripped in a jaw to be pulled out in the vertical direction, at room temperature with a displacement speed of 0.6 mm/s.

1.1.2.5 Measurement of the wire deformation

In order to measure wire deformation during the tests, a marks tracking method was used. This method, which is based on image processing technique, allows us to track automatically the position of each marks painted at the wire surface. The position of each mark barycenter is given by:

$$\begin{cases} x_g = \frac{\sum_i x_i (I_i - I_s)}{\sum_i (I_i - I_s)} \\ y_g = \frac{\sum_i y_i (I_i - I_s)}{\sum_i (I_i - I_s)} \end{cases} \quad (1.1)$$

where I_i is the grey level of the pixel, whose coordinates are (x_i, y_i) , and I_s is the threshold value, from which the pixels of markers are distinguished [Chean *et al.*, 2011]. Fig. 1.6 illustrates the

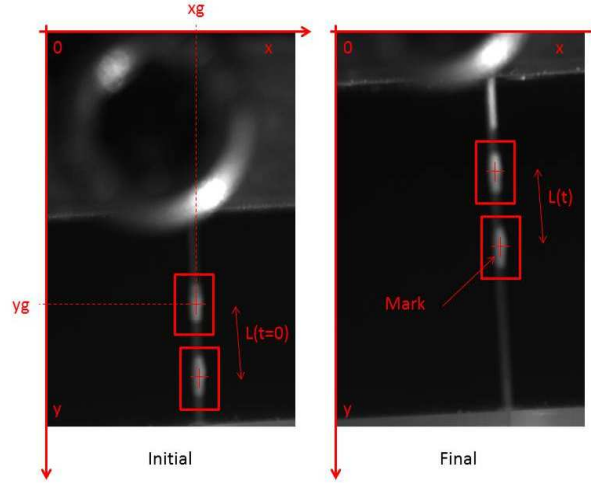


Figure 1.6: Pictures illustrating the marks tracking method.

1.1.2.6 Scanning Electron Microscopy

In order to examine the wire surfaces after extracting it, scanning electron microscopy (SEM) was carried out with a JEOL JSM 6301F. An energy dispersive spectrometer of X-rays (EDSX), coupled with a JEOL JSM 6400 microscope, was used to determine the chemical elements on fracture surfaces.

The aim of such analyzes is to compare the effects of different treatments on the interface resistance at the microscopic scale.

1.1.3 Results and discussion

The mechanical results, SEM observations and EDSX analysis are presented and discussed in this section.

1.1.3.1 Untreated and deoxidized wires

Fig. 1.7 a) presents the SEM observation of untreated NiTi wire surface. The surface observation highlights that surface is composed of grains, which differ in shape and in size. Voids, which appear in black color, are observed between grains. EDSX analysis of untreated (Fig. 1.8 a) and deoxidized (Fig. 1.8 b) wire surface confirms the higher amount of oxides in case of untreated wire surface. SEM observations of a deoxidized wire are presented in Fig. 1.7 b). Significant change in the wire surface is observed. Indeed, grains and voids in between are not observed any more, and the surface is composed of cups with different dimensions. The surface is less regular than the previous one, which should promote physical interactions with the rubber matrix.

Fig. 1.9 presents the results of the pull-out test for an untreated and a deoxidized wire. Debonding occurs for small jaw displacement, with a small force. This debonding force

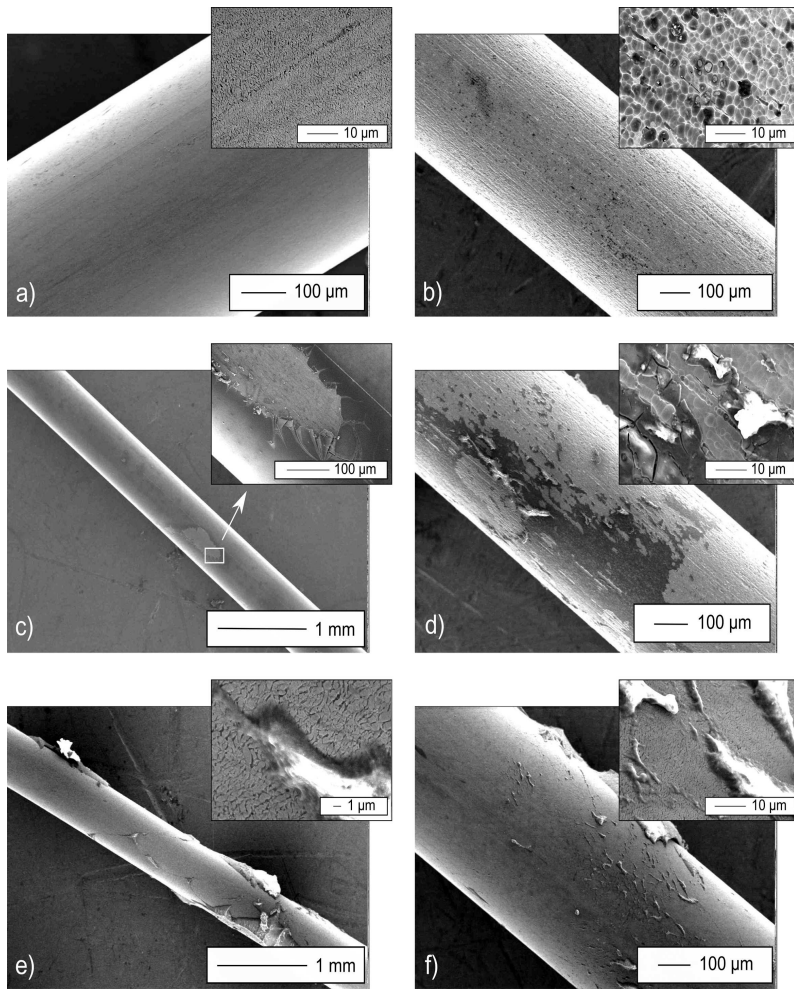


Figure 1.7: Observations of the pulled out wires a) without any treatment, b) deoxidized, c) with a primer, d) deoxidized with a primer, e) treated with a plasma and f) with a primer and a plasma treatment.

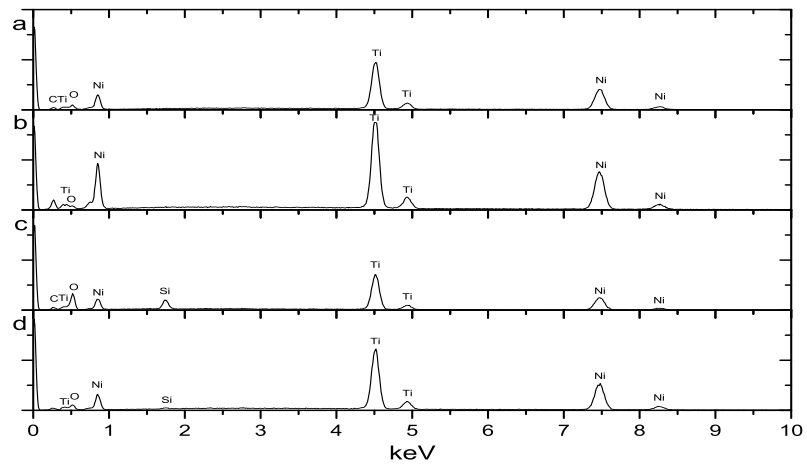


Figure 1.8: EDSX analysis of a wire a) without any treatment, b) deoxidized, c) with a primer and d) treated with a plasma.

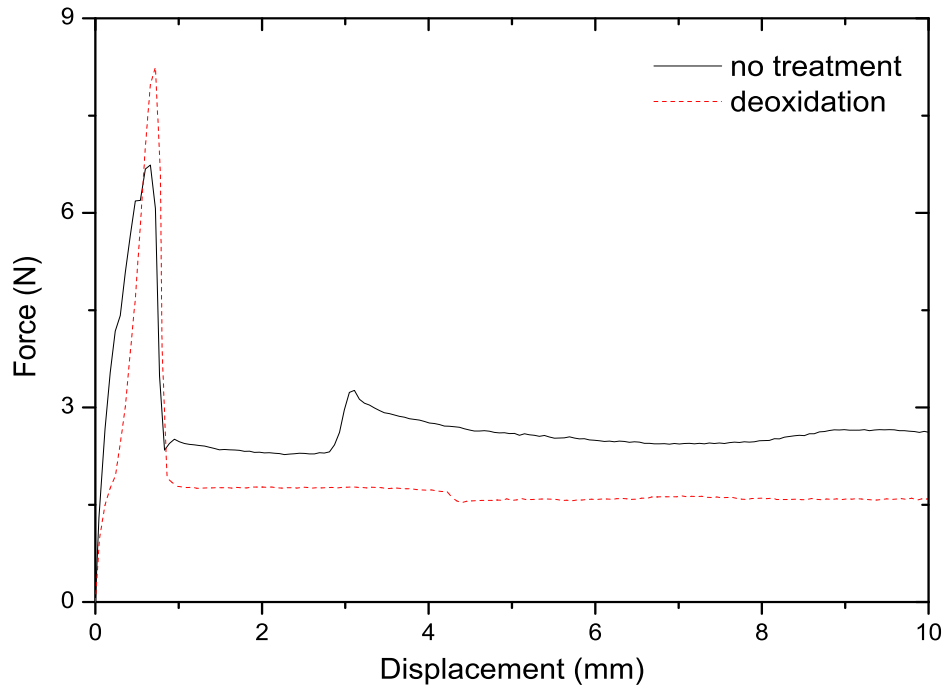


Figure 1.9: Results of a pull out test with an untreated and a deoxidized NiTi wire.

in the case of a deoxidized wire is slightly higher than that of the untreated wire (about 8 N for the first one against about 7 N for the second), but the improvement is not very significant here. The deoxidation of the wire is therefore not necessary to promote the interface properties. After reaching the debonding force, a residual force is measured. It corresponds to the force required to finish the wire extraction. It is due to the friction between the NiTi wire and the silicone rubber matrix.

1.1.3.2 Use of an adhesion promoter

The adhesion promoter previously presented is used here to improve interface properties between the NiTi and the silicone matrix. The EDSX analysis of a wire with a primer coat is presented in Fig. 1.8 c). It shows that this adhesion promoter is principally composed of silicon and oxygen, which allows silicone rubber and NiTi to be chemically linked. Indeed, the efficiency of silane (composed too of silicon and oxygen) coupling primers to improve the adhesion in an elastomer-metal interface was already investigated in the literature, as for example in Golaz *et al.* [2011].

The results of the pull-out test are presented in Fig. 1.10 for wires deoxidized or not using the primer, and compared to the results with an untreated wire. The maximum force required to extract the wire of the rubber matrix (55 N) is about eight times higher than previously (7 N), regardless if the wire is deoxidized or not. Moreover, the displacement needed for the debonding is also larger. The curve of the deoxidized and not wires are almost similar, even if the maximum force is a bit higher for an untreated wire using primer. The pull-out curves present some singularities. Firstly, the evolution of the curve is not the same at the beginning of the test (for a displacement between 0 and 0.5 mm) than in the following. The fact that no pre-stress is applied to the test device before

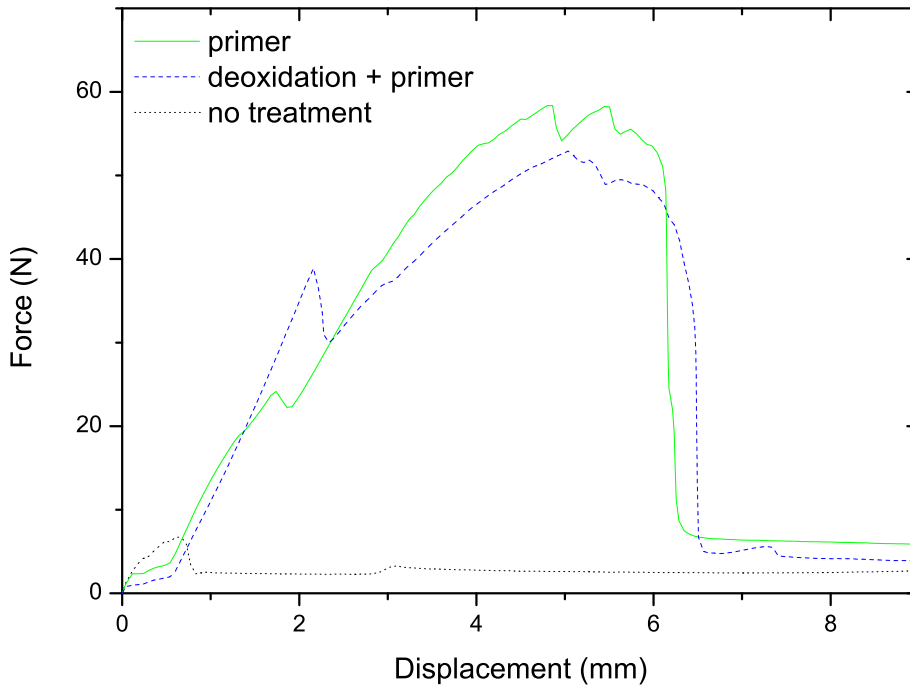


Figure 1.10: Effect of the adhesion promoter on the interface NiTi/silicone rubber.

the test explains this difference. The device and the specimen have a slight out-of-plane displacement. Secondly, a first peak is observed on the force-displacement curve for a displacement about 2 mm. This phenomenon is often observed in the literature for pull-out tests with NiTi wires. The interpretation of a sliding at the interface is proposed in Sadrnezhad *et al.* [2009] to explain the first singularity of the curve. The phase changes are raised in Smith *et al.* [2004] to interpret this phenomenon as an elbow and in Hamming *et al.* [2008] to justify the numerous peaks in the curve. The transformation possibilities of a pulled out SMA fiber are also put forward in Wang and Hu [2005], and the effects of the martensitic transformation on a NiTi/polymer composite behavior are investigated in Payandeh *et al.* [2012]. In the present study, the deformation of the pulled-out wire was determined by the target tracking performed during the test. The results of the measured stress versus the deformation of the wire, until the debonding, are plotted on a strain-stress curve and compared to a NiTi wire subjected to a load-unload uniaxial tensile test in Fig. 1.11. The strain-stress curve of the pulled-out wire is similar to the uniaxial tensile one, and it can be observed that the strain (0.75 %) and stress (295 MPa) levels reached are clearly not enough to induce a phase transformation (1.76 % and 475 MPa respectively). The peak on the pull-out curves in Fig. 1.10 is therefore not explained by a material phase transformation, and seems rather to be a first sliding at the interface of the composite in our case. It is to note that target tracking and study of the wire deformation was done for each test but are not reported in the paper, as the strain and stress never reached the level necessary to start the martensitic transformation.

SEM observations of the extracted wire with primer are shown in Fig. 1.7 c). Even though no silicone rubber was observed on the wire surface, the coat of primer is almost unaltered, excepted a hole where the primer has been extracted. Cracks due to this

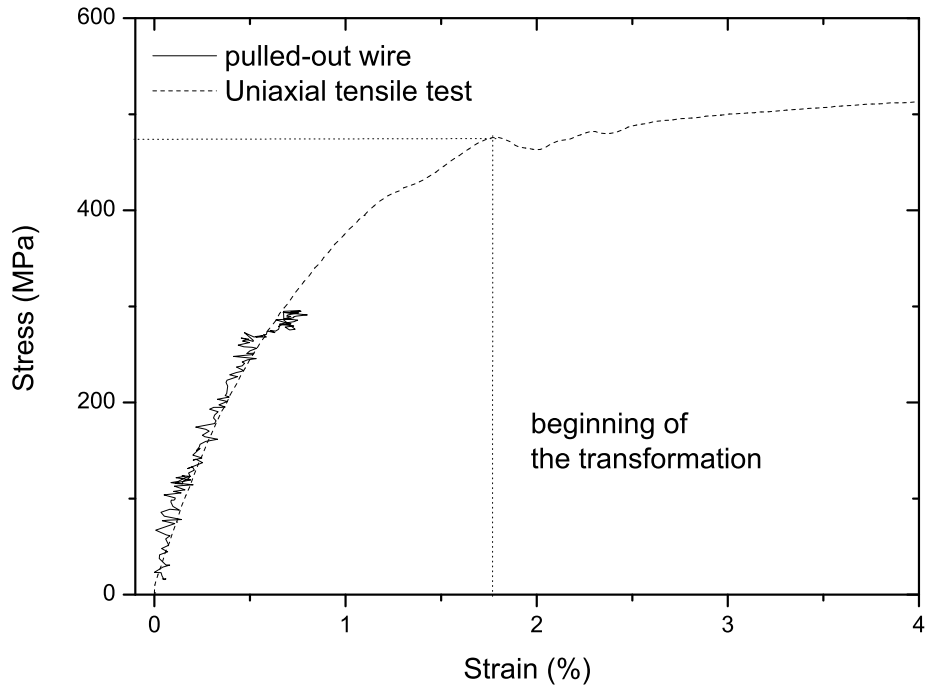


Figure 1.11: Deformation of the NiTi wire during the pull out test with a primer treatment, compared to a load-unload cycle of a NiTi wire.

extraction do not propagate. So the interface between wire and primer is stronger than that between the primer and the silicone rubber matrix as no silicone rubber is remained on the primer coat. Nevertheless, the primer coat is lower in the case of a deoxidized wire as shown in Fig. 1.7 d). A great part of this coat was extracted and stayed in the silicone matrix. The irregularity of the surface of the deoxidized wire leads to a non-uniformity in the primer coat thickness. This leads to crack occurrence in the primer coat, which makes it less efficient.

1.1.3.3 Plasma treatment

Fig. 1.12 presents the results of the pull-out tests using a plasma treatment. Once again, the force required to reach the complete debonding (50 N) is much higher than without treatment (7 N). As for the use of primer, curves exhibit a first peak before increasing again, until reaching the maximum debonding force. As observed previously, results with a deoxidized wire is a little lower than plasma on untreated wire, that is why no more tests are carried out with deoxidized wires.

A wire treated with plasma and extracted from the polymer matrix was observed by SEM (Fig. 1.7 e)). A few silicone rubber patches were observed on the wire surface, meaning that some cohesive failures take place in the material before adhesive failure at the interface. The boxed zone magnification in Fig. 1.7 e) shows that no difference in the surface morphology is observed between wire with plasma treatment and untreated wire. Moreover, EDSX analysis (Fig. 1.8 d)), carried out on a part of the wire surface with silicone rubber, does not allow us to detect any changes in the chemical composition of the pulled wire surface.

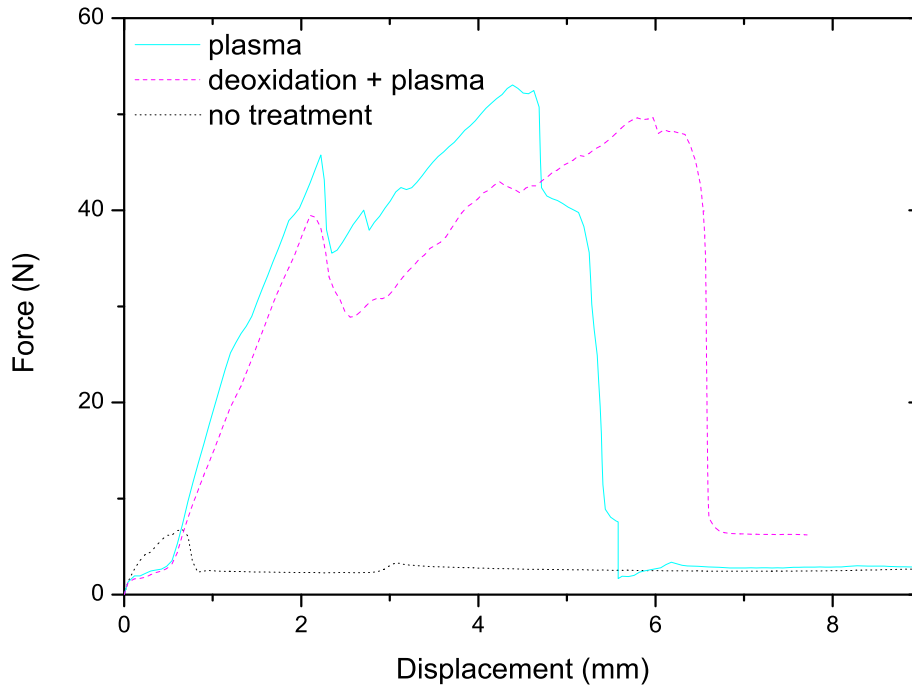


Figure 1.12: Plasma treatment effect on the NiTi/silicone rubber interface.

1.1.3.4 Toward an improvement

The two treatments previously applied have shown efficient results to improve mechanical resistance of the interface. In this section, an additional improvement is researched using these methods. Numerous possibilities exist and it is not possible to cover all of them in the present paper. Here, two methodologies were chosen. The SEM analyzes have shown that using a primer no silicone rubber remains on the primer coat after wire extraction, meaning that the primer-silicone interface was of low resistance. This is why the first method chosen is the application of a plasma treatment on a coat of primer applied on a wire. The second method chosen is a change of the parameters of the plasma treatment, more especially exposure time. Here, the wire is exposed to the plasma during 1800 s against 600 s previously, using the same device. Results of the pull-out tests are presented in Fig. 1.13. They are quite similar between the two treatments: the level of the first peaks (45 N) and of the maximum forces (about 80 N) are almost the same. The required force and displacement to obtain the complete debonding are very high (more than ten times superior than without treatment), which proves the efficiency of these treatments.

SEM observations of the extracted wire treated with a primer followed by a plasma are shown in Fig. 1.7 f). The primer coat remains at the wire surface, but some silicone rubber patches are observed, which is in good agreement with the improvement of the primer-silicone rubber interface. The observations carried out on the wire treated with plasma and extracted are not represented here as no difference was observed with the first plasma treatment, *i.e.* a few silicone rubber patches are staying on the wire surface and the microstructure of this one is similar to a untreated wire.

In order to compare and to summarize the results, two diagrams are built. As wire deoxidation does not influence the results, the corresponding results are not represented

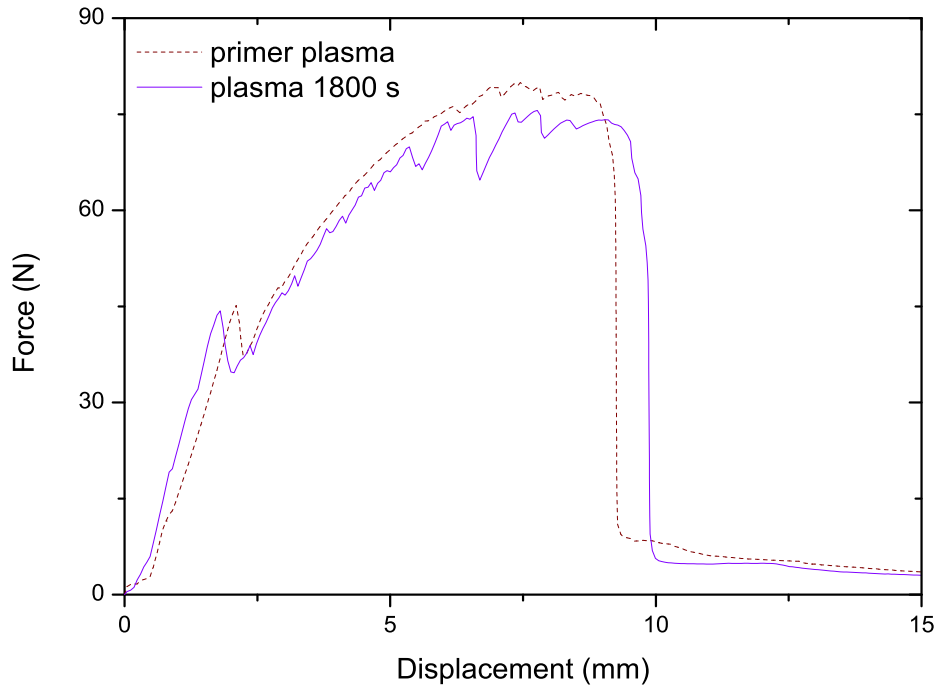


Figure 1.13: Effect of a longer time plasma and of primer + plasma on the interface NiTi/silicone rubber.

in these diagrams. In Fig. 1.14, the maximum forces reached during pull-out tests are plotted. The primer followed by plasma treatment exhibits the higher debonding force

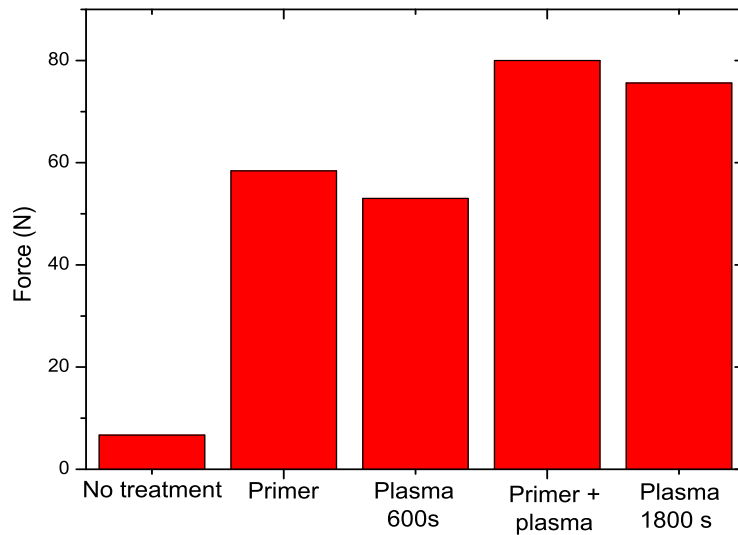


Figure 1.14: Maximum force values obtained during a pull out test.

(about 80N), leading to a debonding force almost ten times superior to that obtained with an untreated wire. The force reached with a modified plasma treatment is almost the same, whereas the primer and plasma treatment used separately leads to lower force. The untreated wire does not lead to significant improvement of the interface mechanical resistance. Fig. 1.15, presents the initial curve slopes obtained during the tests (in N/mm). These slopes are calculated before the beginning of the debonding process, *i.e.* before the

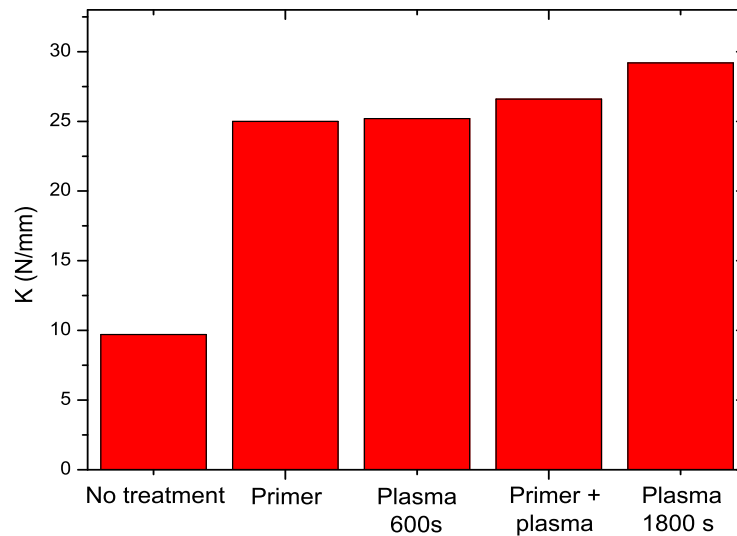


Figure 1.15: Initial slopes obtained during a pull out test.

first peak on each curve. It can be seen here that the increase in the initial slope is less important than for the forces compared to the untreated wire (about two and a half times greater here). The initial curve slopes are almost the same for all the treatments, meaning that all the treatments lead to the same initial mechanical property, but differences appear after the first peak.

1.1.4 Conclusion

Different methods to improve the adhesion between NiTi and silicone were tested in this study. First, NiTi wire deoxidation shows no beneficial effects on the mechanical interface resistance. Second, significant improvements of the interface resistance were obtained using a primer and a plasma. The two treatments were found to bring equivalent improvement of the interface. Third, the combination of both primer and plasma (primer then plasma in fact), and a longer exposure time for plasma leads to the best mechanical resistance reinforcement. Even if the primer followed by a plasma presents the better mechanical results, the plasma treatment with an exposure time presents more advantages as it can be applied in various cases contrary to the primer treatment, typically if we consider wire tangle. Finally, this study opens a new route on the elaboration of biocompatible interfaces between NiTi and silicone rubbers, which is currently investigated by the authors.

1.2 Elaboration of a tubular architected composite

T. Rey, J.-B. Le Cam, G. Chagnon, D. Favier, M. Rebouah, F. Razan, E. Robin, P. Didier, L. Heller, S. Faure, K. Janouchova
Submitted to Materials Science and Engineering: C.

This paper deals with composite structures for biomedical applications. For this purpose, an architected tubular structure composed of Nickel Titanium (NiTi) Shape Mem-

ory Alloy (SMA) and silicone rubber was fabricated. One of the main interests of such structures is to ensure a good adhesion between its two constitutive materials. A previous study of the authors (Rey *et al.*, 2014) has shown that the adhesion between NiTi and silicone rubber can be improved by an adhesion promoter or plasma treatment. However, adhesion promoters are often not biocompatible. Hence, plasma treatment is in a favored to be used in the present study. Three different gases were tested; air, argon and oxygen. The effects of these treatments on the maximum force required to pull-out a NiTi wire from the silicone rubber matrix were investigated by means of pull-out tests carried out with a self-developed device. Among the three gases, a higher maximum force was obtained for argon gas in the plasma treatment. A tube shaped architected NiTi/silicone rubber structure was then produced using this treatment. The composite was tested by means of a bulge test. Results open a new way of investigations for architected NiTi-silicone structures for biomechanical applications.

1.2.1 Introduction

Smart materials and structures are widely used to solve biomedical problems. For example, stents are commonly used for several years. Some of the applications using a stent needed a tubular structure with a small variation in length during radial or bulge solicitations. This shows the interest of such architected NiTi silicone rubber structures for biomedical applications. Some of the studies reported focus on NiTi associated with polymers [Neuking *et al.*, 2005; de Araùjo *et al.*, 2008]. To the best knowledge of the authors, the work by Heller *et al.* [2012] is the only one dealing with elastomer combined with NiTi. They proposed NiTi-braided elastomer composites for smart structure applications. Each of the two constitutive materials are well known for their typical behavior: NiTi exhibits superelasticity and shape memory behavior, and silicone rubber exhibits hyperelasticity allowing large deformations without permanent set. The use of NiTi was investigated for many applications during the last few years, especially in the medical field [Duerig *et al.*, 1999; Morgan, 2004; Petrini and Migliavacca, 2011; Nespoli *et al.*, 2014] due to its biocompatibility [Berger-Gorbet *et al.*, 1996; Es-Souni *et al.*, 2005; Bansiddhi *et al.*, 2008; Khalil-Allafi *et al.*, 2010; Jani *et al.*, 2014]. Also, similarly to SMA, elastomers are often considered to make composites [Thein-Han *et al.*, 2009; Oppenheim *et al.*, 2010]. For applications where the composite requires a good mechanical resistance, the efficiency strongly depends on the interface between the NiTi and the polymer matrix. Some investigations to improve their adhesion have already been reported in the literature, highlighting that numerous treatments can change the quality of the interface. Indeed, the adhesion between the two materials can be improved by mechanical [Jonnalagadda *et al.*, 1997; Lau *et al.*, 2002] or chemical [Smith *et al.*, 2004] treatments, or by a combination of mechanical, physical and chemical surface treatments [Neuking *et al.*, 2008]. Each treatment presents its own disadvantages: the mechanical treatments are not applicable for every geometries and chemical treatments such as adhesion promoters are often unsuitable for biocompatibility. For these reasons, the use of plasma treatment seems to benefit both of the interface resistance [Neuking *et al.*, 2008; Rey *et al.*, 2014b] and the interface biocompatibility [Sui *et al.*, 2007]. It was also used in polymeric materials to improve the efficacy of voice prosthesis [Everaert *et al.*, 1998] or to fulfill the requirements medical in medical applications

[Oehr, 2003].

The aim of the present study is to fabricate and to characterize the mechanical response of a smart tubular structure, by assembling NiTi wires with silicone rubber whose interface resistance is improved by plasma treatment. Section 1.2.2 presents the materials, and the different self-developed devices to test the interface, to produce and to test the composite. Results obtained from the tests performed are given and discussed in section 1.2.3. Finally, some concluding remarks close the paper.

1.2.2 Experimental setup

1.2.2.1 Materials

Commercial pseudoelastic NiTi (50.8 at.% of Ni) SMA wires of 0.5 mm diameter were used for the tests of the interface. The Austenite to Rhombohedral phase (A to R) transformation occurs during cooling at a temperature equal to 0°C and the reverse transformation (R to A) occurs at a temperature equal to 10°C. The Rhombohedral to Martensite (R to M) transformation was not observable by means of DSC, because it occurred at a temperature lower than -90°C, which is the limit of the DSC system used. Thinner NiTi wires with dimensions of 0.1 mm diameter were used to fabricate the composite. Characteristic temperatures were previously identified by DSC [Rey *et al.*, 2014b]. The austenite to rhombohedral (A to R) transformation occurs during cooling at a temperature equal to 30°C and the reverse transformation (R to A) occurs at a temperature equal to 34°C. Like previously, the rhombohedral to martensite (R to M) transformation was not observable on the DSC.

A uniaxial tensile test was performed at room temperature on two NiTi wires. Results are presented in Figure 1.16. Both wires exhibit large deformations (for a metallic material) with a low residual strain, and a typical superelastic behavior: an (austenitic) elastic part is first observed, followed by a plateau corresponding to a phase transformation (A to M), and a second (martensitic) elastic part. The different values of the plateau during loading and unloading is induced by a mechanical hysteresis. A biocompatible silicone rubber (Bluestar RTV 4404) was used as polymer matrix. The elaboration process of the silicone rubber is the following: its two components were mixed, this mixture was then degassed, and finally cured for 1 hour at 80°C. The silicone rubber is subjected to cyclic tensile test for four cycles at four increasing maximum strains at room temperature. Results obtained are presented in Figure 1.16, in terms of the nominal stress (*i.e.* first Piola-Kirchhoff stress, defined as the ratio of the current force by the initial surface) versus strain. Here, several classical phenomena in rubber can be observed. Firstly, rubber undergoes large deformations upon loading with low residual strain after unloading (less than 8% for a maximum strain equal to 150%). Secondly, mechanical hysteresis was observed, *i.e.* difference of stress between loading and unloading. Thirdly, the stress response for subsequent loadings was different. Stress softening or 'Mullins effect' [Mullins, 1948] was mainly observed during the first loading.

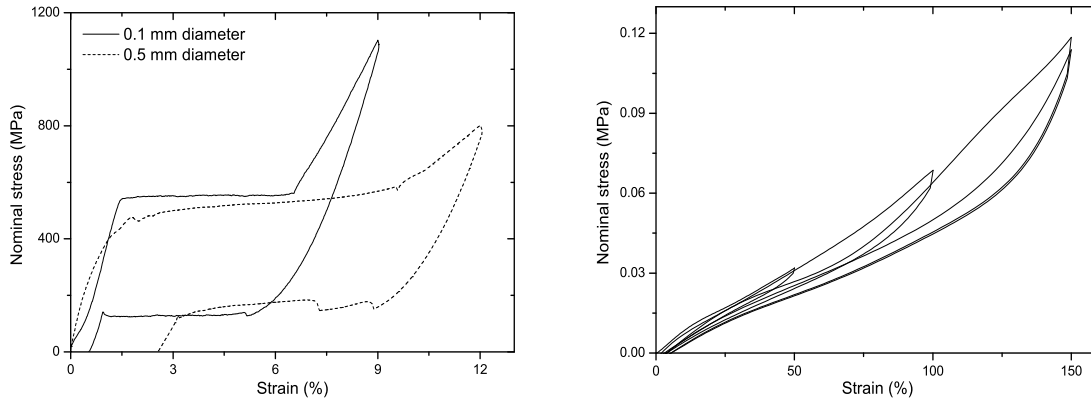


Figure 1.16: Tensile test on the NiTi wires (on the left) and on a RTV 4404 silicone rubber (on the right).

1.2.2.2 Interface characterization

Sample preparation

The adhesion between NiTi and silicone rubber was performed by using a plasma treatment without any chemical substances [Neuking *et al.*, 2008; Rey *et al.*, 2014b]: a gas under low pressure is subjected to a high frequency oscillating electromagnetic field and the accelerated ions in the gas collide with the gas molecules, ionizing them and forming plasma. The ionized gas particles in the plasma interact with solid surfaces placed in the same environment by removing organic contamination from surfaces and modifying or enhancing the physical and chemical surface characteristics [Winters and Coburn, 1992]. The type of interaction between plasma and surface depends on parameters such as the intrinsic properties sample or gas(es) composition and flux, electrical power, exposure time, pressure [Rosnagel *et al.*, 1990]... The treatments were carried out with different gases to study their influence on the mechanical response of the NiTi/silicone rubber structure. The plasma treatments using argon or oxygen as working gases were performed using a RIE 300, whereas the plasma treatment with air as working gas was performed using a Harrick Plasma Cleaner. In both cases, the power and exposure time were fixed at 30 W and 720 s respectively. The treatment was performed under vacuum conditions, with operation pressure set equal to 10^{-1} kPa and 2.10^{-2} kPa for the RIE 300 and the Harrick Plasma Cleaner, respectively. Once the wire surface was treated by plasma, it was placed into a self-developed mold, already used in a previous paper of the authors Rey *et al.* [2014b]. The mold was then closed, and the silicone was blended to a curing agent and degassed, before injected into the mold using a medical syringe. Finally, the mold was placed into an oven for 1 h at 80°C to cure the silicone. The diameter of the cured disk of silicone is 30 mm and the thickness is 5.4 mm.

Pull-out tests

In order to investigate the adhesion between silicone rubber matrix and embedded NiTi wire, pull-out tests were performed. This type of test is classically used in the literature [Lau *et al.*, 2002; Smith *et al.*, 2004; Neuking *et al.*, 2008; Sadrnezhaad *et al.*, 2009; Rey *et al.*, 2014b] to evaluate the mechanical resistance of the interfaces. For this test, the increase of the adhesion strength is defined by the increase of the maximum required force

to pull-out the NiTi wire from the polymer matrix. The pull-out tests were performed using an Instron 5543 testing machine, which load cell capacity is 1 kN. The device is illustrated in a previous paper of the authors Rey *et al.* [2014b]. During the test, the sample was kept in the mold to avoid any slipping of the silicone rubber. The mold was mounted in a self-developed device. The wire was placed into the jaw, and was then pulled from the silicone disk in the vertical direction at room temperature and at a displacement rate of 0.6mm/s.

In order to check the interface stability over time, pull out tests were performed at different times after molding, between 0 and 7 days.

Additional analyses

Measurements of the wire deformation were carried out by marks tracking method in order to check that no transformation occurred in the SMA wires during the pull-out tests. Moreover, Scanning Electron Microscopy (SEM) observations of the wires were performed with a JEOL JSM 6301F in order to observe surfaces of the pulled-out wires. In order to analyze the effects induced by the plasma treatment, several observations were made before and after the treatment.

Roughness evaluation of a NiTi plate was performed before and after the more efficient plasma treatment. The composition of the NiTi plate is the same than those of the NiTi wires (50.8 at. % of Ni), and its length, width and thickness are 75, 15 and 3 mm, respectively. This analysis was carried out with a surface profiler (Alpha-Step IQ, KLA Tencor). Measurements were performed by means of a diamond tip moving on the specimen surface. For the present measurements, the length, speed and frequency were chosen equal to 500 μm , 20 $\mu\text{m/s}$ and 200 Hz, respectively. The roughness was calculated as the arithmetic average between successive minimum and maximum values of the height (called Ra).

Wettability tests were also carried out on a similar NiTi plate. A liquid droplet was put at the surface of the specimen under study and the diameter and height of this droplet were measured. By this way, the contact angle between the droplet and the specimen can be calculated. The droplet volume is equal to 3 mm³. Two liquids were used: water and diiodomethane. The surface energy was then calculated, using the method proposed in Owens and Wendt [1969].

1.2.2.3 Elaboration of the composite

In order to obtain a tubular shaped composite, NiTi wires were knitted and then a shape setting was performed at 450°C (see Figure 1.17 a)). The tube obtained was threaded on a metallic tube and fixed to two holding parts in order to avoid any displacement during the injection of the silicone rubber. Then, this tube was treated by plasma for 720 s at 30 W with the working gas giving the best results with the pull-out tests. The treated NiTi tube was then put in a self-developed mold, to be embedded in the polymer matrix, which is injected by the way of a medical syringe. Finally, the mold was placed into an oven at 80°C for 1 hour. The obtained composite is presented in Figure 1.17 b), with the two holding parts at its extremities. Its length, internal and external diameters are 30, 8 and

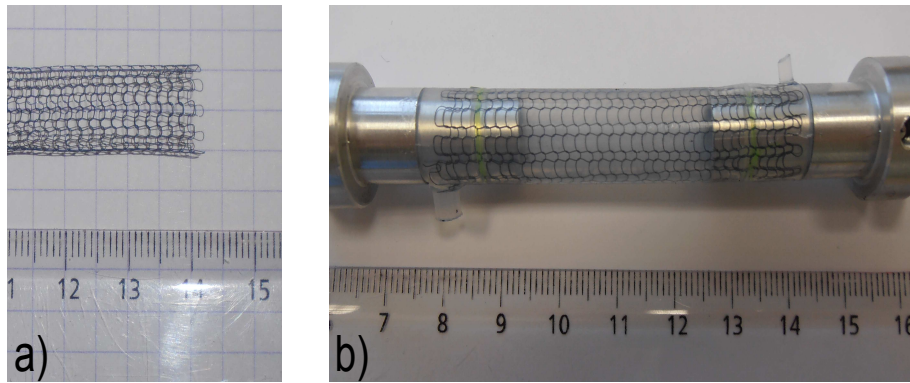


Figure 1.17: Knitted tube of NiTi (a), tube embedded in a silicone rubber matrix (b).

12 mm, respectively. Several tubes were fabricated in order to check the reproducibility of the process.

1.2.2.4 Bulge test

A bulge test was performed by injecting water into the composite. Figure 1.18 gives an overview of the experimental setup. The composite was suspended by one of the holding

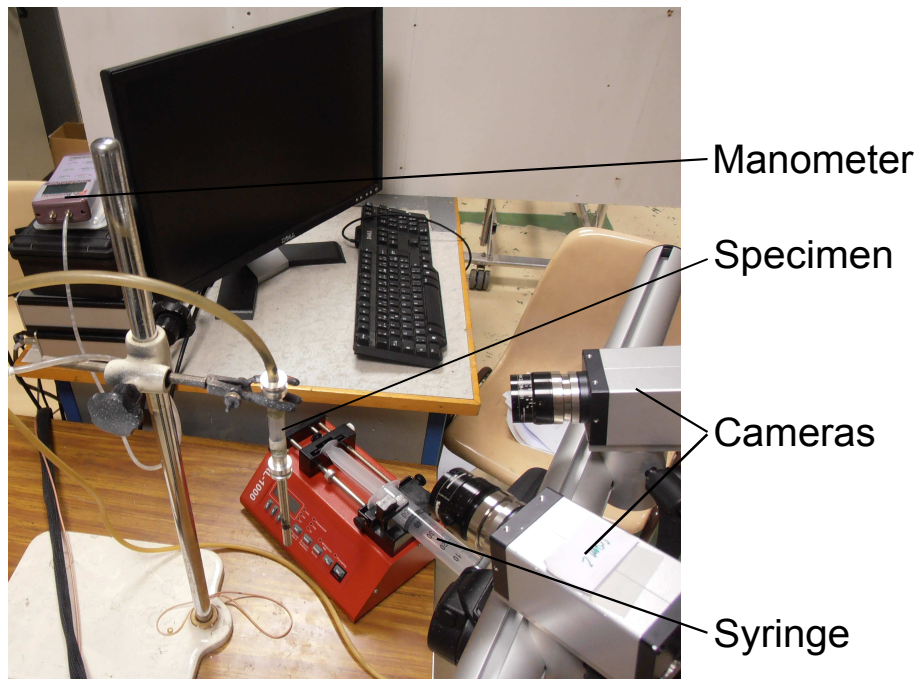


Figure 1.18: Overview of the bulge test.

parts, and a water injection pipe was connected at this part. The other extremity was closed by a cork. It is worth noting that even though a low amount of force (0.54 N) was imposed (by the weight of the cork and the holding part), the displacements of the inferior part were not blocked. Water was injected at a constant volume rate by the way of a medical syringe. The pressure in the tube was measured with a manometer.

During the bulge test, the strain field at the composite surface was measured by means of a Stereo Digital Image Correlation (SDIC) system. The CDD sensor of the two cameras used features 1028 X 1028 connected pixels. A speckle pattern was done using a special powder coating on the tube surface for the SDIC, and appropriate lighting has been set up. A marks tracking method was also used to follow the displacement of four crosses at the tube surface and to obtain quantitative values of displacements. Two crosses were marked at the top and bottom of the tube in order to measure length variations, whereas the two others were marked at the center in order to observe the circumference variations.

1.2.3 Results and discussion

1.2.3.1 Pull-out tests

Results of the pull-out tests are presented in Figure 1.19 a). Tests were found to be repeatable. Hence, only one curve is plotted for each treatment. The force was found to

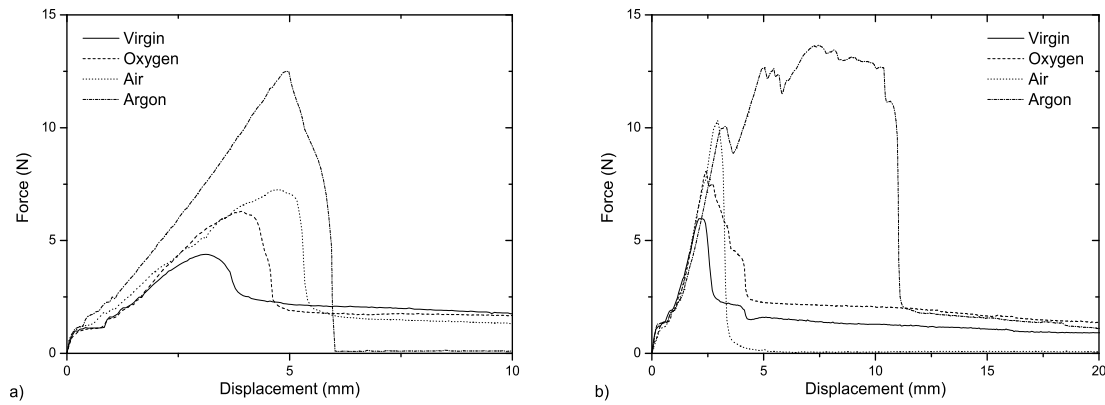


Figure 1.19: Results of the pull-out tests with different treatments, with a silicone pancake thickness of a) 5.4 mm and b) 2 mm.

increase with a plasma treatment regardless the type of gas considered: 33%, 48% and 159% for oxygen, air and argon, respectively.

It is to note that for several applications, thickness of the embedding polymer matrix is not of the same order as the pull-out tests (*i.e.* at least ten times superior than the wire diameter). For this reason, the same tests were carried out with a thickness of the silicone pancake equal to 2 mm. The results obtained are presented in Figure 1.19 b). This Figure shows that even though the forces reached are different, the trend remains the same as that observed for the classical pull-out tests: the highest maximum forces were obtained for argon, with an increase of maximum force of 158% (14.05 N versus 5.45 N without any treatment). This shows that the efficacy of the treatment and the classification of the treatment do not depend on the thickness of the silicone pancake in the range of thickness tested. Additional pull out tests were carried out using both argon and oxygen (same proportion of each gas), and results showed once again that it is less efficient than using argon only. A comparison with the same tests performed in Rey *et al.* [2014b] with another filled silicone rubber (Bluestar RTV 3428) shows that the efficacy of the plasma treatment strongly depends on the nature of the considered polymer. Indeed, in the present study, the treatment with air gas is less efficient than in Rey *et al.* [2014b]. In the present

study, the ratio between the maximum forces reached with treated and untreated wires was inferior to 2, while it was superior to 7 in Rey *et al.* [2014b]. The results of the wires deformation measurements showed that the local deformations observed on the wires were too low to induce any transformation phenomenon.

Results of the pull-out tests performed several days after molding showed a low increase of the maximum force measured. Even if these results show that the mechanical properties of the interface remained constant at the time scale of several days, additional tests have to be carried out for higher post-molding times, depending on the considered application.

1.2.3.2 Post-mortem analysis of the interface zone

SEM observations are presented in Figure 1.20, for an untreated wire (a), and for wires treated with plasma using oxygen (b), air (c), and argon (d) as working gas. Without any

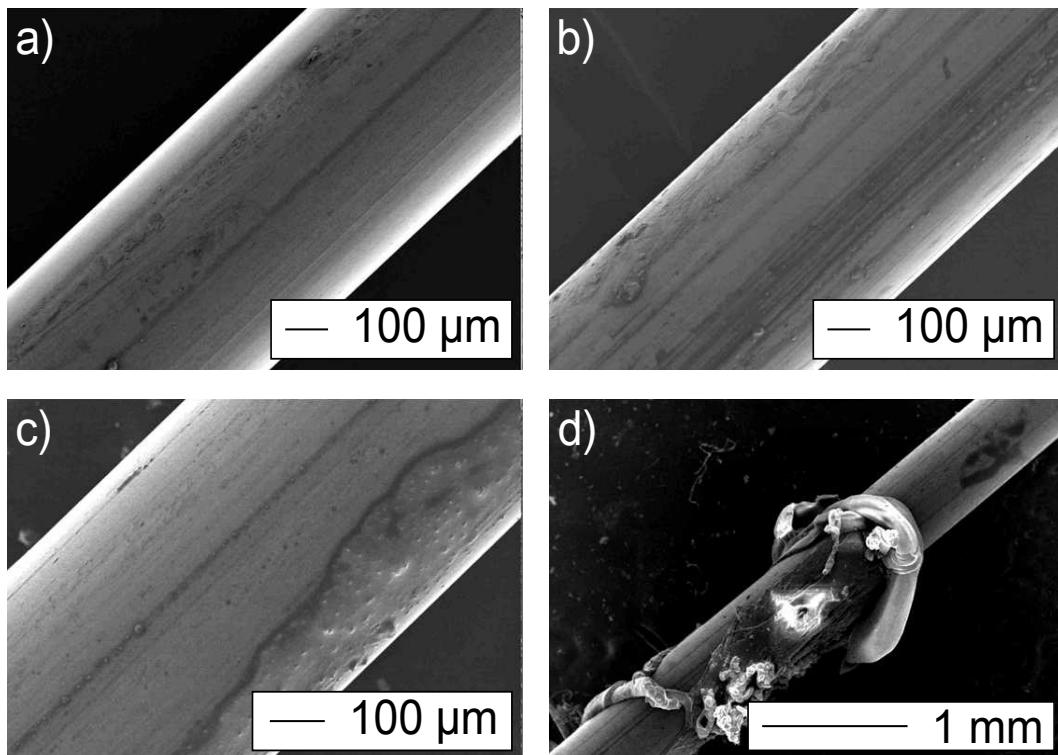


Figure 1.20: Observation of the pulled-out wires a) without any treatment, and treated by plasma with b) oxygen, c) air and d) argon as working gas.

surface treatment, no silicone rubber was observed on the surface of the pulled-out wire, whereas a few parts of silicone were observed for a wire treated with oxygen and air. As shown in Figure 1.20 d), the surface treated with argon gas exhibited large silicone rubber patches which indicates that significant cohesive failures took place in the material before any adhesive failure. This confirms the best efficacy of the plasma treatment with argon. For each condition, no modifications on the surface of the wire were observed for areas without silicone. Results obtained for the roughness analyses showed that the roughness remained constant before and after the argon gas plasma treatment (R_a equal to $0.706 \mu\text{m}$

before and $0.695 \mu\text{m}$ after the treatment). Hence, the plasma treatment does not affect the surface of the NiTi wire, confirming the SEM observations on the pulled-out wire.

Results of the wettability analyses show that the wettability is increased by plasma treatment with argon gas. Indeed, the contact angle measured for water and diiodomethane were equal to 56° and 37° against 17° and 39° before treatment respectively, giving an increase of the surface energy from 50 mJ/m^2 to 70 mJ/m^2 .

1.2.3.3 Bulge tests

As mentioned earlier, the composite was bulged by water injection. Several cycles were carried out in order to investigate the possible irreversibilities in the mechanical response. Figure 1.21 presents the pressure variation during 10 cycles with an injected water volume of 1 cm^3 . The measurements were not performed during the first cycle, as it is a cycle of

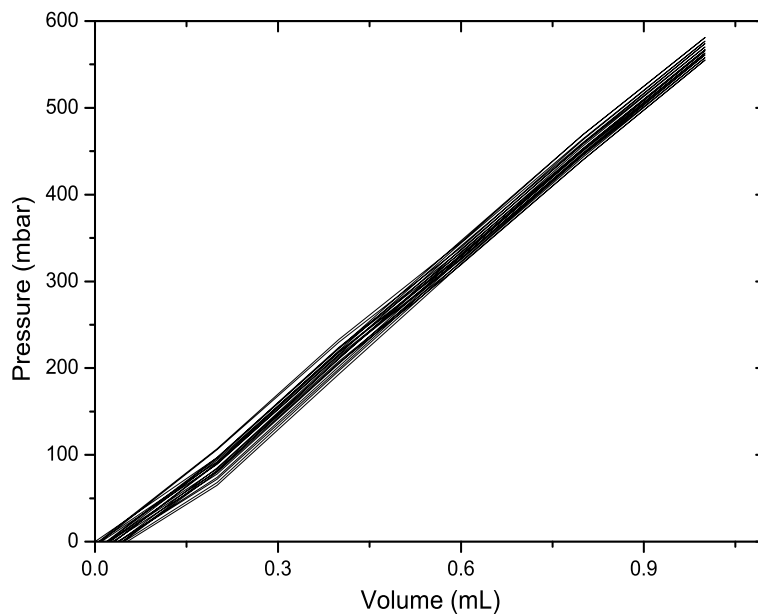


Figure 1.21: Bulge test of the architected composite.

setting up of the system. Thus the cycles presented in the figure are from the 2^{nd} to the 11^{th} . It is observed on this curve that a small amount of permanent set existed between each cycle. Therefore, the mechanical response was considered to be similar throughout the test.

Variation of the tube dimensions were measured during the test by means of marks tracking method. During the test, the tube was kept in a circular shape. So, an increase of the distance between two points in the radial direction corresponds to an increase of the diameter. It was observed that the diameter of the center of the composite increased during the injection of water. At the same time, its length decreased during injection. It should be noted that the composite rotated slightly during the test. These three effects were induced due to the response of the knitted NiTi tube: the mesh gets tighten by itself, inducing a length reduction because stitches are closer, and rotation because the knitting was carried out by a helical method.

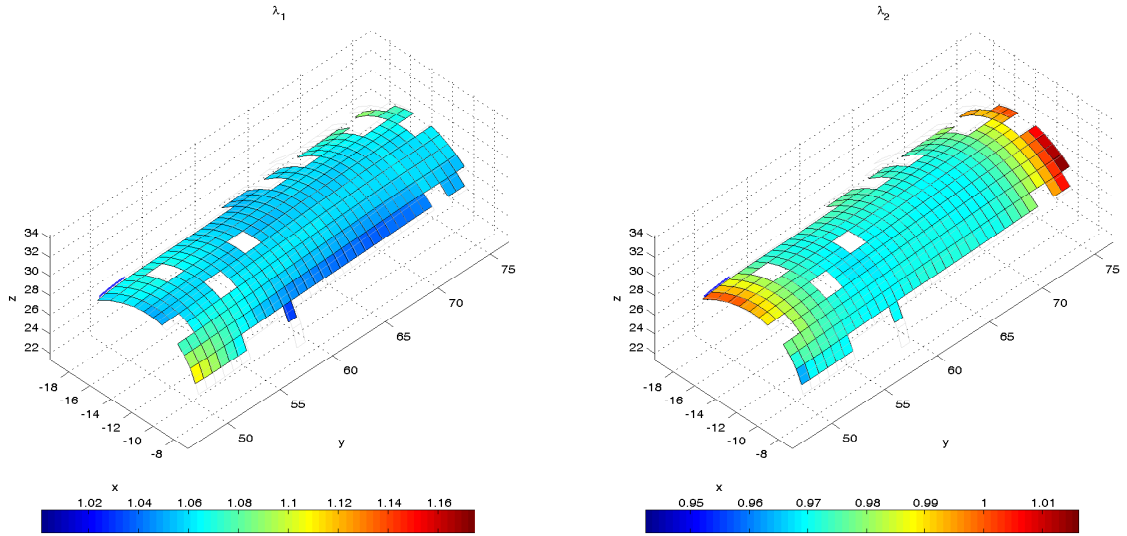


Figure 1.22: Estimation of the stretches by means of stereo-correlation measurements in the diameter (1) and length (2) directions.

In order to analyze the displacements and deformations at the tube surface, SDIC analyzes were also performed during the test. The error on the strain measurements was equal to 0.1%. Figure 1.22 presents the distribution of the stretches in the diameter and length directions (λ_1 and λ_2 respectively), at a pressure slightly lower than 60 kPa. The stereo-correlation results confirmed that the composite diameter increased whereas the length decreased. Here, measurements made close to the holding parts are not taken into account in the analysis, as the 3D reconstruction was distorted due to the clipping of the tube. It can be observed that for a pressure slightly lower than 60 kPa, the strain reached in the diameter direction is equal to 7% in tension whereas it is equal to 3% in compression in the length direction.

A tube of silicone rubber was bulged by the same way in order to analyze the influence of the tubular NiTi structure. Figure 1.23 presents the results of the bulge tests for a silicone rubber tube and a NiTi silicone rubber tube. It can be observed in Fig. 1.23 a)

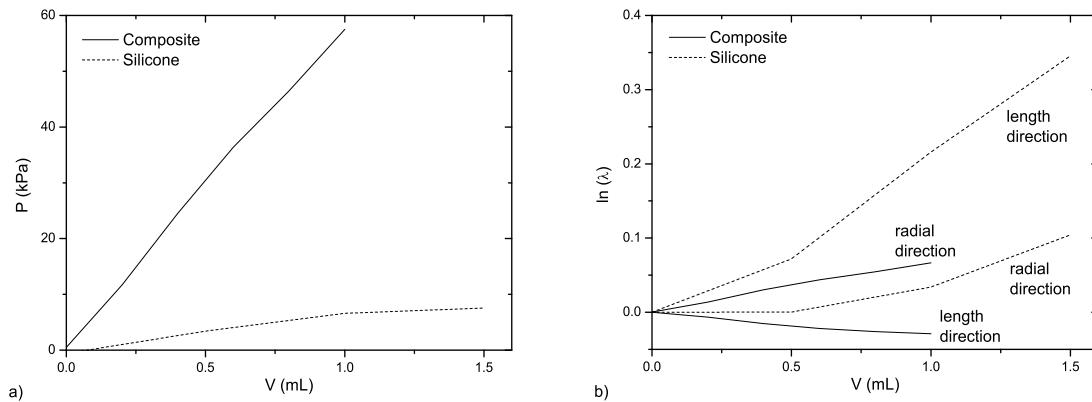


Figure 1.23: Comparison between the bulge of a silicone rubber tube and a NiTi silicone rubber composite tube.

that the addition of the knitted NiTi tube led to a significant increase of stiffness of the

structure. Indeed, the measured pressure in NiTi silicone rubber tube was very higher than for silicone rubber tube (for example, for a volume of 1 cm³, the pressure in the composite tube was equal to 57 kPa instead of 6.5 kPa for silicone rubber, *i.e.* almost 9 times higher). Fig. 1.23 b) shows that the stretch measured in the longitudinal direction was more important than the one in the radial direction for silicone rubber only, and positive logarithmic stretches were observed in the two directions. For the composite, the logarithmic stretch in the longitudinal direction was negative, and less important than the stretch in the radial direction.

1.2.3.4 Discussion

Results highlighted that the composite tube behavior was very different from a tube of silicone rubber. Indeed, as previously observed, the tube of silicone rubber increases its length and diameter during a bulge test. The increase in length is higher than the increase in diameter. It reaches 35% of the initial length, which is not compatible with biomedical applications. When a knitted NiTi structure is used, the length slightly decreased instead of increasing steeply. Moreover, in this case, the length of contraction is lower than the diameter expansion (7%). This is a major advantage offered by such NiTi silicone rubber composite. Several other advantages can also be pointed out.

Firstly, its mechanical behavior can be easily modified. Indeed, it is mainly determined by the mechanical response of the knitted NiTi, whose mechanical behavior can be altered through heat treatments. Secondly, the mechanical response of the knitted tube can be modified by changing the mesh size or by using two wires with different mechanical behaviors before the shape setting step. For instance, to induce a type of anisotropy similar to that observed in soft tissues. Thirdly, the behavior of a NiTi based composite can be driven by several ways: it is well known to react with mechanical, thermal and electrical solicitations. For thermal and electrical solicitations, the silicone rubber isolates the NiTi from the tissues. Finally, no detectable mechanical response changes were observed during cyclic loadings. This offers many possibilities and such a composite should strongly be considered for applications, typically for applications like artificial vessels or stents.

1.2.4 Conclusion

In this paper, a composite structure has been proposed to meet the specific needs in the biomedical field. The composite structure was fabricated by associating a knitted NiTi with a silicone rubber. The interface resistance between both materials was improved by an optimized plasma treatment without any adhesion promoter. A tubular shaped composite structure was fabricated using a self-developed device and submitting it to cyclic internal pressure during a bulge test. Results have shown that under pressure, the strain level is low. The tube contracts in the longitudinal direction and stretches in the radial direction. Consequently, this particular composite structure provides promising aspects for biomedical applications, especially to fabricate artificial vessels or stents.

1.3 Conclusions of the chapter

The mechanical properties of a NiTi silicone rubber composite depend on both the mechanical properties of its constitutive materials and the interface between them. Hence, the adhesion between the two constitutive materials has to be ensured and optimized. Even though many studies on the interface between NiTi and polymers have been reported in the literature, only a few of them deals with adhesion between NiTi and silicone rubber. Several methods have been proposed to improve the adhesion. Their efficiency are classically evaluated by means of pull-out tests. In the present study, plasma treatment and adhesion promoter were used to improve the adhesion and consequently the mechanical properties of the interface between NiTi and silicone rubber. The improvement of the mechanical properties of the interface was evaluated by using a self-developed pull-out device. Results have shown that both the adhesion promoter and the plasma treatment improve the adhesion between NiTi and silicone rubber. Moreover, SEM observations showed that the adhesion between NiTi and adhesion promoter was stronger than between adhesion promoter and silicone rubber. That is why these two treatments were combined (adhesion promoter followed by plasma treatment), and the improvement of adhesion was better than previously. However, plasma treatment also improved the adhesion and was than preferred for addressing biomechanical applications. Nevertheless, it needed to be optimized, *i.e.* to find the best parameter set in terms of treatment duration time and nature of working gas. Therefore, different gases were tested for the plasma treatment. Results of pull-out tests showed that the use of argon and a time duration of 720 s gave a better enhancement than the other gases tested (oxygen and air). An architected NiTi/silicone rubber composite was then fabricated by assembling a knitted NiTi tubular structure and a silicone rubber matrix by using the optimized plasma treatment. The mechanical response of this composite was characterized by means of bulge tests, performed by water injection. Stereo digital image correlation and mark tracking techniques were used during the tests to evaluate the deformation field at the surface of the composite. Results showed that the variations in the composite length were low compared to the radial extension, showing that such a composite is well suitable to fabricate artificial vessels. Moreover, the mechanical behavior of such a composite can be easily modified by changing the properties of the NiTi structure (mesh knitting for example). Moreover, silicone rubber, in which the NiTi structure is embedded, ensures both the impermeability of the composite and the isolation of the NiTi from the external environment. These results and arguments are very promising to address biomedical applications.

Influence of the temperature on the mechanical behaviour of filled and unfilled silicone rubbers

Architected composites presented in the previous chapter can be considered for many applications. Indeed, the combination of these two materials with their typical behaviors makes it very interesting. Due to the thermal properties of the NiTi, which can mechanically react to temperature changes, such a composite can be considered for applications with great temperature variations. Moreover, the results of the tensile tests presented in appendix A confirmed that the mechanical behavior of such a composite depends on the temperature. Nevertheless, even if the thermal properties and the evolution of the mechanical behavior of the NiTi with the temperature are well known, these phenomena were not already studied for silicone rubbers. However, changes in the mechanical behavior of the silicone rubber could affect the mechanical behavior of the NiTi silicone rubber composite. Indeed, a change of temperature could imply for example an increase or decrease of stiffness, stress softening, or mechanical hysteresis of the silicone rubber. That is why it is essential to evaluate the influence of the temperature on the mechanical behavior of the silicone rubber to consider applications with temperature variations for a NiTi silicone rubber architected composite. A study was carried out on two different silicone rubbers (an unfilled and a filled one), and the paper arising for this study is presented in the following of this chapter.

T. Rey, G. Chagnon, J.-B. Le Cam, D. Favier
Published in Polymer Testing 32 (2013) 492-501.

This paper investigates the effects of temperature on the mechanical properties of silicone rubbers. First, differential scanning calorimetry tests are performed to determine the crystallization and melting temperatures. Second, mechanical tests are carried out at different temperatures above that of crystallization, up to 150°C. In this temperature range, the silicone rubbers exhibit entropic behavior. The neo-hookean model is used to fit the mechanical response. Third, the effects of temperature on the hysteresis, the stress softening and the stress relaxation are studied. Strong differences are observed and discussed.

2.1 Introduction

Silicone rubbers are increasingly used in many applications that differ in nature, for instance automotive applications, food storage products, footwear, electronics. This is mainly explained by their easiness of cure and, more generally, of manufacture. Moreover, silicone rubbers do not react with most chemicals, which explains why they are used in many medical applications.

Classically, silicone rubbers are filled with mineral fillers such as silica in order to increase their stiffness. In this case, fillers greatly complicate the mechanical response by inducing numerous phenomena: non-exhaustively, stress softening [Mullins, 1948], the Payne effect [Fletcher and Gent, 1953; Payne, 1962] and mechanical hysteresis. Even although mechanical response of filled and unfilled silicone rubbers has already been characterized in the literature at room temperature [Meunier *et al.*, 2008; Machado *et al.*, 2010, 2012], no study investigates the effects of temperature on the mechanical response, while the large variety of applications requires a large range of service temperatures. Moreover, temperature variation affects the interaction between the fillers and the rubber matrix [Rothon, 2001] and, consequently, it is necessary to study both filled and unfilled silicone rubbers. This paper aims, therefore, at investigating the influence of temperature above that of crystallization on hyperelasticity, stress softening, mechanical hysteresis and stress relaxation. Section 2.2 presents the materials and the experimental setup. Section 2.3 gives the results obtained for both materials. The evolution of the various phenomena involved in the deformation of silicone rubbers is discussed in Section 2.4. Finally, concluding remarks close the paper.

2.2 Experimental setup

This section focuses first on the preparation of the two studied silicone rubbers (Bluestar RTV 141 and RTV 3428), second on the identification of their characteristic temperatures, and third on the mechanical tests performed.

2.2.1 Preparation of the silicone rubbers

The preparation process was similar for the two materials. The first step consisted of blending two liquid components, the uncured unfilled silicone RTV 141A (or RTV 3428A for the filled silicone) and 10/1 phr in weight of the curing agent RTV 141B for the unfilled silicone (or RTV 3428B for the filled silicone). The mixture was then degassed for 30 min in a vacuum chamber to remove any air bubbles to ensure the material homogeneity. The degassed liquid was injected by means of a medical syringe into a closed mold to guarantee a constant specimen thickness (2 mm). Finally, the mold was put in an oven at a temperature of 70°C for 4 h to cure the material. This procedure was previously used for the unfilled [Meunier *et al.*, 2008] and filled [Machado *et al.*, 2010, 2012] silicone rubbers for studying their mechanical properties at room temperature. Before testing the temperature effects on the mechanical properties, it is necessary to check that the material is fully cross-linked in order to not superimpose temperature and cross-linking effects. To this end, the materials were heated at different temperatures for different times after curing and then

cooled at room temperature. One day rest was imposed before performing the mechanical tests. For each specimen, a uniaxial tensile test was carried out at room temperature. Fig. 2.1 presents the results obtained for the unfilled silicone in terms of the nominal

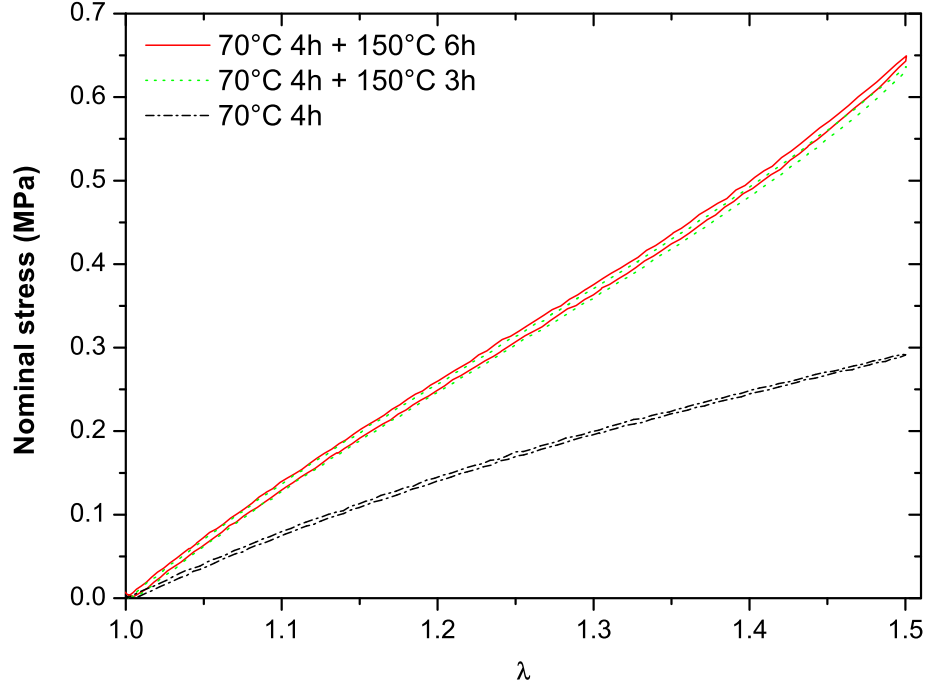


Figure 2.1: Influence of curing time on the strain-stress relationship for the unfilled RTV 141 silicone.

stress versus the stretch ratio λ (defined as the ratio between current and initial lengths). As shown in this figure, the material prepared with the supplier recommendations (4 h at 70°C) is not fully cross-linked. Indeed, the specimens heated at 150°C for 3 and 6 h exhibit stiffer behaviour. Moreover, no variation in stiffness is observed after a heating at 150°C for 3 h. The microstructure of the material is, therefore, stabilized after such a thermal treatment. Consequently, in the present study, the material was heated 3 h more at 150°C. This new procedure ensures that the change in the mechanical response during the test is not due to an increase in cross-linking. It should be noted that no difference was observed for the filled silicone whatever the applied thermal treatment, meaning that the recommendations of the supplier, i.e. 4 h at 70°C, lead to a stabilized microstructure.

2.2.2 DSC and DMTA analyses

DSC (Differential Scanning Calorimetry) and DMTA (Dynamic Mechanical and Thermal Analysis) tests were carried out to define the characteristic temperatures of the two silicones, i.e. temperatures of crystallization and melting for a given temperature rate.

The DSC was performed with a TA Q200 differential scanning calorimeter. The cooling rate was set to 2°C per minute, and the temperature range between 0°C and -90°. Then, heating took place between -90°C and 0°C with the same heating rate as previously used. Specimens of 29 and 37 mg weight were used for the unfilled and filled silicones, respectively. Results are presented in Fig. 2.2. As shown in this figure, an exothermal peak in the heat

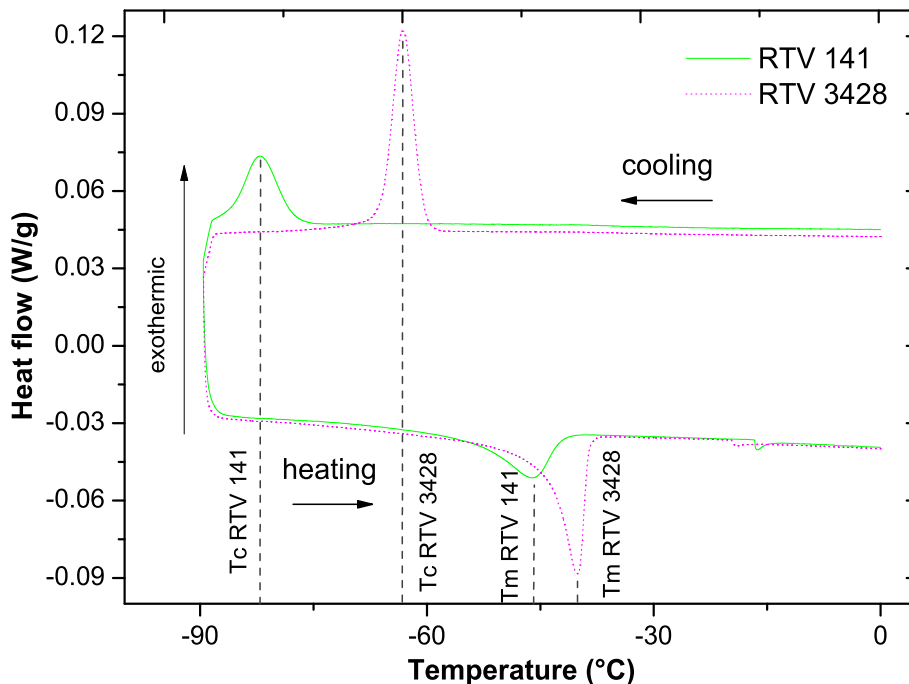


Figure 2.2: Heat flow versus temperature measured by means of a DSC for an unfilled and a filled silicone for a temperature cycle from 0°C to -90°C and from -90°C to 0°C. T_c and T_m are the temperatures where crystallization and crystallites melting occur, respectively.

flow temperature curve is observed for the two materials during cooling, this corresponds to the crystallization of some of the polymer chains. During heating, an endothermal peak is observed, which corresponds to the crystallites melting. The temperatures for which crystallization and crystallites melting occur are denoted respectively T_c and T_m in the following. The values of these characteristic temperatures are reported in Table 2.1. These tests do not allow us to determine the glass transition temperature for both materials, which occurs at temperature lower than -90°C.

	Crystallization temperature	Melting temperature
RTV 141	-83°C	-47°C
RTV 3428	-66°C	-41°C

Table 2.1: Characteristic temperatures for the two silicone rubbers.

Dynamic Mechanical Thermal Analysis (DMTA) tests were carried out by means of a Gabo Eplexor 500N machine with load cell capacity of 25 N. This type of test is classically used to study the amplitude dependence of filler reinforced rubbers (see for instance Rendek and Lion [2010]). The test consists firstly in cooling with a temperature range between 150°C and -100°C at a rate of 2°C per minute, and secondly by heating from -100°C to 150°C at the same rate. The mean strain applied was equal to 15% and a double strain amplitude equal to 0.2% was applied at a frequency of 1 Hz.

Figs. 2.3 and 2.4 present the results obtained for the unfilled and the filled silicone, respectively. Results show that both the storage modulus (E') and the loss modulus (E'')

are not affected by temperatures far from T_c and T_m . During cooling, these two moduli increase sharply close to the T_c for both materials, i.e. from -80°C for the unfilled silicone and from -60°C for the filled one. The results are in good agreement with the literature [Rogero *et al.*, 2005; Stathi *et al.*, 2010]. Moreover, these moduli decrease during heating until the temperature reaches T_m . A significant difference is observed between T_c and T_m for both materials, which confirms the results obtained from the DSC analysis. This difference can be explained by a supercooling effect [Trabelsi *et al.*, 2003]. The values of $\tan \delta$ are about 0.2 for the filled silicone and about 0.05 for the unfilled one, meaning that the filled material is more viscous than the unfilled, which is in good agreement with previous work in the literature [Hou *et al.*, 1999]. $\tan \delta$ slightly decreases for the two materials with decreasing temperature, which highlights that the material viscosity increases by increasing the temperature.

2.2.3 Mechanical tests

As previously shown, the RTV 141 behaves as a purely hyperelastic material at room temperature with a strain at failure close to 100% [Meunier *et al.*, 2008] whereas the RTV 3428 exhibits stress-softening, hysteresis, stress relaxation and undergoes larger deformations [Machado *et al.*, 2010, 2012].

Due to these differences, the mechanical tests performed on both materials were different: for RTV 141, only one uniaxial load-unload cycle at a strain of 50% was performed, with a strain rate of 1.67 s^{-1} , at temperatures between -60°C and 150°C . For RTV3428, it was necessary to perform several mechanical cycles at increasing deformation. Here, the mechanical cycles were carried out from 25 to 250% strain, with an increase of 25% strain between each cycle (see the histogram in Fig. 2.6). These tests were performed with a strain rate equal to 1.67 s^{-1} , between -40°C and 150°C (-60°C is close to T_c for this material).

A second type of mechanical test was then performed, which corresponds to relaxation tests. For the unfilled silicone, a maximum strain equal to 50% was applied with a strain rate set to 1.67 s^{-1} . For the filled silicone, one mechanical cycle was beforehand performed at a maximum strain equal to 250% in order to remove the stress softening of the first cycle and to focus only on the relaxation properties [Bergstrom and Boyce, 1998; Lion, 1997; Yeoh, 1990]. After a rest time greater than 4 h, which ensures recovery of the viscoelastic properties, a relaxation test was carried out by applying a 150% maximum strain with a strain rate equal to 1.67 s^{-1} .

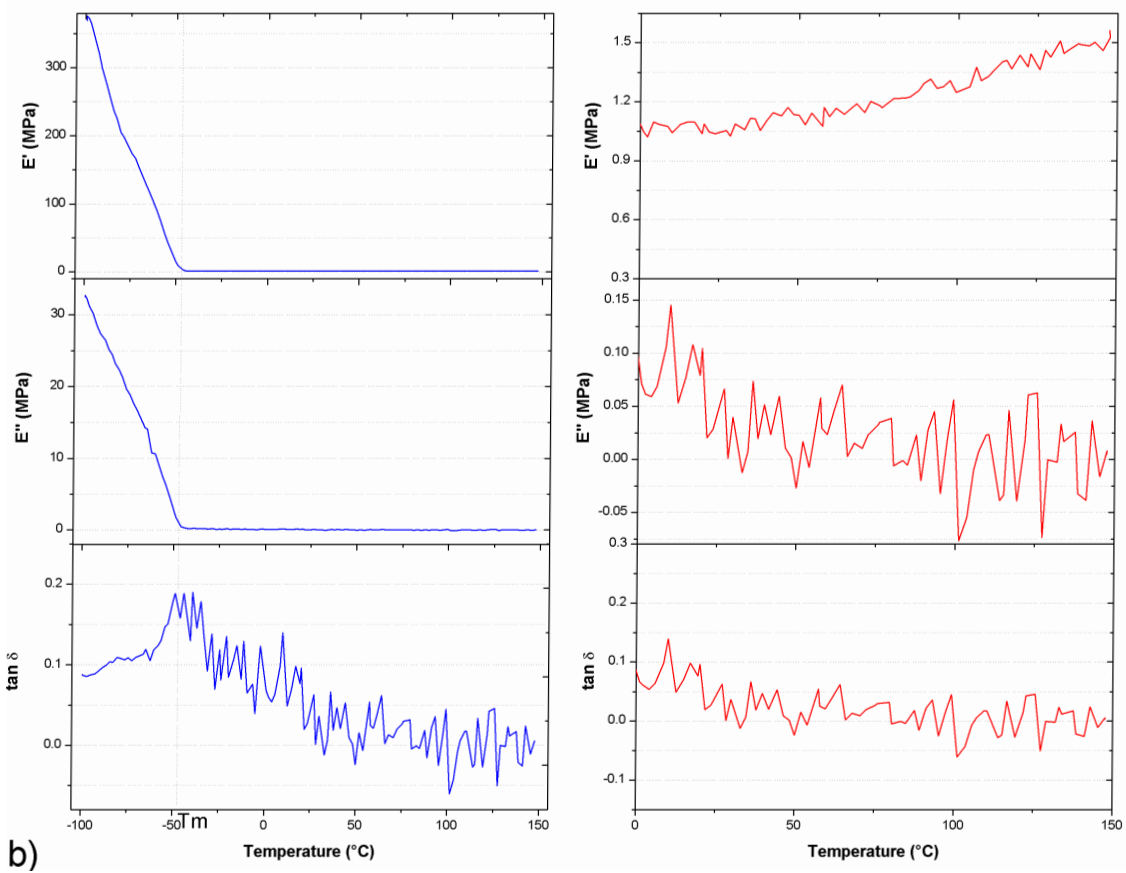
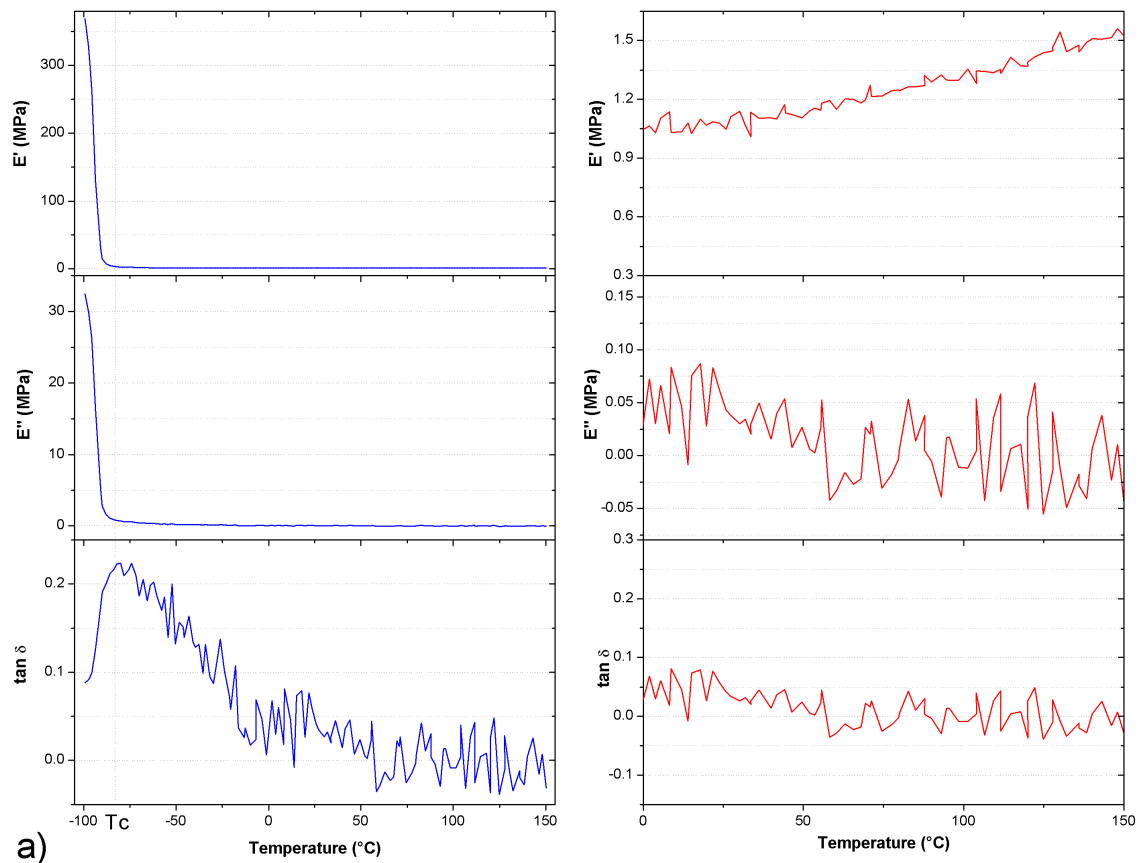


Figure 2.3: DMTA realized on an unfilled silicone rubber, the left side presents the results for the whole temperature measurement range (from -100°C to 150°C) while the right side presents a zoom for positive temperatures (0°C , 150°C) for the cooling (a) and the heating (b).

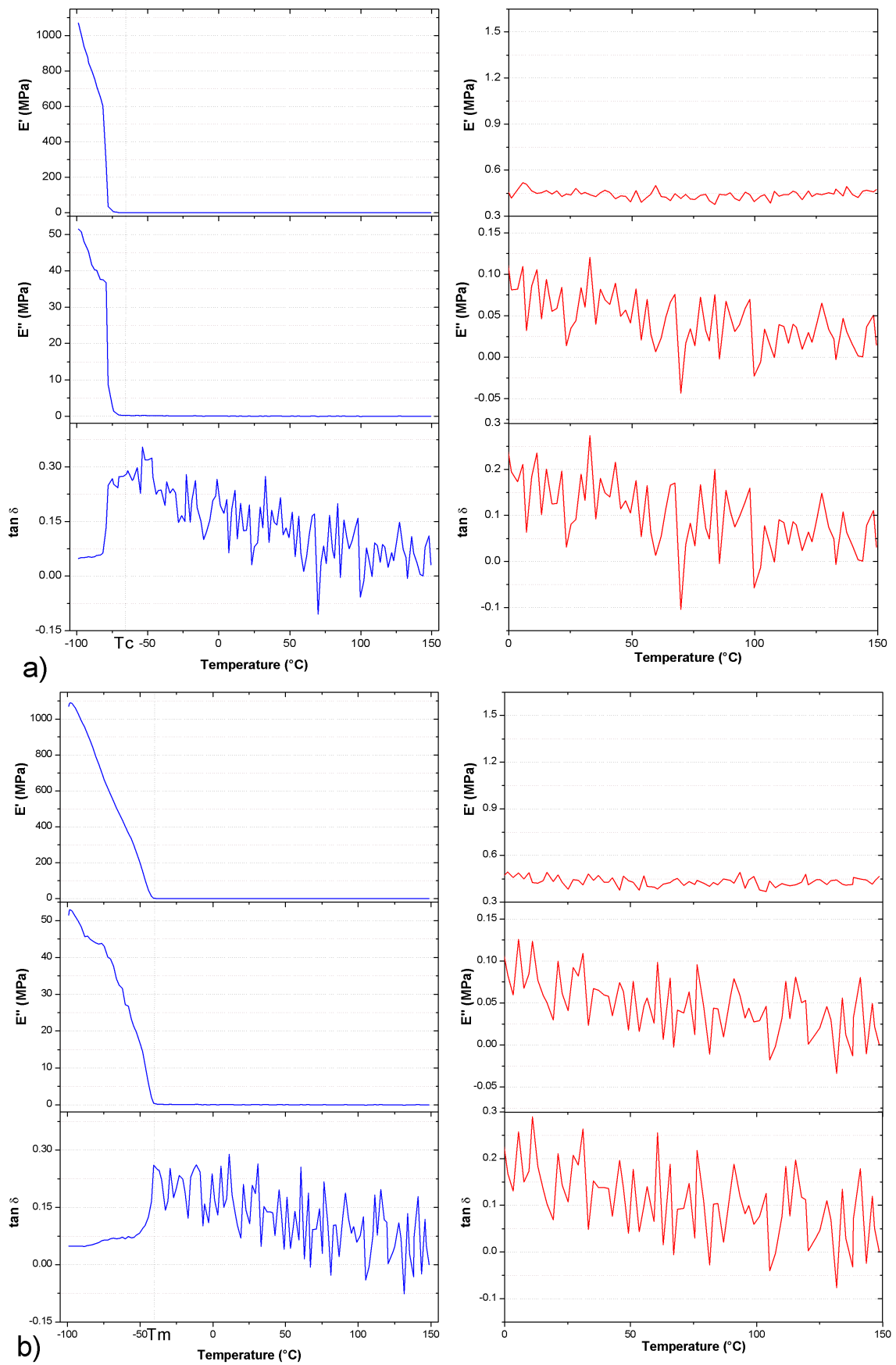


Figure 2.4: DMTA realized on a filled silicone rubber, the left side presents the results for the whole temperature measurement range (from -100°C to 150°C) while the right side presents a zoom for positive temperatures (0°C , 150°C) for the cooling (a) and the heating (b).

2.3 Tests results

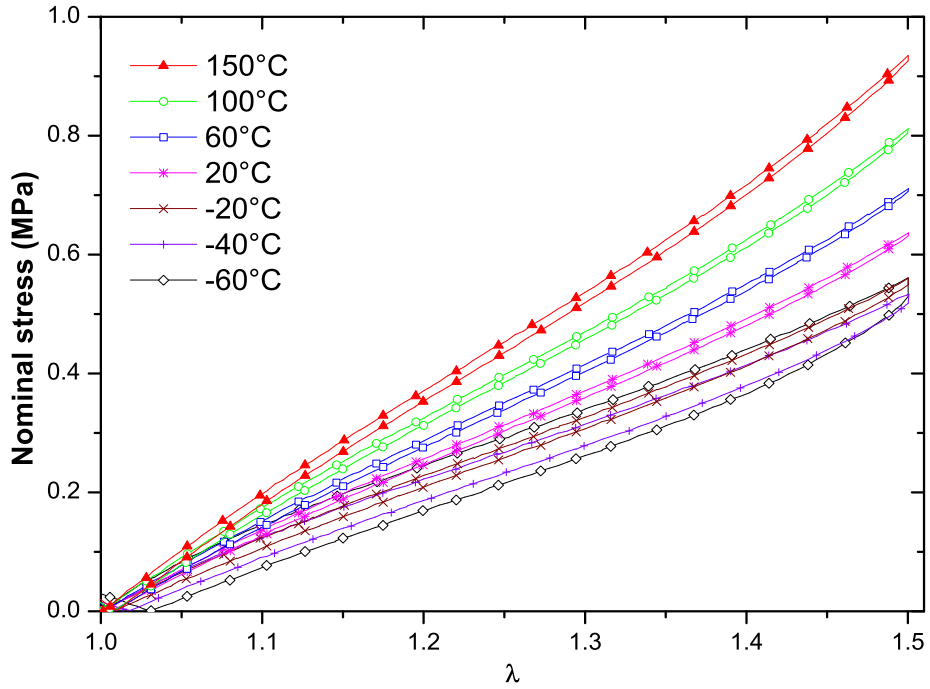


Figure 2.5: Cyclic strain-stress tensile test of the unfilled silicone rubber at different temperatures.

Fig. 2.5 presents the results of uniaxial tensile tests for the unfilled silicone. The stiffness of the material increases with temperature, except at -60°C . These curves highlight the entropic behaviour of the unfilled silicone rubber for temperatures far from T_c . For temperature close to T_c , typically -60°C , the material behaviour remains entropic, but crystallites form in the bulk material and act as fillers [Trabelsi *et al.*, 2003; Flory, 1947]. Consequently, the material stiffness increases, meaning that the effect of crystallization on the mechanical response of the material is of the first order compared to that of entropy variation. It should be noted that the change in the preparation process, more especially the fact that the material is fully cross-linked in the present study, explains the differences from the results obtained by Meunier *et al.* [2008].

Fig. 2.6 presents the results obtained for the filled silicone. First, a significant difference between the load and unload curves is observed, which forms a hysteresis loop. Moreover, a difference of stiffness is observed between the first and the second loads at a same strain level. This softening is one of the features of the Mullins effect [Mullins, 1948]. Second, for temperatures lower than 0°C , the material becomes stiffer when the temperature is close to T_c . For temperatures greater than 0°C , despite a loss of material stiffness due to the viscosity when the temperature increases, the material becomes stiffer, meaning that the entropic effect is more significant than the viscous one. It can be noted that the test performed at 150°C is not completed as the specimen fails at about 200% strain.

Fig. 2.7 presents the results of the relaxation tests for the unfilled silicone. In this figure, the nominal stress is normalized to the maximum nominal stress reached during

the test (the start point of the stress relaxation). The values of the maximum nominal stress measured are reported in Table 2.2.

Temperature	-60°C	-40°C	-20°C	20°C	60°C	100°C	150°C
Maximum nominal stress measured for the unfilled silicone (MPa)	0.57	0.55	0.57	0.65	0.72	0.82	0.94
Maximum nominal stress measured for the filled silicone (MPa)		0.31	0.3	0.33	0.37	0.41	

Table 2.2: Maximum nominal stress measured during the stress relaxation tests.

Each curve represents a monotonic decreasing function of time. Without considering the curve obtained at -20°C , the higher the temperature, the lower the stress relaxation. Results obtained at -20°C are not clearly explained and require further investigation.

Fig. 2.8 presents the results obtained for the filled silicone, Table 2 gives the values of the maximum nominal stress measured. Once again, the relaxation decreases with increasing temperature. These results are similar to those proposed by Laurent *et al.* [2008] and Vandenbroucke [2010] on other rubber-like materials. No result is available at 150°C , due to the fact that the material fails during the preconditioning step at 250%.

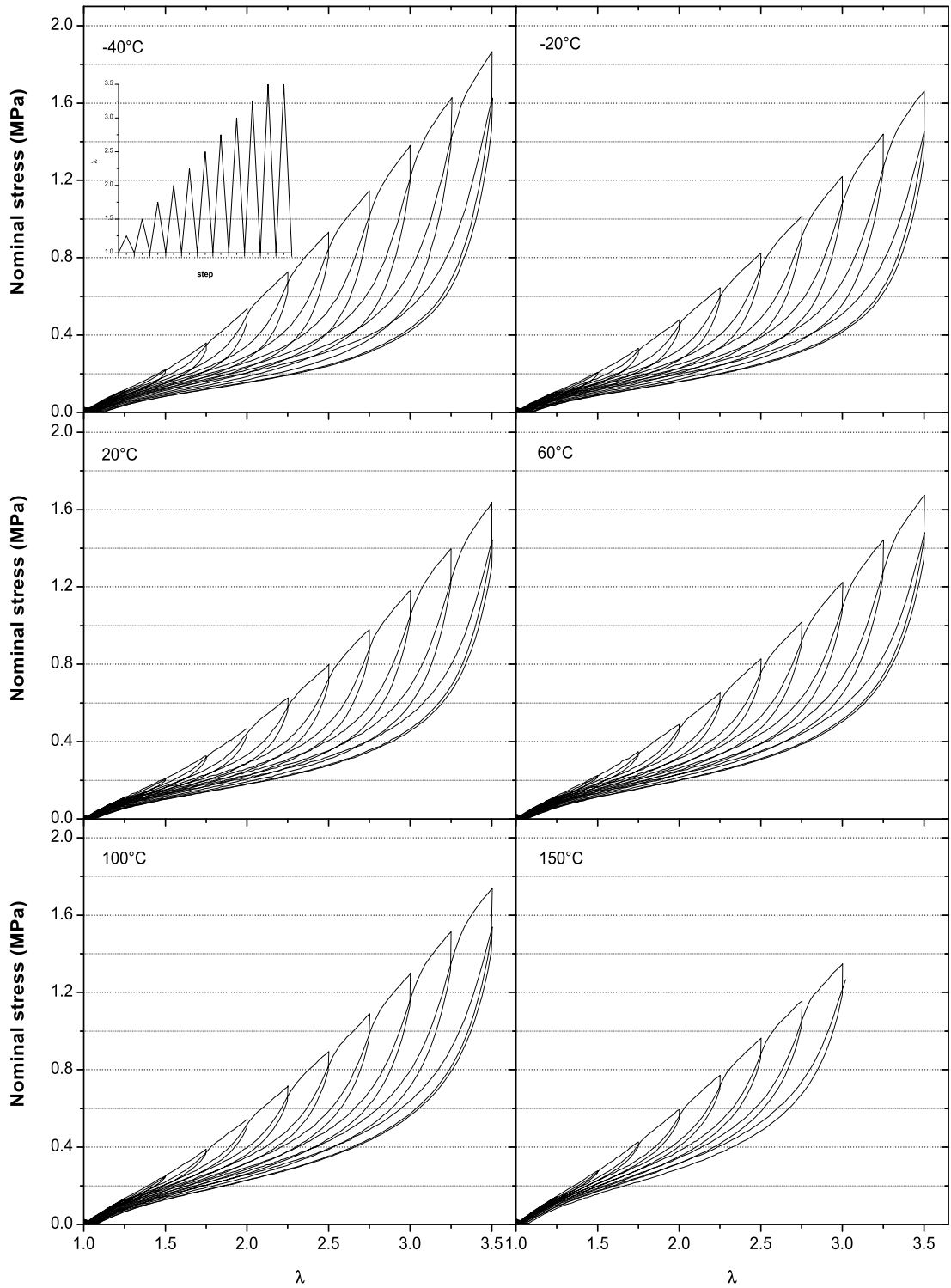


Figure 2.6: Tensile strain-stress curves at different temperatures for the filled silicone rubber.

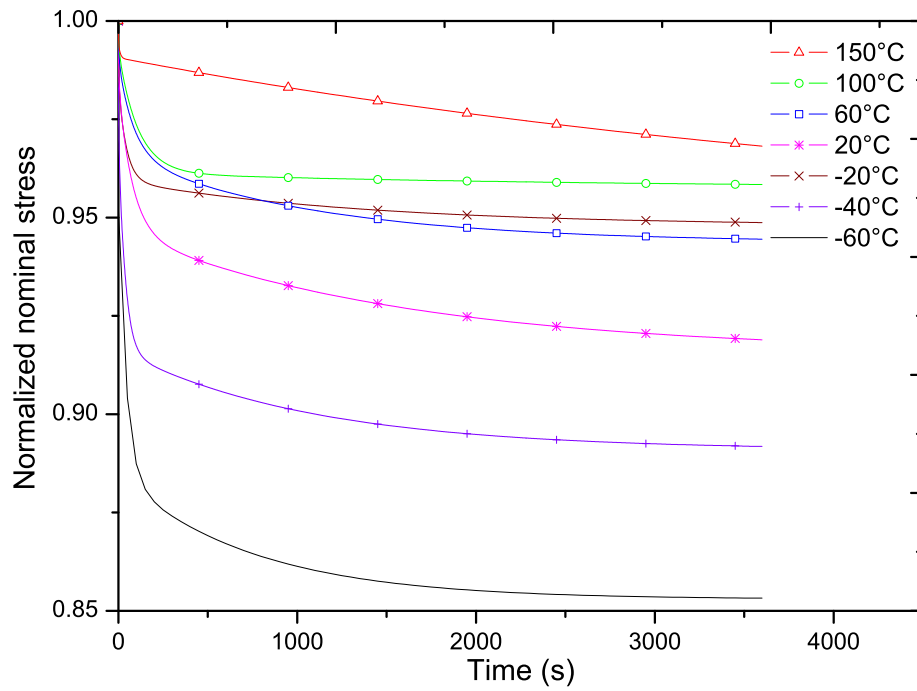


Figure 2.7: Stress relaxation responses for the unfilled silicone.

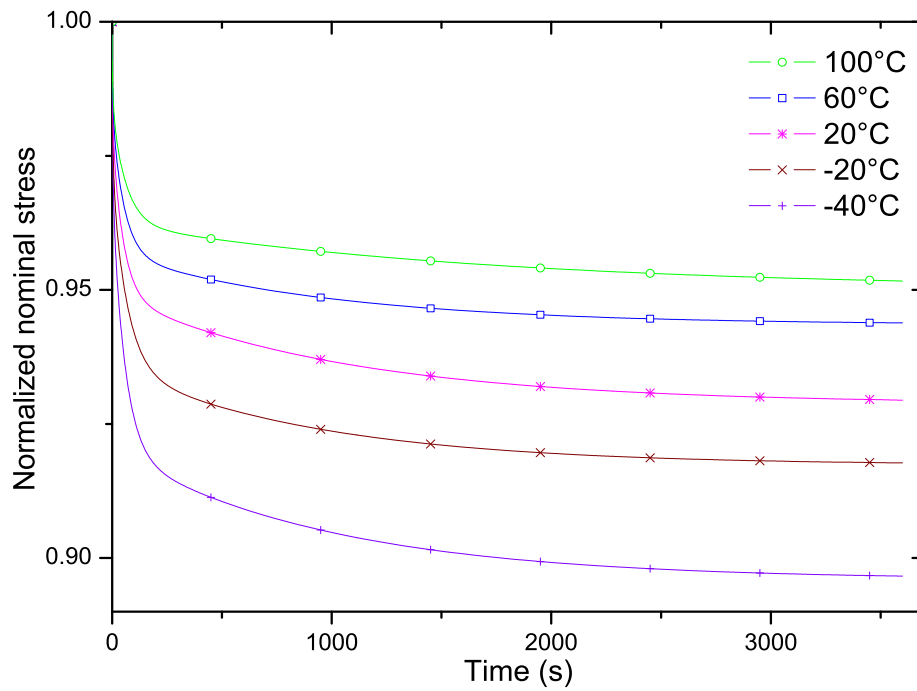


Figure 2.8: Stress relaxation responses for the filled silicone.

2.4 Discussion

In this section, the relation between temperature and strain on the material behaviour is first discussed by considering the neo-hookean model. Then, the effects of the temperature on the Mullins effect and the mechanical hysteresis are successively investigated.

2.4.1 Modeling of temperature dependency of the mechanical response

The neo-hookean model [Treloar, 1943] was used to predict the experimental results previously presented. In this case, the evolution of nominal stress π (in MPa) is written with the stretch λ and the temperature T (in K) as follows:

$$\pi = nkT \left(\lambda - 1/\lambda^2 \right) \quad (2.1)$$

where n is the density of macromolecular chains by volume unit (m^{-3}) and k is the Boltzmann constant (JK^{-1}). The parameter nk was fitted for the unfilled silicone for a temperature of 20°C and a strain level lower than 25%. The value of nk was found to be equal to $1.2910^{-3} \text{ J.K}^{-1}$. Then, this value was used to plot the curves at each temperature. Fig. 2.9 shows the curves obtained. This figure shows that the neo-hookean

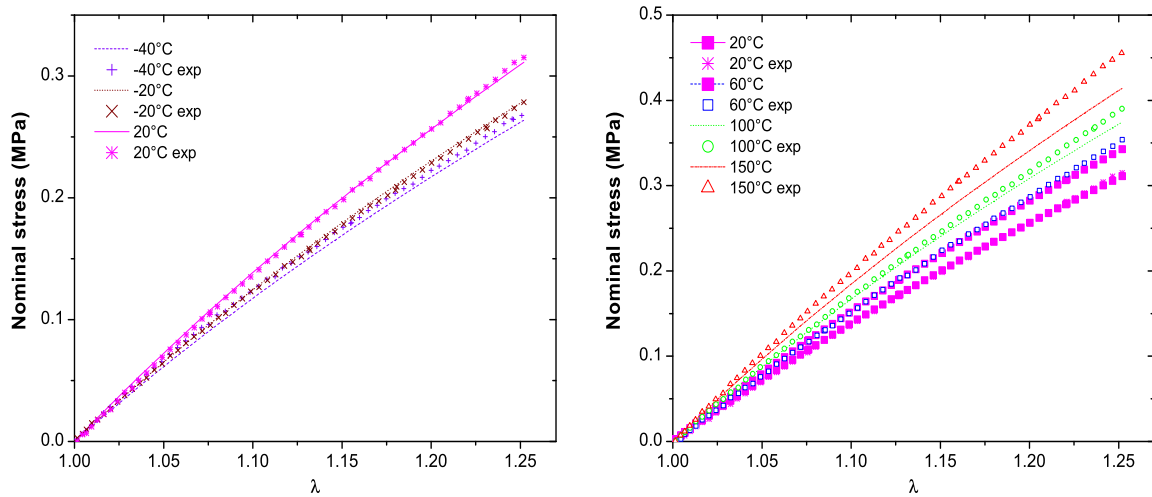


Figure 2.9: Comparison between neo-hookean model and experimental results for the unfilled silicone rubber.

model satisfactorily predicts the experimental results for -20 , 20 and 60°C . However, the model does not predict correctly the material behaviour for temperatures equal to -40°C and 100°C and even less at 150°C . This seems to indicate that the neo-hookean model gives a good approximation of the material behaviour in a range of temperature between -20°C and 60°C (i.e. room temperature $\pm 40^\circ\text{C}$) if the model parameter is fitted from tests at room temperature, 20°C in the present study. The poor prediction of the model for -40°C is due to the fact that the material stiffness is increasing as the appearance of crystallites begins, and the value of nk previously calculated is no longer correct. The same model was used to fit the experimental results of the filled silicone. The parameter nk was fitted on the experimental curve at 20°C , and was used to plot the curves for all the other temperatures. For the filled material, nk is equal to $5.110^{-4} \text{ J K}^{-1}$. Fig. 2.10

gives the results obtained. This figure highlights that the neo-hookean model predicts

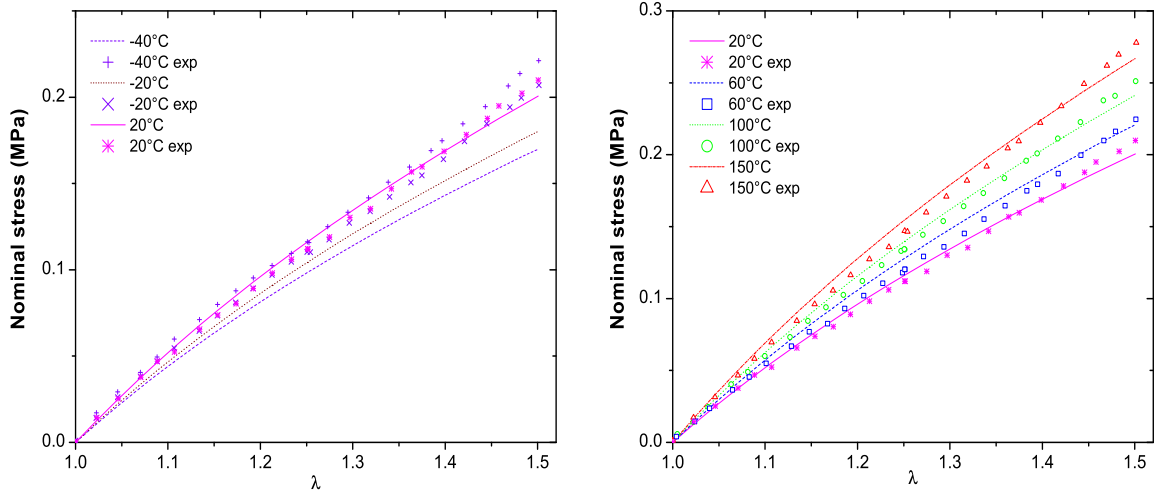


Figure 2.10: Comparison between neo-hookean model and experimental results for the filled silicone rubber.

approximately the evolution in the mechanical response with temperature for this material. The evolution of the mechanical response is underestimated for -20 and -40°C whereas it is better estimated for 60 , 100 and 150°C . This is due to the fact that the neo-hookean model accounts for the macromolecular network elasticity, but not the matrix-filler interactions. More elaborate models could be used, as done for example by Korochkina *et al.* [2008], but it is not the objective of the present study.

2.4.2 Mullins effect

The unfilled silicone is not subject to stress softening, which is the reason why this analysis only deals with the filled silicone. As classically reported in the literature, our results show that the filled silicone exhibits stress softening, which is mainly observed between the first and second loads [Machado *et al.*, 2010]. It has often been considered as a damage phenomenon [Beatty and Krishnaswamy, 2000; Chagnon *et al.*, 2004; DeSimone *et al.*, 2001; Diani *et al.*, 2006b]. In order to evaluate the stress-softening, several methods can be used, among them that by Stevenson *et al.* [2001]. This method consists of calculating the ratio between the energies brought during load and unload. In the present study, we calculated the ratio between the energies brought during second (W2L) and first (W1L) loads. This method, which was previously proposed in Machado *et al.* [2010], allows us to remove the effect of hysteresis from the calculation. The measurement of energy is defined by:

$$W = \int_{\bar{F}} \bar{\pi} : d\bar{F} \quad (2.2)$$

where π is the nominal stress tensor and F is the deformation gradient tensor. Fig. 2.11 presents the evolution of this ratio for different maximum strain levels from 25 to 250% for a temperature range between -40°C and 150°C . It appears that the energy loss increases with deformation whatever the temperature. The curves corresponding to 60 , 100 and 150°C are confounded, meaning that above 60°C the stress softening evolution is not

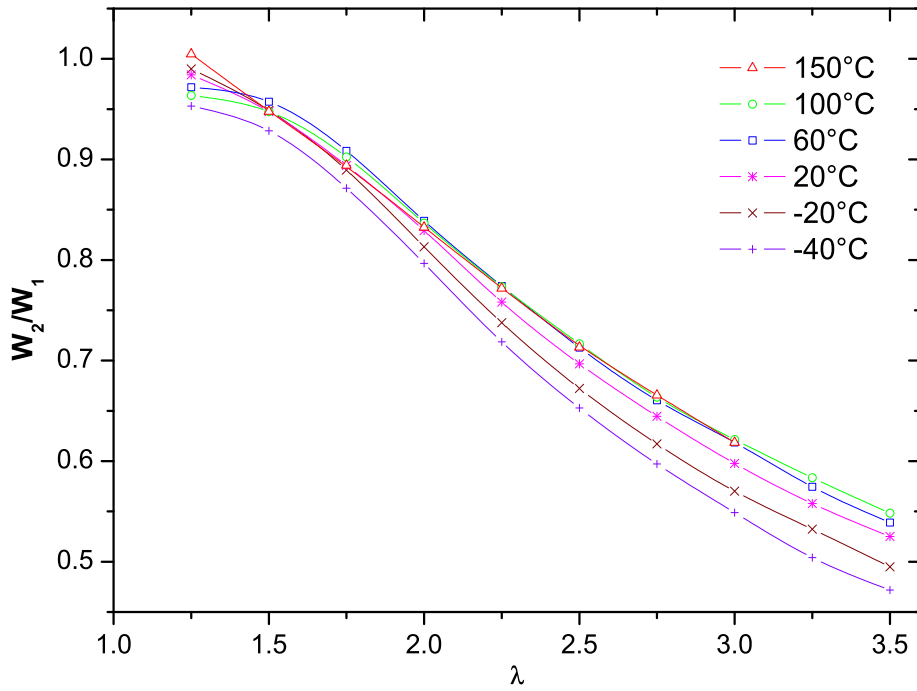


Figure 2.11: Evolution of the energy ratio between first and second loads versus the maximum elongation for different temperatures.

greatly dependent on temperature, whereas below 60°C , the lower the temperature, the higher the stress-softening. This means that the macromolecular network is more sensitive to stress softening at low temperatures.

2.4.3 The mechanical hysteresis

In unfilled silicone, mechanical hysteresis is only observed for a maximum strain equal to 50%. For lower strain levels, it is not detected. Fig. 2.12 gives the evolution of the hysteresis area between load $W1L$ and unload $W1U$ ($W1L-W1U$) versus the temperature for this maximum strain level. As shown in this figure, the hysteresis loop area is quasi-constant for temperatures above 0°C . However, for temperatures below 0°C , the hysteresis loop area greatly increases until the temperature reaches T_c .

For the filled silicone rubber, the hysteresis loop is observed for strains from 25 to 250%. Fig. 2.13 presents the corresponding hysteresis loop area versus the strain. As shown in this figure, the hysteresis loop area increases with the strain and seems to be not affected by the temperature. It should be noted that the area slightly increases with temperatures that tend to T_c .

Fig. 2.14 gives the hysteresis between the second load and unload ($W2L-W1U$). The evolution of the hysteresis loop area versus the strain is similar as that obtained previously for the first load cycles. The difference lies first in the size of the hysteresis loops, which are five times smaller than for the first load cycles, and second in the fact that the higher the temperature, the smaller the hysteresis loop area. This is in good agreement with the fact that once the Mullins effect is removed from the mechanical response, the hysteresis loop is only due to viscosity.

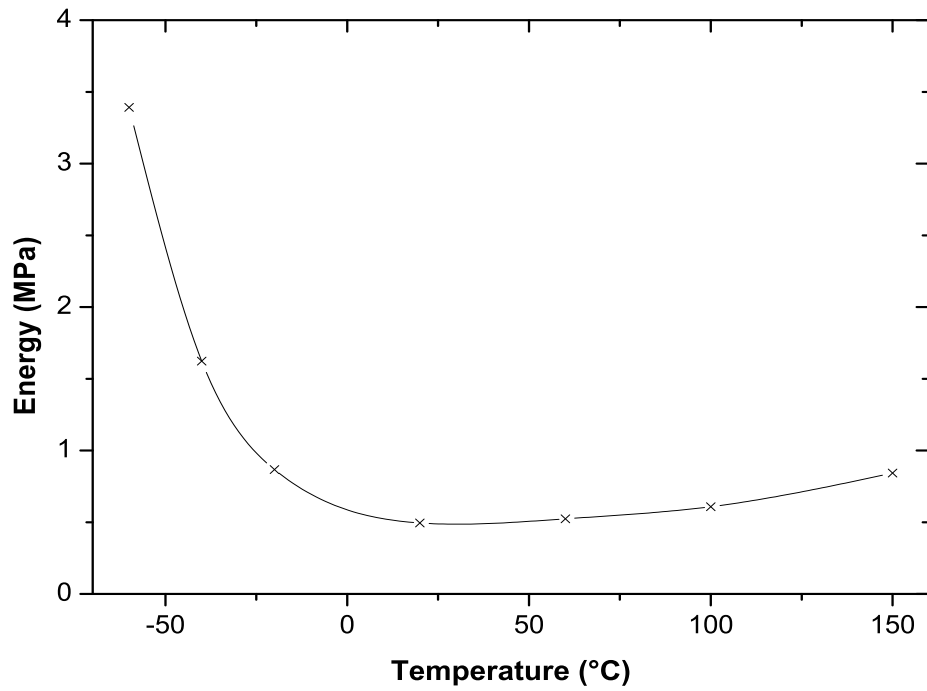


Figure 2.12: Energy corresponding to the hysteresis loop for the unfilled silicone at different temperatures for a strain of 50%.

The fact that hysteresis loops obtained in the first cycles are not influenced by the temperature means that the Mullins effect is mainly responsible. Indeed, contrarily to hysteresis due to viscosity (see Fig. 2.14), Mullins effect observed in filled silicone rubber is not significantly dependent on the temperature.

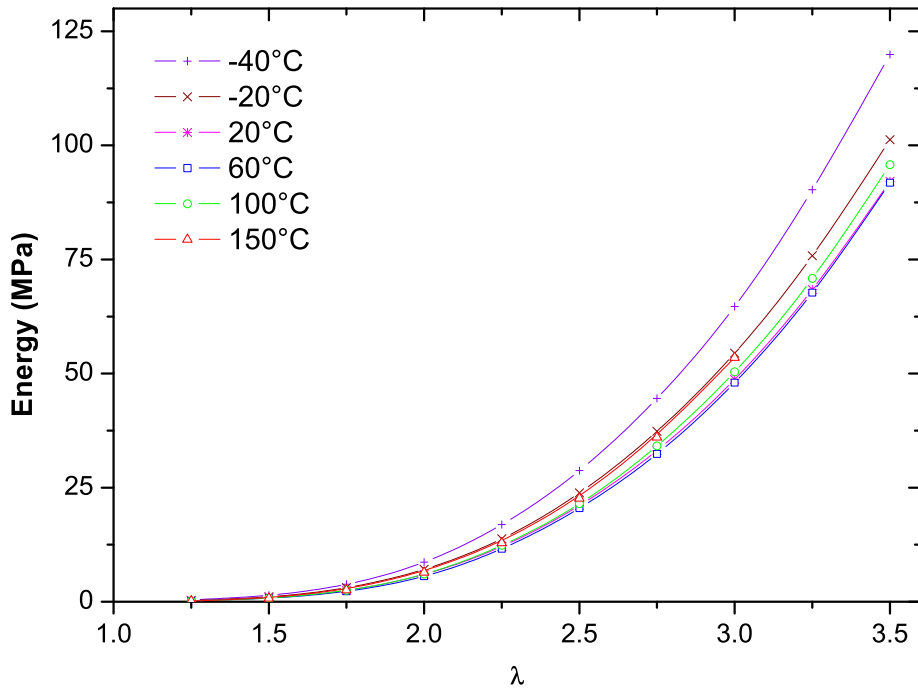


Figure 2.13: Energy corresponding to the hysteresis loop during the first cycle for the filled silicone at different temperatures.

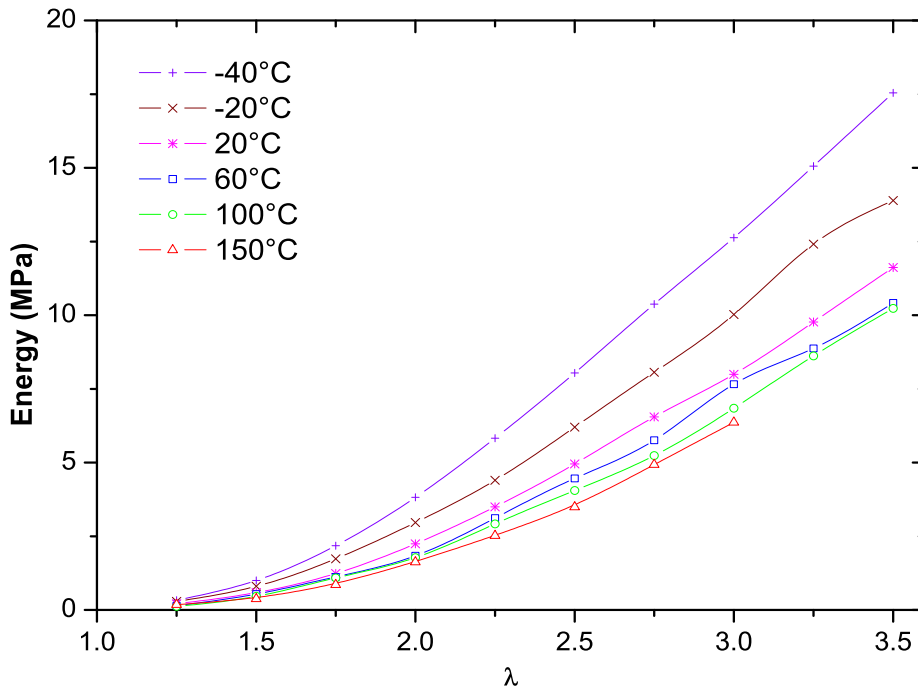


Figure 2.14: Energy corresponding to the hysteresis loop during the second cycle (*i.e.* after stress softening), for the filled silicone at different temperatures.

2.5 Conclusions

This study investigated the effects of temperature on the mechanical properties of filled and unfilled silicone rubbers, especially on hyperelasticity, mechanical hysteresis, stress

softening and stress relaxation. Results show that the stabilized behaviour of silicone rubbers depends quasi-linearly on the temperature. This is not true for the other phenomena. Typically in filled silicone rubber, the magnitude of hysteresis, stress relaxation and stress softening decrease by increasing the temperature. Moreover, up to 60°C, the temperature does not alter the stress softening. For these reasons, the modeling of phenomena involved in the deformation of rubbers should account for the non-linear dependence of these phenomena on the temperature. Consequently, this study opens a new way for the modeling of classical phenomena observed in rubbers, more particularly for the modeling of the Mullins effect, whose softening function should depend on a decreasing and asymptotic function of the temperature. Further work in this field is currently being carried out by the authors.

2.6 Conclusions of the chapter

In order to consider applications of a NiTi silicone rubber composite with temperature variations, the variations of mechanical behavior of the silicone rubber have to be considered, especially if the temperature tends to its crystallization one. Far from this temperature, it depends on the quantity of silicone rubber used for the elaboration of the composite. Indeed, as the influence of the NiTi is more important than the silicone and that the NiTi strongly reacts with temperature, the variations of behavior of the silicone rubber with temperature could be negligible if there is not a lot of silicone rubber. Moreover, for biomedical applications, the temperature variations allowed are very low, so even if the silicone could be used as an isolator for the NiTi and could be used with a larger range of temperature, it could not be very large, and the variations of mechanical behavior in a little range of temperature are very low, as seen in this chapter.

Hyperelasticity with rate-independent microsphere hysteresis model for rubberlike materials

Due to the typical properties of the NiTi shape memory alloy, composites made of NiTi are often considered to be used as actuators. Actuators are mainly used under cyclic loading, either mechanical, electrical or thermal. Thus, in order to model the mechanical behavior of a NiTi silicone rubber composite, some aspects of the two materials have to be taken into account. For the silicone rubber, during cyclic tests, some phenomena are observed: stress softening [Mullins, 1948], mechanical hysteresis and viscosity. In order to consider a great number of cycles, the study of the Mullins effect is not really relevant as it occurs only during the first cycles. Moreover, a lot of authors already proposed models investigating it [Beatty and Krishnaswamy, 2000; DeSimone *et al.*, 2001; Chagnon *et al.*, 2004; Diani *et al.*, 2006b]. However, mechanical hysteresis is still observed after several of cycles of deformation in rubberlike materials. This phenomenon was also observed in the mechanical response of the composite during cyclic tensile tests (appendix A), for each cycle of deformation. Therefore, in order to simulate the mechanical behavior of such a composite, the mechanical hysteresis has to be taken into account. For this purpose, this chapter presents a model proposed to take into account the rate-independent mechanical hysteresis of rubberlike materials.

A monodimensional equation taking into account the rate-independent mechanical hysteresis is proposed in this chapter. This equation is extended to 3D representation by means of the directional approach. Recently, some constitutive equations were proposed to model this stress softening with such a method, in order to represent the anisotropy, initial or induced by the Mullins effect [Machado *et al.*, 2014; Rebouah *et al.*, 2013], that is why a similar approach is used here in order to extend the model to a 3D representation.

T. Rey, G. Chagnon, D. Favier, J.-B. Le Cam

Published in Computational Materials Science 90 (2014) 89-98.

The mechanical behavior of elastomers strongly differs from one to another. Among these differences, hysteresis upon cyclic load can take place, and can be either rate-dependent or rate-independent. In the present paper, a microsphere model taking into account rate-independent hysteresis is proposed and applied to model filled silicone rubbers behavior.

The hysteresis model is based on a combination of monodimensional constitutive equations distributed in space. The behavior of each direction is described by a collection of parallel spring slider elements. The sliders are Coulomb dampers with non-zero break-free force in tension. This model is tested on a filled silicone rubber by the way of uniaxial tensile and pure shear tests. The mechanical response of the material is well predicted for such tests. Finally, the constitutive equations are implemented in the finite element software ABAQUS. Calculation results highlight good performances of the proposed model.

3.1 Introduction

The study and modeling of the mechanical behavior of rubber-like materials have been widely studied in last decades due to the increasing number of industrial applications, such as vibration isolators, tires or shock absorbers, non exhaustively. Classically, rubbers are filled by mineral fillers in order to improve their physical properties. The addition of fillers typically implies an increase of stiffness and a reinforcement of crack growth resistance [Ambacher *et al.*, 1991; Rigbi, 1980]. However, it also induces numerous additional effects [Ambacher *et al.*, 1991; Rigbi, 1980]. Among them, one can cite the stress softening, which mainly occurs between the first and second loads, and often called the Mullins effect [Mullins, 1948] (which can rarely be observed in unfilled rubbers too [Diani *et al.*, 2009]), the stress relaxation and the mechanical hysteresis (unload different from load).

The load and unload responses of filled rubber differ during cyclic tests. Even if this evolution is mainly due to the Mullins effect during the first cycle, a difference between load and unload responses is still observed once the material is softened, *i.e.* after the first cycle. This phenomenon, so-called hysteresis, can depend on the strain rate [Amin *et al.*, 2006], the crosslinks density [Bergstrom and Boyce, 1998] or the temperature [Rey *et al.*, 2013a].

Several micromechanism-inspired approaches of the hysteresis phenomenon were proposed in the literature, based on different physical considerations. To the opinion of Bergström and Boyce [Bergstrom and Boyce, 1998], hysteresis is induced by the viscous reptation of elastically inactive macromolecules. This type of micromechanism has also motivated a micro-sphere approach Miehe and Göktepe [2005], where hysteresis is considered to be due to the fillers entanglement. Some authors considered that a part of the broken cross-links can be re-formed upon unload D'Ambrosio *et al.* [2008]. More recently, the idea of a successive breakdown of filler clusters taking place during a load, and of a complete re-aggregation of the filler particles taking place during an unload was proposed Lorenz and Klüppel [2012]. This implies filler-induced hysteresis.

According to either the physical or the phenomenological approach used, different viscoelastic models with or without damage were proposed to take into account the hysteresis (for example Kaliske and Rothert [1998]; Miehe and Keck [2000]; Diani *et al.* [2006b]). A classical hypothesis of the proposed constitutive models is the multiplicative split of the deformation gradient into elastic and inelastic parts [Bergstrom and Boyce, 1998; Simo, 1987; Lion, 1996; Reese and Govindjee, 1998; Linder *et al.*, 2011]. Other approaches used a history dependent function to account for the hysteresis [Dorfmann and Ogden, 2003].

Even though most of the papers focused on the viscoelastic behavior of the material,

some of them studied the rate-independent hysteresis [D'Ambrosio *et al.*, 2008; Kaliske and Rothert, 1998; Dorfmann and Ogden, 2003; Vandenbroucke *et al.*, 2010]. To distinguish stress-softening and hysteresis, most of the authors removed the Mullins effect from the material behavior by carrying out beforehand several cycles [Bergstrom and Boyce, 1998; Lion, 1996].

This paper focuses on the quasi-static modeling (*i.e.* the rate independent behavior) of hysteresis effect after stress-softening. The aim of this work is to propose a directional method able to represent the difference between load and unload, easily extendable to anisotropy and well-adapted to the implementation in a finite element code.

The different mechanical tests carried out on a filled silicone rubber and the results obtained are presented in part 3.2. The theoretical background to model hysteresis is introduced in part 3.3. In part 3.4, experimental data are compared with simulations and results are discussed. Part 3.5 presents model implementation in a finite element code and calculation results obtained in case of heterogeneous test. Finally, concluding remarks close the paper.

3.2 Experimental setup

3.2.1 Materials

The material considered here is a filled silicone rubber Bluestar RTV 3428. Its mechanical properties were previously investigated Rey *et al.* [2013a]; Machado *et al.* [2010, 2012] and it was shown that this material exhibits stress-softening, occurring mainly during the first load, hysteresis and temperature dependent behavior.

3.2.2 Loading conditions

Two types of classical tests are carried out, uniaxial tensile tests and pure shear tests. These tests are performed using a Gabo Eplexor 500N. For the uniaxial tensile tests, the length, width and thickness of the specimens are 12, 2 and 2 mm, respectively and a 25 N load cell is used. For the pure shear tests, the length, width and thickness of the specimens are 2, 40 and 2 mm, respectively and a 500 N load cell is used. Several tests were carried out at different strain rates on the considered material, and it was observed that no significant difference can be observed for strain rates lower than $\dot{\lambda} = 1.67 \times 10^{-3} \text{ s}^{-1}$. As a consequence, to assume quasi-static conditions, the tests of this paper are performed at a low strain rate, *i.e.* $\dot{\lambda} = 1.67 \times 10^{-3} \text{ s}^{-1}$.

In order to distinguish mechanical hysteresis from Mullins effect, a preconditioning test is carried out on each specimen to remove the stress softening from the mechanical behavior. This procedure is classically applied in the literature to ensure test repeatability [Bergstrom and Boyce, 1998; Lion, 1996; Dorfmann and Ogden, 2004]. In the present study, preconditioning consists in performing 5 cycles of load unload to a stretch of $\lambda = 3$. Results of uniaxial tensile tests are presented in figure 3.1 a), in terms of the nominal stress versus the stretch λ . Figure 3.1 b) shows that there is no more stress softening between the 4th and 5th cycles proving that 5 cycles are sufficient to remove the Mullins

effect from the mechanical behavior of the silicone rubber. The results are quite similar for planar tensile tests and are not reported here.

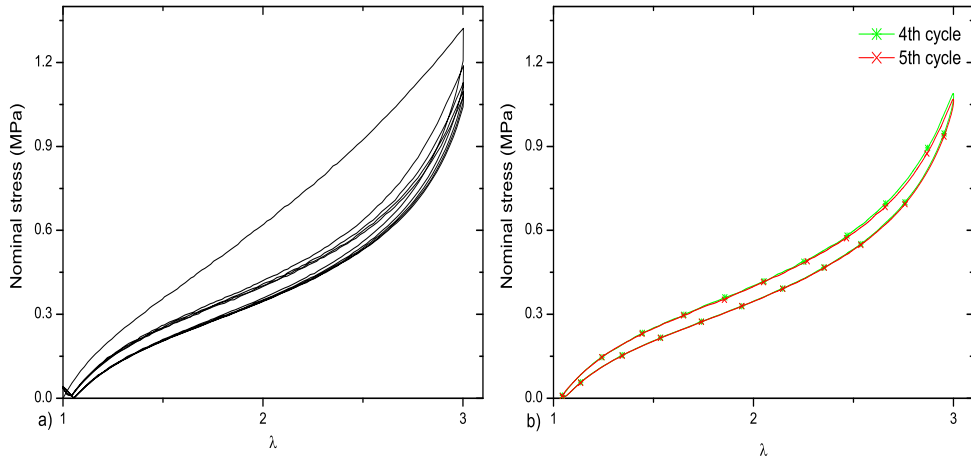


Figure 3.1: Preconditioning test to remove the stress softening during an uniaxial tensile test, with a) the five first cycles and b) the fourth and fifth cycle, at a stretch of $\lambda=3$.

3.2.3 Experimental results

Uniaxial tensile test is first carried out with increasing load cycles. These cycles are performed to $\lambda = 1.5, 2$ and 2.5 (see histogram in figure 3.2). It can be observed in figure 3.2 a) that there is a difference between loads and unloads, and that this phenomenon increases with increasing stretch. It is worth noting that there is still a very few residual strain.

A similar planar tensile test is performed, with three cycles to $\lambda = 1.5, 2$ and 2.5 . The results of this test are presented in figure 3.2 b). The curve is quite similar as for the uniaxial tensile test, the only difference is the stress level that is higher for the planar tensile test.

Two additional non-classical uniaxial tensile and planar tensile tests are performed to study the hysteresis phenomenon. The first test (called 'nc1' in the following) is a load-unload major loop with two hysteresis loops during the load and the unload. The second test ('nc2') is also a load-unload tensile test with a hysteresis sub-loop inside a first loop during the load. Figure 3.3 presents the histograms and results of these tests. Once again, it can be seen that the stress level is higher for planar tensile tests. In the 'nc2' test, the size of the hysteresis sub-loop is smaller than the size of the hysteresis loop, whereas for the 'nc1' test the four hysteresis loops seem to have the same size.

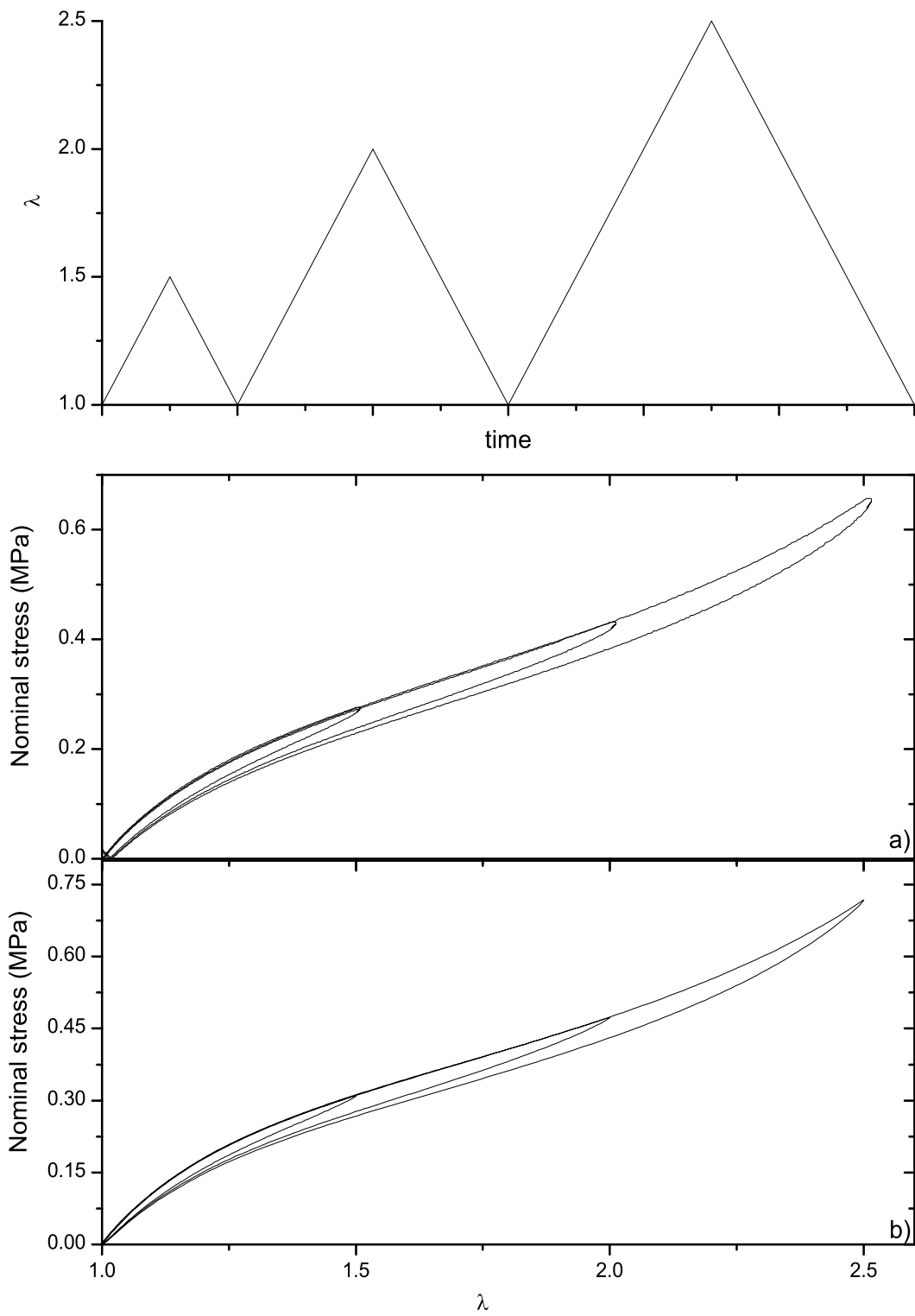


Figure 3.2: Evolution of the hysteresis during a tensile test for a) uniaxial tensile test and b) planar tensile test.

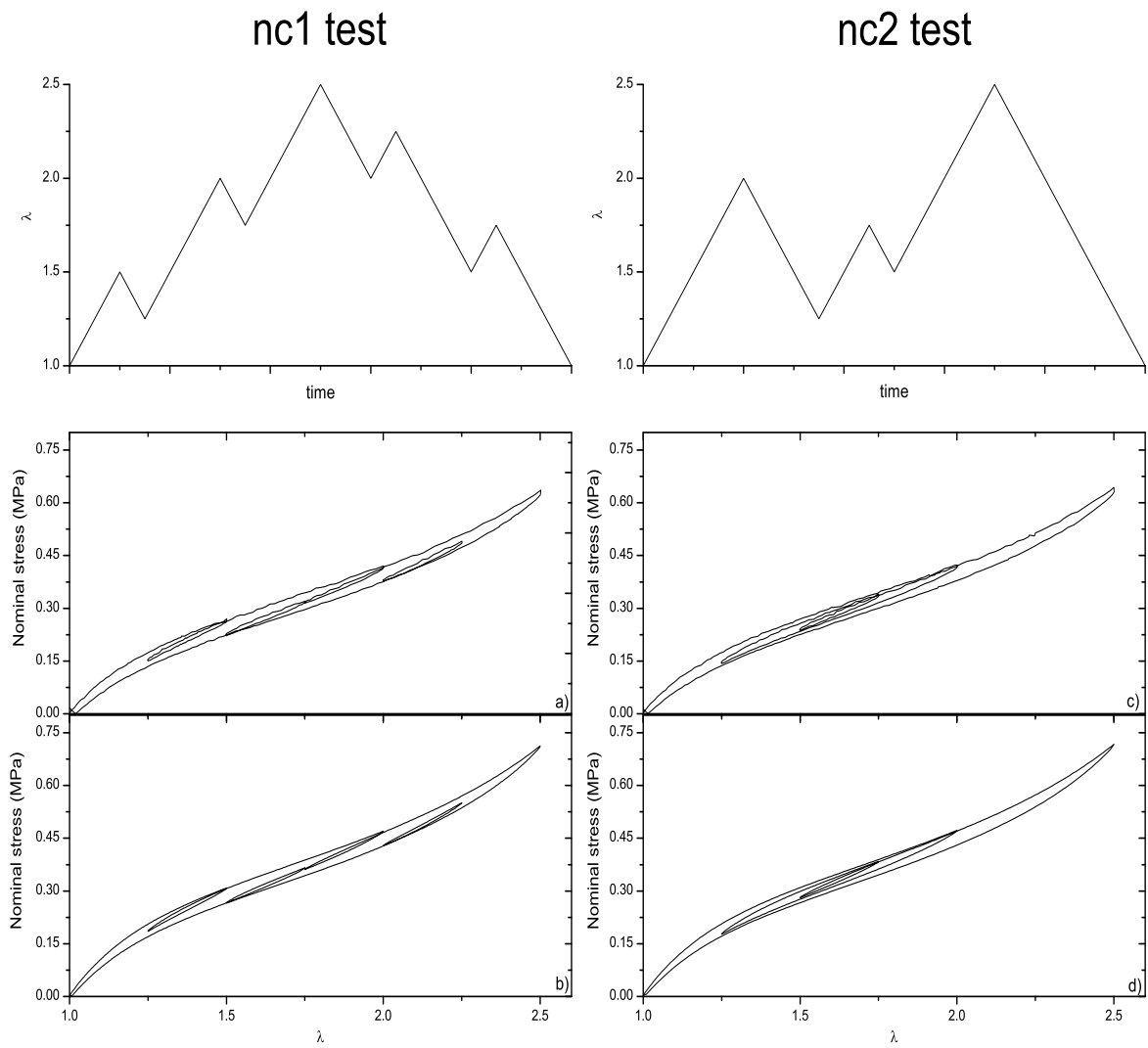


Figure 3.3: Results of a) uniaxial load-unload tensile test and b) planar tensile load-unload test with four hysteresis loops and of c) uniaxial load-unload tensile test and d) planar tensile load-unload test with a hysteresis loop inside another one.

3.3 Theory

3.3.1 Motivation

As mentioned above, hysteresis is a phenomenon whose physical mechanisms are still not clearly understood. Similarly to the other elastomers, silica filled silicone rubbers exhibit a hysteresis loop in terms of the stress-strain relationship [Rey *et al.*, 2013a]. The hysteresis loop is not observed when the silicone rubber is unfilled [Rey *et al.*, 2013a], showing that hysteresis is not due to macromolecular network deformation but to fillers, more especially to interactions between fillers and rubber matrix [Montes *et al.*, 2010]. Similar results are observed in other elastomers, for which hysteresis can also be wrongly attributed to viscosity. Indeed, phenomena that are rate-independent in a given range of strain rates and whose effects are different between load and unload induce a hysteresis loop. This is for instance the case in natural rubber, for which hysteresis loop is due to strain-induced crystallization and not to viscosity [Samaca Martinez *et al.*, 2013a, b].

3.3.2 Decomposition of the material behavior

According to the previous motivations, the model for filled silicone rubber should take into account the macromolecular network elasticity and the hysteresis generated by the difference in the fillers/rubber matrix interactions between load and unload. Classically, models reported in the literature are based on the decomposition of the material behavior into two or three parts. A first hyperelastic part is completed with a viscous part, a damage part or both of them. Even though such a representation is usually used for elastomers, it was also used for other materials, for example to study metallic alloys and magnetization phenomena [Favier and Guélin, 1985; Favier *et al.*, 1992].

In the present paper, this approach is adapted to represent time independent hysteresis in elastomers. For this purpose, the model is only composed of a hyperelastic part, represented by a nonlinear spring, and a hysteretic part, represented by infinity of spring-friction slider association.

The hyperelastic Cauchy stress σ_{hyper} and the hysteresis Cauchy stress σ_{hyst} are added to obtain the mechanical response of the material. By assuming that the material is incompressible, the total stress writes as follows:

$$\boldsymbol{\sigma} = \boldsymbol{\sigma}_{hyper} + \boldsymbol{\sigma}_{hyst} - p\mathbf{I} \quad (3.1)$$

where p is the hydrostatic pressure, introduced for taking account the incompressibility, and \mathbf{I} is the identity tensor.

3.3.3 Hyperelastic part

The hysteresis part described in the next section can be used with any hyperelastic constitutive equations. As an example, in the present paper, a classical model with a Biderman strain energy Biderman [1958] is used. This constitutive equation is given by:

$$W_{hyper} = c_{10}(I_1 - 3) + c_{20}(I_1 - 3)^2 + c_{30}(I_1 - 3)^3 + c_{01}(I_2 - 3) \quad (3.2)$$

where c_{10} , c_{20} , c_{30} and c_{01} are material parameters, I_1 and I_2 are respectively the first and second strain invariants of the right Cauchy-Green tensor $\mathbf{C} = \mathbf{F}^T \mathbf{F}$, and \mathbf{F} is the deformation gradient. These invariants are defined as $I_1 = \text{tr}(\mathbf{C})$ and $I_2 = \frac{1}{2}(\text{tr}(\mathbf{C})^2 - \text{tr}(\mathbf{C}^2))$.

3.3.4 Hysteresis part

3.3.4.1 General form

For an initially isotropic material, the chains constituting the silicone rubber are assumed to be equidistributed in space. In this case, an infinity of directions in the space is used to model the material behavior [Wu and Van der Giessen, 1993]. However, an infinite number of directions leads to integration problems, and consequently a discrete number of directions is a better solution. This is the reason why the 42 directions proposed by Bažant and Oh [1986] is used in the present study. The directional repartition is classically used to model rubber-like materials, especially to describe Mullins effect [Diani *et al.*, 2006a; Itskov *et al.*, 2006; Rebouah *et al.*, 2013; Zéhil and Gavin, 2013]. Nevertheless, any other spatial repartition can be chosen. By the way, initial directions unit vectors $\mathbf{a}_0^{(i)}$ are defined, and initial direction tensors $\mathbf{A}_0^{(i)}$, current direction vectors $\mathbf{a}^{(i)}$ and tensors $\mathbf{A}^{(i)}$ and normalized current direction tensor $\mathbf{A}_n^{(i)}$ are respectively calculated by:

$$\begin{aligned}\mathbf{A}_0^{(i)} &= \mathbf{a}_0^{(i)} \otimes \mathbf{a}_0^{(i)} \\ \mathbf{a}^{(i)} &= \mathbf{F} \mathbf{a}_0^{(i)} \\ \mathbf{A}^{(i)} &= \mathbf{a}^{(i)} \otimes \mathbf{a}^{(i)} \\ \mathbf{A}_n^{(i)} &= \frac{\mathbf{a}^{(i)} \otimes \mathbf{a}^{(i)}}{\|\mathbf{a}^{(i)}\| \|\mathbf{a}^{(i)}\|}\end{aligned}\tag{3.3}$$

The main advantage of using a microsphere repartition is that only monodimensional constitutive equations are needed to represent a tridimensional behavior. No tridimensional tensorial generalization of constitutive equations is required as in Vandenbroucke *et al.* [2010].

The time independent model used for the hysteretic part is shown in figure 3.4. In this representation, the effect of interactions between fillers and the rubber matrix is considered to be different during load and unload. As a consequence, a non classical friction slider is introduced and its behavior is presented in figure 3.5. First, when loaded in tension, the stretch and stress increase until the stress reaches the limit value of the slider, and stays then equal to this value. When it is relaxed, the stretch and stress decrease until the stress reaches zero and stays constant to this value. So the system comes back to its initial configuration by creating a hysteresis loop as illustrated in figure 3.5 a). Second, when the network is initially compressed, the stretch decreases but the stress stays equal to zero. When the load in compression is relaxed, the network starts to resist and the stress increases until the sliding limit is reached (cf. figure 3.5 b)). This represents a friction slider that is only used in one loading direction.

Each direction is represented by the scheme presented in figure 3.4. The sum of an infinity of linear spring with different sliders can be represented by a global equation. Here, the repartition proposed by Favier and Guélin [1985] is used, leading

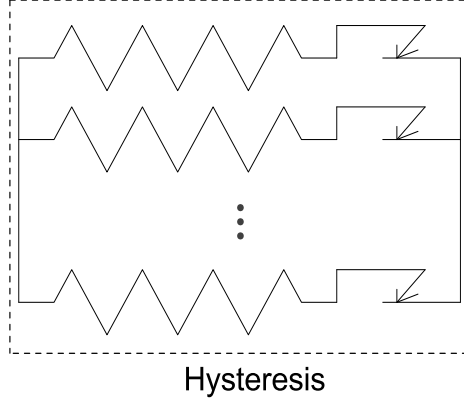


Figure 3.4: Representation of the hysteresis rheological model in a direction.

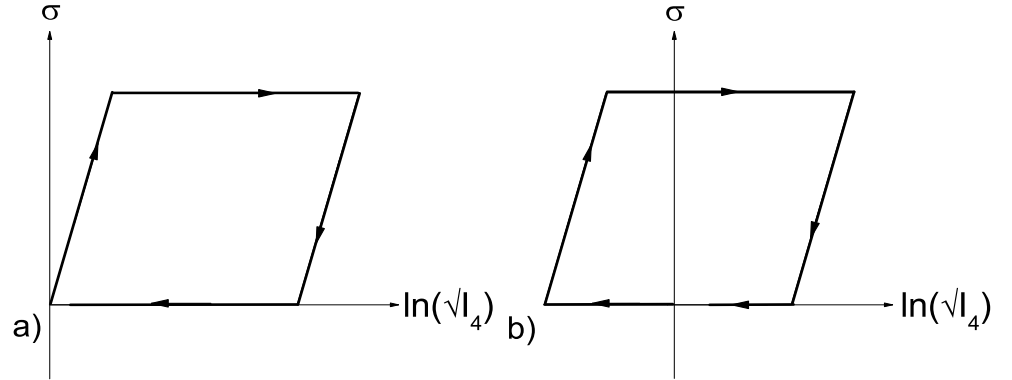


Figure 3.5: Behavior of an a) initially stretched and b) initially compressed spring-friction slider association in series.

to a global formulation given by:

$$\sigma^{(i)} = \sigma_0 \tanh \frac{E \ln \sqrt{I_4^{(i)}}}{\sigma_0} \quad (3.4)$$

where $\sigma^{(i)}$ is the stress in the considered direction i , E is equivalent to an initial slope, σ_0 is the maximum reachable stress by the hysteresis part of each direction, and $I_4^{(i)}$ is the fourth invariant of the right Cauchy-Green tensor \mathbf{C} . It is defined by $I_4^{(i)} = \text{tr}(\mathbf{C}\mathbf{a}_0^{(i)})$, and it represents the square of the elongation $\lambda^{(i)}$ in direction $\mathbf{a}_0^{(i)}$. It is worth noting that by affecting a different value of E and σ_0 in each direction it is possible to induce anisotropy.

The stress tensor is finally obtained by summing the contributions of each direction:

$$\boldsymbol{\sigma}_{hyst} = \sum_{i=1}^{42} \omega_i \sigma^{(i)} \mathbf{A}_n^{(i)} \quad (3.5)$$

where ω_i are the weight corresponding of each direction Bažant and Oh [1986].

3.3.4.2 Inversion point

To create a difference between load and unload, inversion points are introduced. A similar method was already used by Vandenbroucke *et al.* [2010]; Masing [1926]; Guélin [1980]; Wack *et al.* [1983]; Favier [1988]; Rey *et al.* [2013b]. An inversion point is defined as a change in the load evolution (load to unload or conversely). The creation of inversion points is detected by means of an evaluation of the sign of the expression $(\sigma^{(i)} - \sigma_{inv}^{(i)}) dI_4^{(i)}$, where $dI_4^{(i)}$ is the fourth invariant increment. An algorithm introducing the conditions of add and erase of inversion points is presented in figure 3.6 [Guélin, 1980]. This algorithm is applied for each direction of the microsphere hysteresis model. It is worth noting that

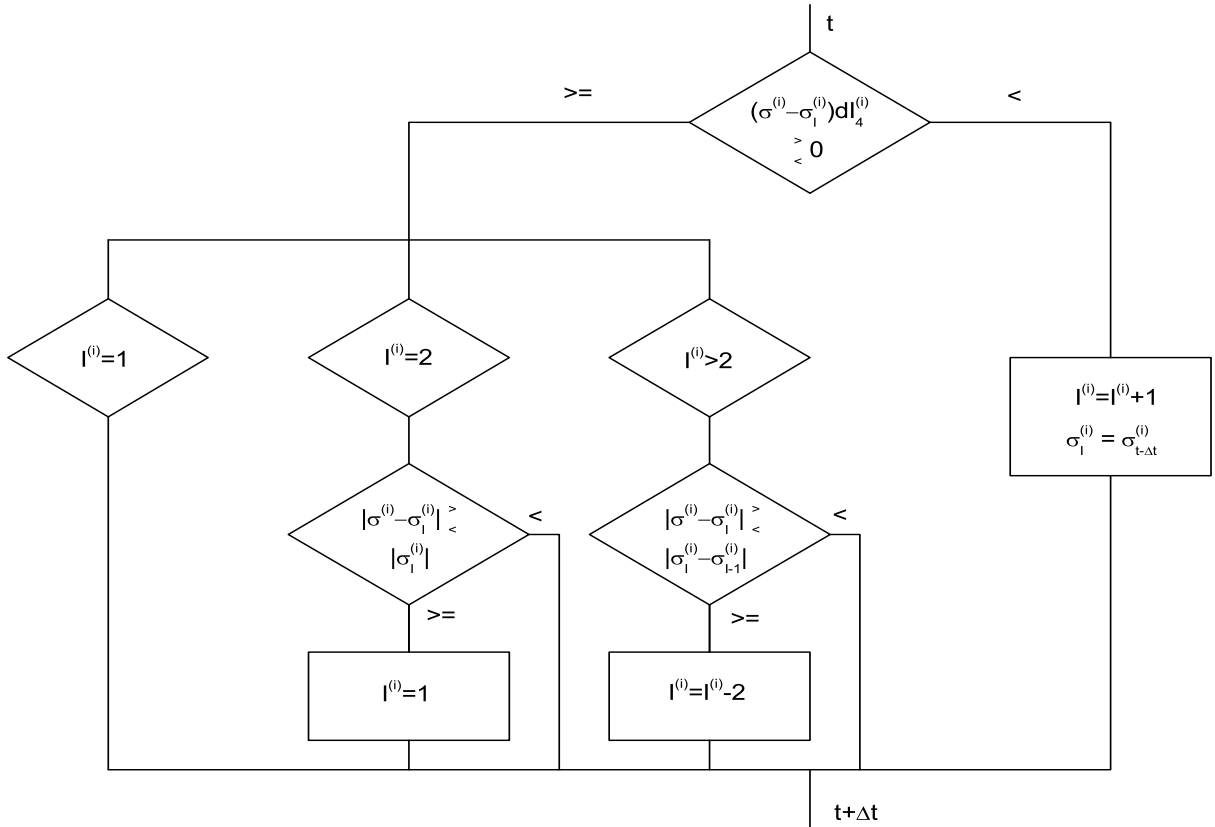


Figure 3.6: Management of inversion points algorithm, where σ is the current stress, $\sigma_I^{(i)}$ is the stress of the inversion point, $I^{(i)}$ is the number of inversion points and $dI_4^{(i)}$ is the difference between the values of $I_4^{(i)}$ at the current and the previous step time.

the first point of a test is considered as inversion point, so there is always at least one inversion point. Once the inversion points introduced, the monodimensional constitutive

equation presented in Eq. (4) becomes:

$$\sigma^{(i)} = \sigma_{inv}^{(i)} + \sigma_0 \tanh \frac{E \left(\ln \sqrt{I_4^{(i)}} - \ln \sqrt{I_{4inv}^{(i)}} \right)}{\sigma_0} \quad (3.6)$$

where $\sigma_{inv}^{(i)}$ and $I_{4inv}^{(i)}$ are respectively the stress and the square of the elongation of the inversion point.

Two examples are presented to illustrate the inversion points. Figure 3.7 a) shows a load-unload curve with creation of an inversion point. At the end of the first load, an

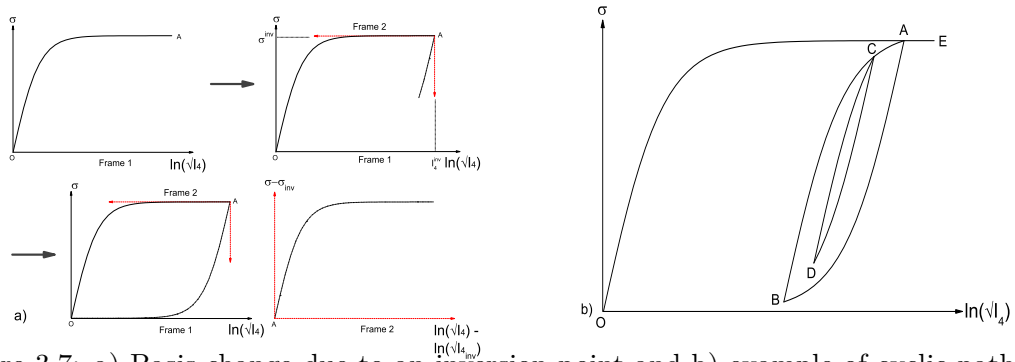


Figure 3.7: a) Basis change due to an inversion point and b) example of cyclic path in a direction.

inversion point is created (point A). Thus, the unload stress-strain curve AO is the same as the load curve OA, but in a frame with point A as origin and the axes oriented so that $(\sigma^{(i)} - \sigma_{inv}^{(i)})$ and $\left(\ln \sqrt{I_4^{(i)}} - \ln \sqrt{I_{4inv}^{(i)}} \right)$ are positive on AO. Thus, the unload curve is the same as the load curve by a similarity of ratio -1. By this way, the scheme presented by the friction sliders is totally respected and allows us to extend easily the model to more complex cyclic paths. Let us consider a subloop in a first loop, as represented in figure 3.7 b). The first load (OA) is defined as previously by Eq. (6). There is next a first unload (AB), defined by Eq. (6), with the point A as new inversion point. Then, a second load occurs (BC), where the point B is a new inversion point, followed by a second unload (CD, with C a new inversion point). These second load and unload are also governed by Eq. (6), with for inversion point the points B and C respectively. Finally, a third and last load is performed (DE). This reload is defined by Eq. (6), considering the point D as inversion point until joining the point C. At this point (C), the subloop CDC is closed and points C and D are no more considered as inversion points. The third load takes now the point B for inversion point in Eq. (6) and is the extension of BC until joining point A. At point A, the subloop ABA is closed and there is only O as inversion point. As a consequence, the end of this reload AE is the extension of OA and is governed by Eq. (6). The load DE is so made by three different arcs. Table 3.1 summarizes the equations and inversion points governing the different segments of this curve.

This kind of method was already used to model hysteresis in rubberlike materials by Vandenbroucke *et al.* [2010]; Favier *et al.* [1997], where similar inversion points were implemented in a tridimensional model, with a tridimensional criterion, but it was validated

segment	equation	list of inversion points	inversion point used in eq. (6)
OA	(6)	O	O
AB	(6)	O A	A
BC	(6)	O A B	B
CD	(6)	O A B C	C
DC	(6)	O A B C D	D
CA	(6)	O A B	B
AE	(6)	O	O

Table 3.1: Equations and inversion points in figure 3.7 b).

on uniaxial tensile and compression tests only. The originality of the present approach is that the inversion points are only controlled by a monodimensional criterion.

The model is based on the use of friction pads, with inversion points. This idea was already used for other kind of materials, and the thermodynamical dissipation of the scheme was already studied by Guélin [1980]. The principle stays the same for the present study.

3.4 Results and discussion

The constitutive equations previously described are used to simulate a filled silicone behavior with the Matlab software. The parameters are identified from experimental data obtained during the uniaxial tensile test presented in section 2. They are reported in table 3.2. These parameters are then used to simulate the other experimental tests.

c_{10} (MPa)	c_{20} (MPa)	c_{30} (MPa)	c_{01} (MPa)	E (MPa)	σ_0 (MPa)
0.1	-0.003	0.0008	0.025	0.94	0.1

Table 3.2: Values of the material parameters fitted on experimental data.

The simulation of the first uniaxial tensile test with three increasing cycles is presented in figure 3.8 a). This figure shows that the silicone behavior is well predicted by the model for this experiment as the curves are nearly confounded. The prediction of the hysteresis loops size (calculated as the difference between load and unload) presented in figure 3.8 b) is satisfactory for this test. Figure 3.9 a) shows the simulation of the planar tensile test with three increasing cycles. It can be seen that the stress level reached is overestimated in this case, which is due to the hyperelastic constitutive equation, overestimating the stress for the planar tension for elongation between $\lambda = 2$ and 4. This was previously explained by Marckmann and Verron [2006]. However, the hysteresis loop size prediction is acceptable despite the overestimation of the stress, as presented in figure 3.9 b). A more complete constitutive equation could be used to obtain best predictions of the hyperelastic behavior of the material, but the aim of this paper is to show that the hysteresis part can be adapted for all the existing hyperelastic constitutive equations, so the Biderman model is kept as it gives reasonable predictions.

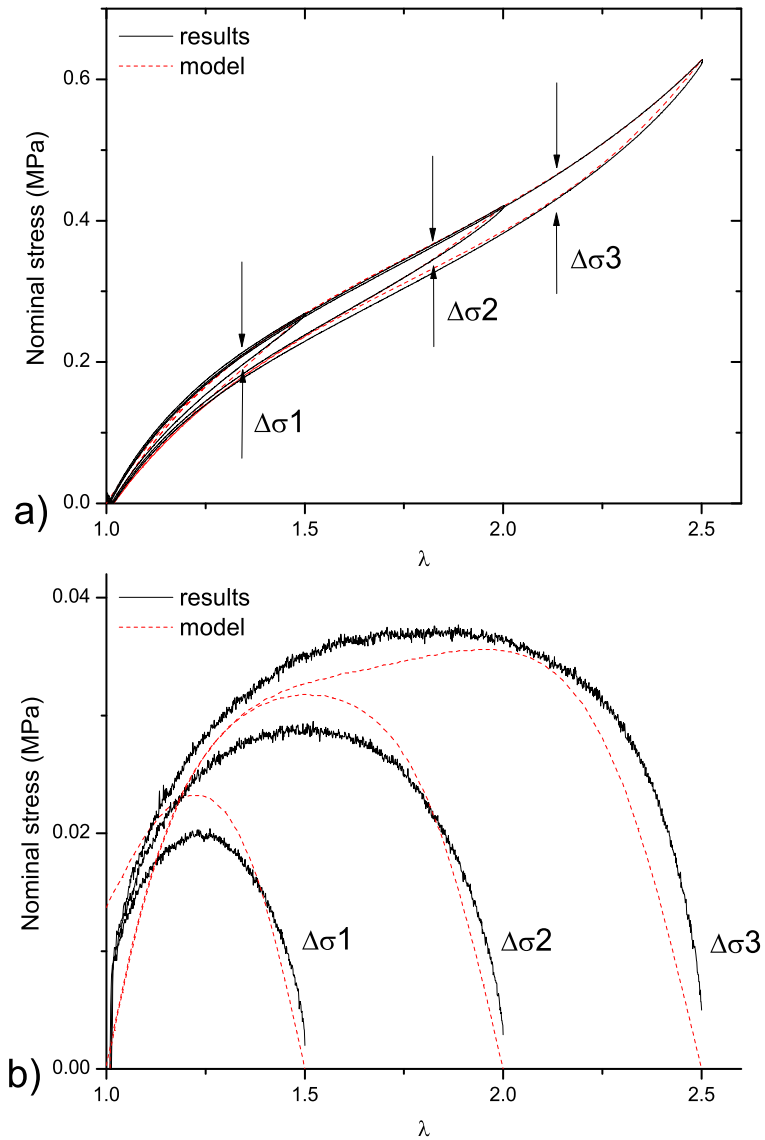


Figure 3.8: Uniaxial tensile test with increasing cycle. Experiments (full lines) and simulation (dashed lines) (a) and comparison of the experimental and simulated hysteresis loops size (b).

The results of the simulations of 'nc1' for uniaxial and planar tensile tests are presented in figures 3.10 a) and b) respectively. The sizes of the hysteresis loops are very well predicted, as shown in figures 3.10 c) and d). Figures 3.10 e) and f) show respectively the results of the simulation of the test 'nc2' for uniaxial and planar tensile tests. Even if the size of the greater hysteresis loop is not perfectly predicted in the two cases, the size of the little one is the same for the model as for the experiments and the prediction of the material behavior is acceptable.

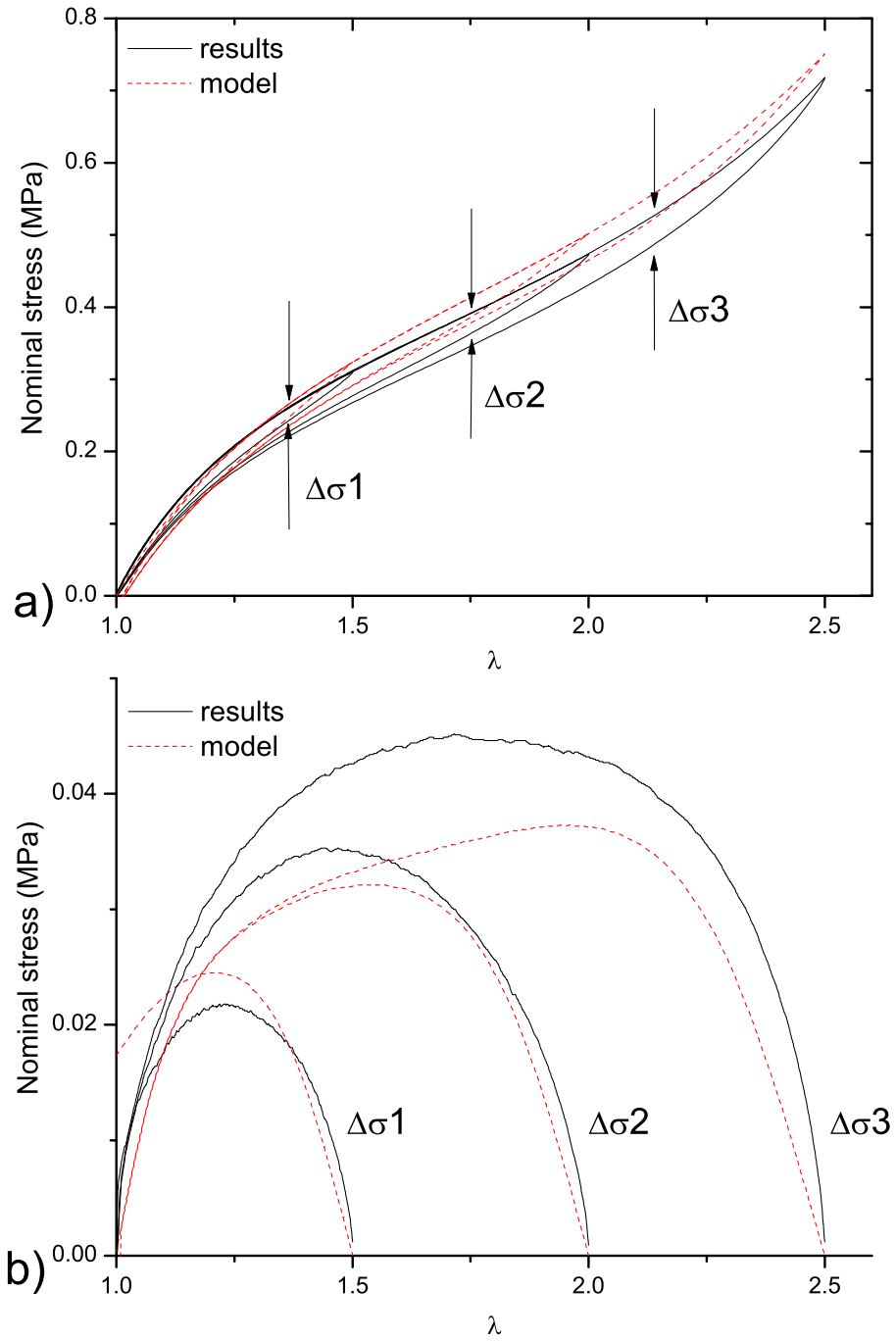


Figure 3.9: planar tensile test with increasing cycle. Experiments (full lines) and simulation (dashed lines) (a) and comparison of the experimental and simulated hysteresis loops size (b).

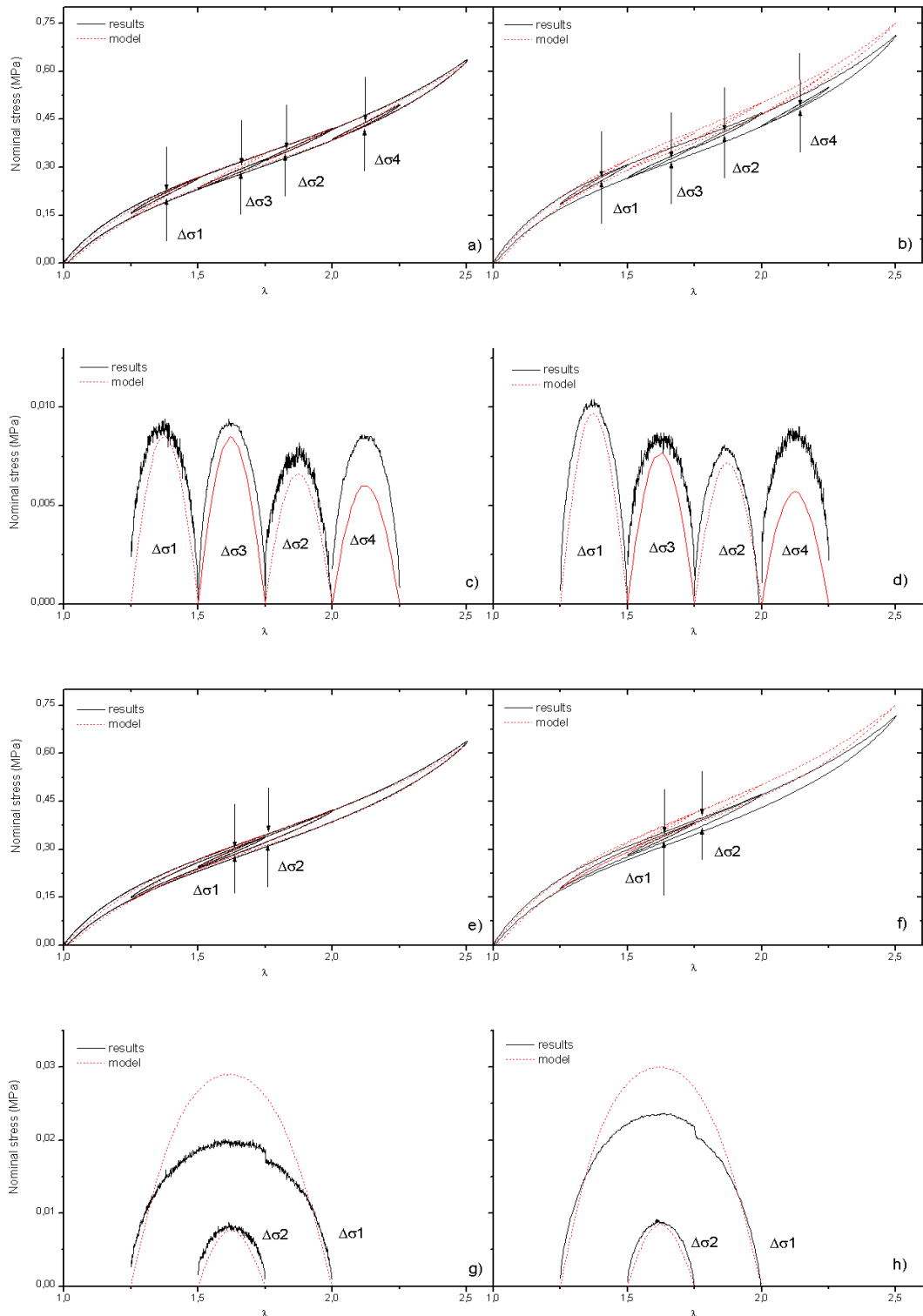


Figure 3.10: Uniaxial tensile (a) and planar tensile (b) tests with four hysteresis loops and uniaxial tensile (e) and planar tensile (f) tests with a hysteresis loop inside another one. Comparison of the experimental and simulated hysteresis loops size (c), (d), (g) and (h).

3.5 Extension of the model

3.5.1 Finite element implementation

The model proposed in this paper is developed in the framework of isotropic and anisotropic invariants. To take into account the material incompressibility, a quasi-incompressible formulation of the strain energy function is needed:

$$W = \bar{W}(\bar{I}_1, \bar{I}_2, \bar{I}_4^{(i)}) + U(J) \quad (3.7)$$

where $\bar{I}_1 = I_3^{-1/3} I_1$, $\bar{I}_2 = I_3^{-2/3} I_2$ and $\bar{I}_4^{(i)} = I_3^{-1/3} I_4^{(i)}$ are the incompressible invariants and $J^2 = I_3 = \det(\mathbf{C})$ the square of the volume variation. The model is implemented into the finite element software Abaqus via a UMAT. Details about the numerical implementation of $\bar{I}_1, \bar{I}_2, \bar{I}_4^{(i)}$ constitutive equations can be found in Federico *et al.* [2008]; Holzapfel and Gasser [2001]; Ogden [2003]; Sun [2005]. The finite element implementation needs the calculation of the second Piola-Kirchhoff stress tensor and the Lagrangian deviatoric tangent modulus. They are calculated by means of the strain energy derivation. The second Piola-Kirchhoff stress tensor is defined as:

$$\mathbf{S} = \bar{\mathbf{S}} + \mathbf{S}^{vol} = 2 \frac{\partial \bar{W}}{\partial \mathbf{C}} + J \frac{\partial U}{\partial J} \mathbf{C}^{-1} \quad (3.8)$$

The volume variation function considered here is the classical function $U(J) = K(J - 1)^2$, used in Abaqus, where K is a material parameter. The general form of the Lagrangian tangent modulus is presented in Kaliske [2000]. The isochoric part of the Lagrangian deviatoric tangent modulus is calculated by:

$$\bar{\mathbb{C}}^L = 2 \frac{\partial \bar{\mathbf{S}}}{\partial \mathbf{C}} \quad (3.9)$$

In the case of a strain energy function of the form $W = W_1(I_1) + W_2(I_2) + \sum W_4(I_4)$, it is expressed by:

$$\bar{\mathbb{C}}^L = 4 \left(\frac{\partial}{\partial \mathbf{C}} \left(\bar{W}_{,1} \frac{\partial \bar{I}_1}{\partial \mathbf{C}} \right) + \frac{\partial}{\partial \mathbf{C}} \left(\bar{W}_{,2} \frac{\partial \bar{I}_2}{\partial \mathbf{C}} \right) + \sum_{i=1}^n \frac{\partial}{\partial \mathbf{C}} \left(\bar{W}_{,4}^{(i)} \frac{\partial \bar{I}_4^{(i)}}{\partial \mathbf{C}} \right) \right) \quad (3.10)$$

where $\bar{W}_{,i}$ is the strain energy derivation with respect to the i^{th} incompressible invariant of the right Cauchy-Green tensor.

This tangent modulus is expressed as a function of the derivatives of the strain energy function with respect to the first, second and fourth invariants. The results of the derivations with respect to the first and second invariants are immediate, they are the derivatives of W_{hyper} of equation (2). For the fourth invariant the first and second derivatives are given without inversion points respectively by:

$$\bar{W}_{,4} = \sigma_0 \tanh \left(\frac{E \ln \left(\sqrt{\bar{I}_4^{(i)}} \right)}{\sigma_0} \right) \quad \bar{W}_{,44} = \frac{E}{2\bar{I}_4^{(i)}} \left(1 - \tanh^2 \left(\frac{E \ln \left(\sqrt{\bar{I}_4^{(i)}} \right)}{\sigma_0} \right) \right) \quad (3.11)$$

These derivations change when an inversion point occurs, and in this case the first and second derivatives of the strain energy function with respect to the fourth invariant are

given respectively by:

$$\begin{aligned} \bar{W}_{,4} &= \left(\sigma_{inv}^{(i)} + \sigma_0 \tanh \left(\frac{E \left(\ln \left(\sqrt{\bar{I}_4^{(i)}} \right) - \ln \left(\sqrt{\bar{I}_{4inv}^{(i)}} \right) \right)}{\sigma_0} \right) \right) \\ \bar{W}_{,44} &= \frac{E}{2\bar{I}_4^{(i)}} \left(1 - \tanh^2 \left(\frac{E \left(\ln \left(\sqrt{\bar{I}_4^{(i)}} \right) - \ln \left(\sqrt{\bar{I}_{4inv}^{(i)}} \right) \right)}{\sigma_0} \right) \right) \end{aligned} \quad (3.12)$$

It is to note that the tangent modulus has to be expressed in the Eulerian configuration. For this purpose, push-forward operation is carried out [Kaliske, 2000].

In order to check the model performance and convergence, a non-classical test was carried out on a diabolo structure, meshed with approximately 6000 elements (8-node linear bricks with hybrid formulation, *i.e.* linear in displacement and constant in pressure) and using the same material parameters as previously (cf. table 3.2). It is subjected to a torsion load of 300° , next partially unloaded and reloaded, and finally totally unloaded (see the histogram in figure 3.11). The moment function of the angle is plotted in figure 3.11.

In each element, each direction $\mathbf{a}_0^{(i)}$ of the hysteresis model experiences inversion points during the simulated test. In order to illustrate that, the direction $\mathbf{a}_0^{(i)} = \mathbf{z}$ is considered in the initial configuration. Pictures 1 to 5 represent the number of inversion points in that direction in each element at different times (see the histogram in figure 3.11). It is worth noting that before the end of the first load (picture 1), some elements have already one or two inversion points meaning that the considered direction was loaded and unloaded several times during the torsion load, due to the important rotation of the material directions and to the volume conservation of the considered elements. An increase of the inversion points number is observed during the first three steps, and it decreases after the closure of the hysteresis loop. It should be noted that a maximum principal elongation value of 2.5 is obtained (the parameters were identified for this elongation during the uniaxial tensile test in the previous section), proving the good performance of the proposed model.

3.5.2 Higher hysteresis simulation

The material used in this paper to validate the proposed model presents a weak rate-independent hysteresis. In order to show the possibilities of fitting of higher hysteresis, a simulation with greater parameters of hysteresis is presented in this section. The parameters for the hyperelastic constitutive equation are kept (table 3.2), and the hysteretic parameters E and σ_0 are taken equal to 5 and 1 respectively. Three increasing cycles of load-unload tensile are simulated, from a stretch equal to 1 to a stretch equal to 1.5, 2 and 2.5 successively. Results of this simulation is presented in figure 3.12, and it can be seen that the difference between load and unload is more important than previously.

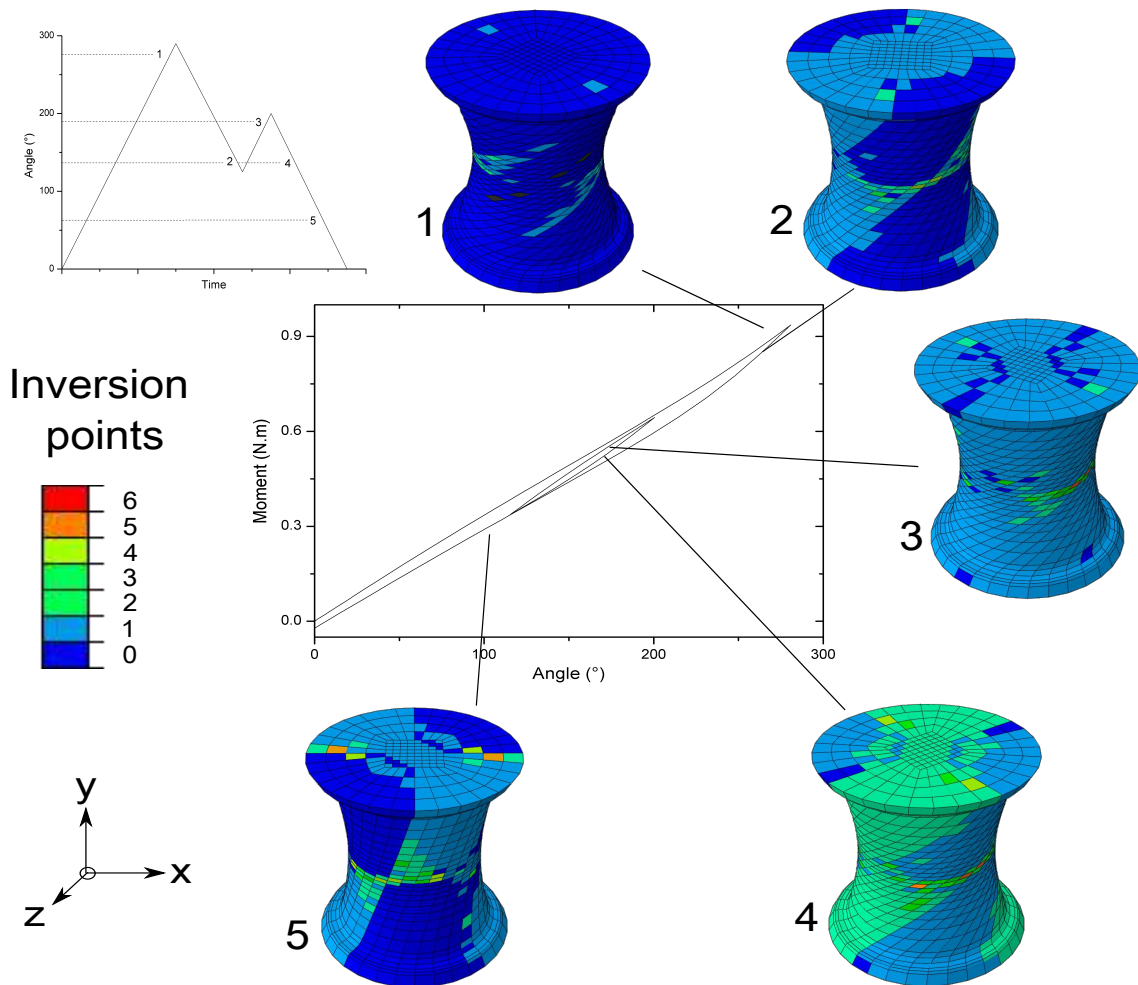


Figure 3.11: Results of a numerical torsion test on the diablo. Evolution of the number of inversion points along the cyclic torsion test.

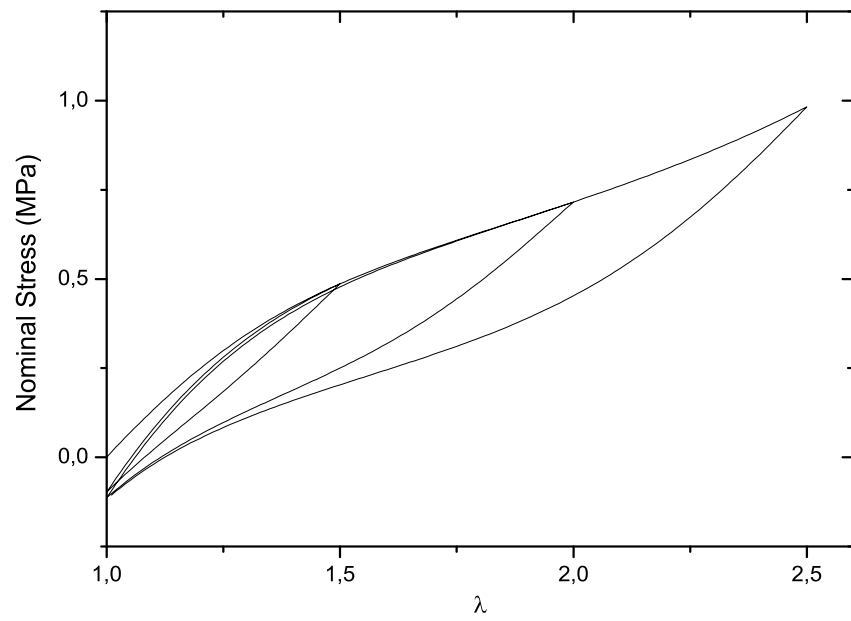


Figure 3.12: Simulation of a cyclic tensile test with a great hysteresis.

3.6 Conclusions

In this paper, a microsphere model was proposed to take into account rate-independent hysteresis. This method is based on the decomposition of rubber-like mechanical behavior into a first usual hyperelastic model and a second hysteresis model. This method can be adapted to any existing hyperelastic constitutive equations. This was illustrated by associating the hysteresis part with a classical Biderman constitutive equation. To describe the hysteretic behavior, a non classical friction slider was introduced, representing a different behavior in tension and compression, and it must be initially loaded in tension to bring a contribution.

The predictions of the model are compared to experimental data in case of uniaxial tensile and planar tensile tests. The hysteresis is well predicted for these tests, even though the hyperelastic part cannot perfectly predict the elastomer mechanical behavior for planar tensile tests.

A finite element implementation was carried out on the software ABAQUS. A test on a non-classical geometry with a complex loading and an important number of elements shows the good efficiency of the model. A simulation with high hysteresis loops show the possibilities of adaptation of the model for different materials. Further investigations about the association of hyperelastic mechanical response, Mullins effect and hysteresis are currently carried out by the authors.

3.7 Conclusions of the chapter

In order to model the mechanical behavior of NiTi silicone rubber structures, and especially cyclic behavior, the mechanical hysteresis has to be taken into account for both the two materials. Therefore, a model was proposed to take into account the mechanical hysteresis of rubberlike materials. In a first approach, only the rate-independent mechanical hysteresis was taken into account.

The aim was to propose a model which can be used with any existing model of hyperelastic constitutive equation. As shown in the second chapter, a shape setting or a pre-stress can be applied to a NiTi silicone rubber composite, which therefore could exhibit an anisotropic mechanical behavior. Thus, the present model has to be easily extendable to anisotropy. For this purpose, a microsphere repartition was used, as recently done in numerous models of the literature. A monodimensional rheological model composed of springs and friction sliders associations was proposed, and the corresponding constitutive equations are developed using the method of the inversion points to generate differences between loads and unloads. These monodimensional constitutive equations are then generalized by means of the microsphere to obtain the 3D model. This model was associated to a classical Biderman hyperelastic model to check its performance. Uniaxial and planar tensile tests were performed, with different hysteresis loops. These tests were simulated with the proposed model. The areas of the different hysteresis loops are well predicted by the model.

Additional investigations were carried out. First, it was observed that great hysteresis loops could be simulated with this model, showing its good performance and its adaptability to different rubberlike materials. Second, the proposed model was also implemented in the finite elements software ABAQUS by means of a UMAT. A torsion test was simulated on a diabolo structure, and a good convergence was obtained, showing the efficiency of this model.

Using this model, a first approach of the mechanical cyclic behavior of the silicone rubber during cyclic loads can be obtained. Obviously, other characteristics of the silicone rubbers (*i.e.* stress softening, viscosity...) have to be taken into account for more accurate results.

A directional approach to model superelastic behavior of NiTi Shape Memory Alloy (SMA)

4.1 Introduction

The remarkable mechanical and thermomechanical behavior of Shape Memory Alloys (SMAs) and especially of equiatomic Nickel-Titanium (NiTi) [Otsuka and Ren, 2005] makes them very interesting for numerous and various applications. Indeed, SMAs undergo large deformations and exhibit unique properties for metallic materials, like superelasticity, shape memory effect and two ways memory effect. Superelasticity of SMAs is now a well known phenomenon. Schematically, this particular mechanical behavior during a tension test is represented by two different elastic parts separated by a stress plateau. The first elastic part corresponds to the mechanical response of the material in its austenitic state. Then, a phase change occurs in the material, resulting in a plateau without stress variations with the strain increase. Once the material is totally transformed (or almost totally), its mechanical response becomes elastic again, corresponding to the mechanical response of the material in its martensitic state. During the unload, the opposite mechanical response occurs (*i.e.* martensite elasticity, reverse transformation, austenite elasticity), and some hysteresis is observed between the load and unload plateaus. Some plasticity can occur after the martensitic elasticity, but SMAs are often just used in the range of superelasticity for their different applications.

A lot of investigations were performed on NiTi specimens and a lot of models were also proposed for superelasticity of shape memory alloys [Matsuzaki and Naito, 2004; Khandelwal and Vidyashankar, 2009]. Most of them cannot accurately take into account the behavior during major and subloop cycles. Experimentally, this effect has been well studied by Orgéas *et al.* [1997] by carrying out simple shear deformation tests through both major and subloop cycles. The aim of the present chapter is to propose a model for the superelastic behavior of NiTi taking into account these effects. For this purpose, a model is proposed using a directional approach classically used to model elastomers. In particular, this approach was used to model the Mullins effect [Mullins, 1948], *i.e.* stress softening between first and second loads, which was observed to induce anisotropy in filled elastomers [Machado *et al.*, 2012]. In order to model this phenomenon, Machado *et al.* [2014] recently proposed a model with a space discretization in a finite number of directions

proposed by Bažant and Oh [1986]. By this way, a monodimensional constitutive equation is proposed in each direction and an integration of all the directions is performed in order to represent the global behavior of the considered material. Such an approach was used for example to model Mullins effect [Diani *et al.*, 2006a; Rebouah *et al.*, 2013; Rebouah and Chagnon, 2013], viscoelasticity [Miehe and Göktepe, 2005] or the mechanical hysteresis [Rey *et al.*, 2014a].

In this chapter, this formalism is adapted to model the behavior of a shape memory alloys, and especially the superelasticity. Section 4.1 of the chapter presents the model proposed for the elasto-plasticity. This model is extended for the superelastic behavior of a SMA in section 4.2. Section 4.3 presents the results of experimental tests of the literature, and the model predictions of these results. Finally, some concluding remarks close the paper.

4.2 Standard elasto-plasticity model

In this section, the directional approach is used to model usual 3D elasto-plastic behavior.

4.2.1 Monodimensional elasto-plastic model

The monodimensional elasto-plastic model presents a pure hysteresis behavior. This is the behavior observed by the mechanistic model represented in figure 4.1 b). The elastic plastic behavior of a spring slider couple is shown in figure 4.1 a). Taking an infinite number of couples, as shown in figure 4.1 b), permits to have a distribution function, and to avoid a fracture point between the elasticity and the threshold. Such a mechanistic

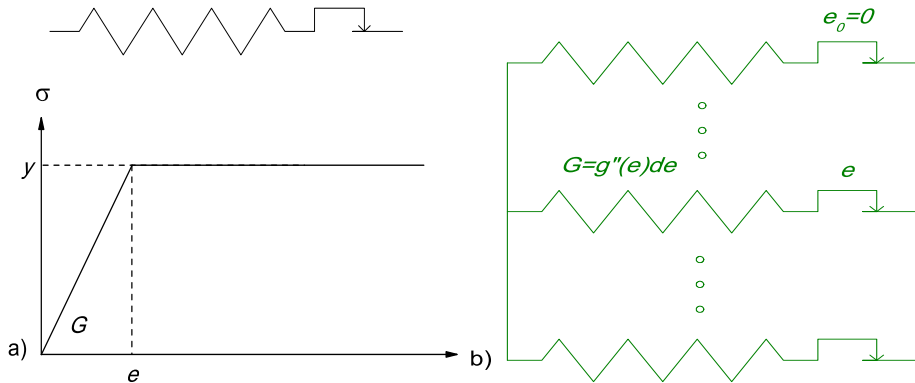


Figure 4.1: Spring slider associations.

model was already used in the literature, as by Guélin [1980], Wack *et al.* [1983] and Favier [1988], and the present work is inspired from these works.

The mechanical response of the rheological model presented in figure 4.1 b) with initial tension, followed by an unload and a reload, is represented in figure 4.2.

Each spring slider couple presents a first slope, controlled by the rigidity G of the spring, and a limit value given by the slider, which can be given by the yield stress y or the yield strain $e = y/G$. Considering that $g''(e)de$ is the rigidity coefficient for the spring-slider couples having their yield strain between e and $e + de$, it appears for the first

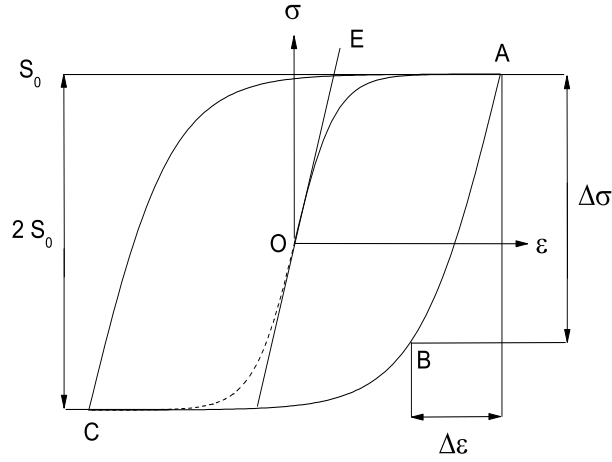


Figure 4.2: Representation of the elasto-plastic part of the mechanical response of the material, initially stretched.

load (OA in figure 4.2) that for a given strain ε_0 :

$$\sigma_0(\varepsilon_0) = \int_0^{\varepsilon_0} e g''(e) de + \int_{\varepsilon_0}^{\infty} \varepsilon_0 g''(e) de \quad (4.1)$$

The first part of the addition represents the sum of the spring-slider associations for which the yield was already reached, and the second part is the sum of the others. Thus, the equation (4.1) can be developed and written under the following form:

$$\begin{aligned} \sigma_0(\varepsilon_0) &= \int_0^{\varepsilon_0} e g''(e) de + \varepsilon_0 \int_0^{\infty} g''(e) de - \varepsilon \int_0^{\varepsilon} g''(e) de \\ &= \varepsilon_0 \int_0^{\infty} g''(e) de + \varepsilon_0 g'(\varepsilon_0) - \int_0^{\varepsilon_0} g'(e) de - \varepsilon_0 \int_0^{\varepsilon_0} g''(e) de \\ &= G_0 \varepsilon_0 - g(\varepsilon_0) \end{aligned} \quad (4.2)$$

with:

$$G_0 = \int_0^{\infty} g''(e) de \quad \text{and} \quad g(0) = g'(0) = 0$$

During the unload (AB, figure 4.2), taking for origin the last point of the first load (A), the strain decrease is equal to $\Delta\varepsilon$, with $\Delta\varepsilon = \varepsilon - \varepsilon(A)$. Noting ω a similarity ratio equal to 2, the stress decrease $\Delta\sigma$, with $\Delta\sigma = \sigma - \sigma(A)$, can be expressed by:

$$\begin{aligned} \Delta\sigma(\Delta\varepsilon) &= \int_0^{\Delta\varepsilon/\omega} \omega e g''(e) de + \int_{\Delta\varepsilon/\omega}^{\infty} \Delta\varepsilon g''(e) de \\ &= \int_0^{\infty} \Delta\varepsilon g''(e) de - \int_0^{\Delta\varepsilon/\omega} \Delta\varepsilon g''(e) de + \int_0^{\Delta\varepsilon/\omega} \omega e g''(e) de \\ &= G_0 \Delta\varepsilon - \Delta\varepsilon g'(\Delta\varepsilon/\omega) + [\omega e g'(e)]_0^{\Delta\varepsilon/\omega} - \int_0^{\Delta\varepsilon/\omega} \omega g'(e) de \\ &= G_0 \Delta\varepsilon - \Delta\varepsilon g'(\Delta\varepsilon/\omega) + \Delta\varepsilon g'(\Delta\varepsilon/\omega) - \omega g(\Delta\varepsilon/\omega) \\ &= G_0 \Delta\varepsilon - \omega g(\Delta\varepsilon/\omega) \end{aligned} \quad (4.3)$$

$$\Rightarrow \sigma - \sigma(A) = \omega \sigma_0(\Delta\varepsilon/\omega) \quad \text{with} \quad \Delta\varepsilon = \varepsilon - \varepsilon(A) \quad \text{and} \quad \omega = 2$$

Thus, the unload curve is deduced from the first one by a similarity of ratio $-\omega$. The point A is defined as the new reference state. This is the Masing rule [Masing, 1926].

The previous relation is valid during the unload until the point C. After C, the reference state becomes the point O and $\sigma - \sigma(O) = \omega(\Delta\varepsilon/\omega)$ with $\Delta\varepsilon = \varepsilon - \varepsilon(O)$ and $\omega = 1$.

It appears that the stress strain relation can always be written as:

$$\sigma - \sigma_{ref} = \sigma_0 \left(\frac{\varepsilon - \varepsilon_{ref}}{\omega} \right) \quad (4.4)$$

introducing the reference stress and strain of each branch or arc of a curve. Models using this method were already proposed in the literature [Guélin, 1980; Wack *et al.*, 1983; Favier, 1988], as for example in the elastomers field [Vandenbroucke *et al.*, 2010; Rey *et al.*, 2014a]. The creation of inversion points is detected by means of an evaluation of the sign of the expression $(\sigma - \sigma_{ref})d\varepsilon$, where $d\varepsilon$ is the strain increment. Figure 4.3 represents the process of determination of reference point between all the previously determined inversion points. The first point of a test (strain and stress equal to 0) is defined as first inversion

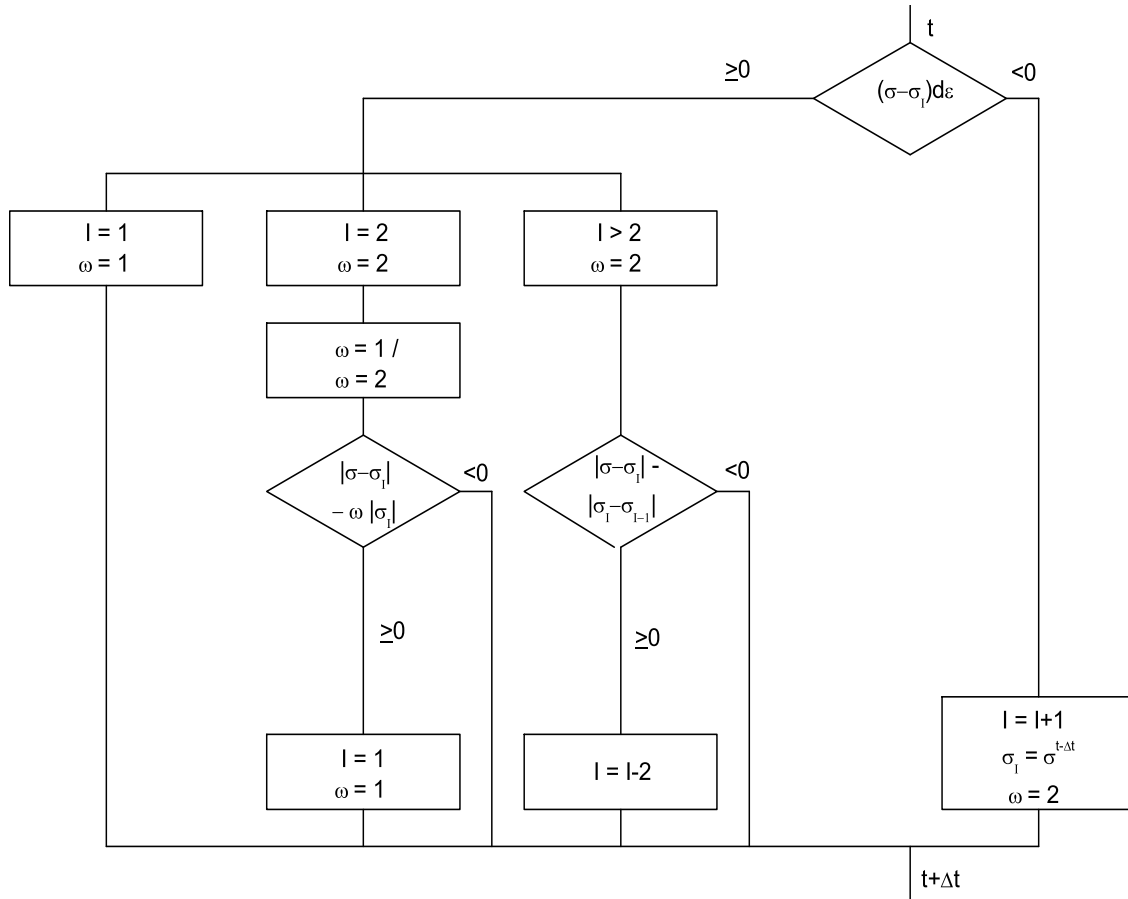


Figure 4.3: Management of inversion points algorithm, where σ and ε are respectively the current stress and strain, σ_I and ε_I are respectively the stress and strain of the inversion point, I is the number of inversion points, $d\varepsilon$ is the strain increment and ω is the similarity ratio.

point. The erasing process of inversion points depends on the number of inversion points still memorized, noted I . If there is two memorized inversion points ($I = 2$), *i.e.* during a first unload, the second inversion point is deleted if the absolute value of the difference between the current stress and the last inversion point stress reaches or exceeds two times

the absolute value of the last inversion point stress (point C in figure 4.2), as seen in figure 4.3. In this case, the following of the curve is the extension of a first load curve ($\sigma_{ref} = \sigma(I = 1)$, $\omega = 1$). If there is more than two inversion points ($I > 2$), two inversion points are deleted if the absolute value of the difference between the current stress and the last inversion point stress reaches or exceeds the absolute value of the difference between the last inversion point stress and the second last inversion point, *i.e.* a loop is closed (figure 4.3). A curve representing this process was presented in the previous chapter (figure 3.7) for a similarity ratio ω equal to 1 but the method stays the same.

An example of the rheological model presented previously, with the contribution of the inversion points, is represented by the following equation:

$$\dot{\sigma} = E \left(1 - \left(\frac{\sigma - \sigma_{ref}}{\omega S_0} \right)^c \right) \dot{\varepsilon} \quad (4.5)$$

with:

$$\omega = 1 \text{ for } I = 1 \quad \text{or} \quad \omega = 2 \text{ for } I > 1 \quad (4.6)$$

where E is the initial slope, σ the value of the stress, S_0 the threshold stress of the function, ε the strain, I the number of memorized inversion points and $\dot{\cdot}$ denotes the time derivative.

4.2.2 3D elasto-plasticity theory

As explained in the introduction, an approach with a discretization of the space and a 3D integration is used in this paper. This method is explained in the following.

4.2.2.1 Rubberlike materials formalism

The invariant formulation, classically used to model rubberlike materials, is reminded here.

The three first invariants are calculated from the right Cauchy-Green tensor \mathbf{C} , itself determined from the transformation gradient tensor \mathbf{F} , $\mathbf{C} = \mathbf{F}^T \mathbf{F}$, by:

$$\begin{aligned} I_1 &= tr \mathbf{C} \\ I_2 &= \frac{1}{2} \left((tr \mathbf{C})^2 - tr (\mathbf{C}^2) \right) \\ I_3 &= \det \mathbf{C} \end{aligned} \quad (4.7)$$

These invariants are used for isotropic models. In order to propose directional models, to take into account the anisotropy for example, considering initial directions \mathbf{a}_0 , invariants are calculated from the right Cauchy-Green tensor \mathbf{C} and from spatial initial directions tensor $\mathbf{A}_0 = \mathbf{a}_0 \otimes \mathbf{a}_0$. Particularly, the fourth invariant is often used, and it is calculated by:

$$I_4 = tr (\mathbf{C} \mathbf{A}_0) \quad (4.8)$$

It physically represents the square of the elongation in the considered direction.

Constitutive equations are sometimes split into a deviatoric and a spherical part in order to take into account of a possible volume variation. The deviatoric part represents the deformations without volume variation, and the volume variations are themselves represented by the spherical part. The deviatoric part is expressed using $\bar{I}_1 = I_1 I_3^{-1/3}$ and

$\bar{I}_2 = I_2 I_3^{-2/3}$, and the spherical part only depends on the third invariant, representing the volume variation. In such a formulation, the fourth invariant is expressed by $\bar{I}_4 = I_4 I_3^{-1/3}$.

In order to use monodimensional equations to model a 3D behavior, a unit sphere is decomposed in a finite number of n directions of the space, distributed along this sphere in order to represent its behavior as well as possible. Bažant and Oh [1986] proposed a n equal to 42 directions repartition, and a scheme representing an eighth of the unit sphere and the directions associated is presented in figure 4.4. Initial directions vectors $\mathbf{a}_0^{(i)}$,

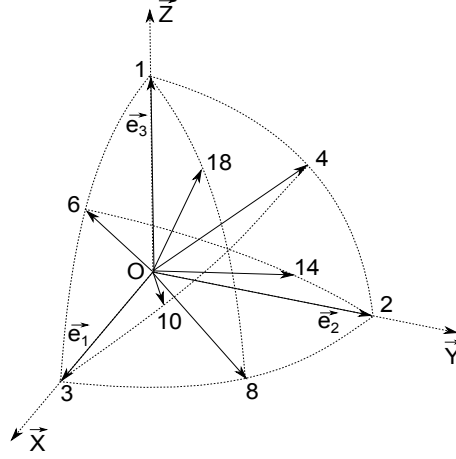


Figure 4.4: Scheme of the directions repartition on an eighth of the unit sphere.

with $i = 1 : 42$, are defined and given in Bažant and Oh [1986], and initial and current direction tensors, $\mathbf{A}_0^{(i)}$ and $\mathbf{A}^{(i)}$ respectively, are calculated by:

$$\begin{aligned}\mathbf{A}_0^{(i)} &= \mathbf{a}_0^{(i)} \otimes \mathbf{a}_0^{(i)} \\ \mathbf{A}^{(i)} &= \mathbf{a}^{(i)} \otimes \mathbf{a}^{(i)} = \mathbf{F}\mathbf{a}_0^{(i)} \otimes \mathbf{F}\mathbf{a}_0^{(i)}\end{aligned}\quad (4.9)$$

The current direction vectors and tensors are often normalized in order to be used for models:

$$\begin{aligned}\mathbf{a}_n^{(i)} &= \frac{\mathbf{F}\mathbf{a}_0^{(i)}}{\|\mathbf{F}\mathbf{a}_0^{(i)}\|} = \frac{\mathbf{a}^{(i)}}{\|\mathbf{a}^{(i)}\|} \\ \mathbf{A}_n^{(i)} &= \frac{\mathbf{F}\mathbf{a}_0^{(i)}}{\|\mathbf{F}\mathbf{a}_0^{(i)}\|} \otimes \frac{\mathbf{F}\mathbf{a}_0^{(i)}}{\|\mathbf{F}\mathbf{a}_0^{(i)}\|} = \mathbf{a}_n^{(i)} \otimes \mathbf{a}_n^{(i)}\end{aligned}\quad (4.10)$$

4.2.2.2 Adaptation to elasto-plasticity

This formalism is used in order to propose a 3D elasto-plasticity model using the monodimensional elasto-plastic equations previously presented. The strain in a direction is assumed to be the deviatoric logarithmic strain, expressed from the fourth invariant by:

$$\bar{\varepsilon}^{(i)} = \ln \left(\bar{\lambda}^{(i)} \right) = \ln \sqrt{\bar{I}_4^{(i)}} \quad (4.11)$$

where $\lambda^{(i)}$ is the elongation in the direction $\mathbf{a}_0^{(i)}$ and $\bar{\lambda}^{(i)} = \lambda^{(i)} J^{-1/3}$.

By the way of the elements previously given, the stress contribution of each direction can be calculated. Then, the deviatoric part of the stress tensor is obtained by:

$$\boldsymbol{\sigma}_{dev} = \sum_{i=1}^n \frac{\omega_i \sigma^{(i)}}{J} \left(\mathbf{A}_n^{(i)} - \frac{1}{3} \mathbf{I} \right) \quad (4.12)$$

where $J^2 = I_3$, and ω_i is the weight of each direction, given by Bažant and Oh [1986]. It is worth noting that the term in brackets ensures that the trace of the deviatoric part of the stress tensor is equal to 0.

The spherical part of the stress is then calculated by the expression:

$$\boldsymbol{\sigma}_{sph} = K \ln(J) \mathbf{I} \quad (4.13)$$

where K is a compressibility coefficient.

Finally, the total stress is obtained by adding the deviatoric and spherical parts:

$$\boldsymbol{\sigma} = \boldsymbol{\sigma}_{dev} + \boldsymbol{\sigma}_{sph} \quad (4.14)$$

4.2.2.3 Numerical tools

A numerical tool was developed in order to simulate tests performed in the principal directions. Thus, the components of the deformation gradient and stress tensors are:

$$\mathbf{F} = \begin{bmatrix} \lambda_1 & 0 & 0 \\ 0 & \lambda_2 & 0 \\ 0 & 0 & \lambda_3 \end{bmatrix} \quad \boldsymbol{\sigma} = \begin{bmatrix} \sigma_1 & 0 & 0 \\ 0 & \sigma_2 & 0 \\ 0 & 0 & \sigma_3 \end{bmatrix} \quad (4.15)$$

In the case of given kinematic, the resolution can be done immediately. If mixed conditions are imposed, an algorithm has to be used to solve the problem. In this case among the six components of \mathbf{F} and $\boldsymbol{\sigma}$, three are given and three are unknown. The different possibilities, depending on the considered test, are presented in table 4.1.

Uniaxial tension		Equibiaxial tension		Planar tension	
Given	Unknown	Given	Unknown	Given	Unknown
λ_1	σ_1	λ_1	σ_1	λ_1	σ_1
$\sigma_2 = 0$	λ_2	λ_2	σ_2	λ_2	σ_2
$\sigma_3 = 0$	λ_3	$\sigma_3 = 0$	λ_3	$\sigma_3 = 0$	λ_3

Table 4.1: Given and unknown components of \mathbf{F} and $\boldsymbol{\sigma}$ depending on the considered case.

For each step, the unknown elongations are initially taken equal to the corresponding elongation of the previous step. By the way of this estimation, the strains $\bar{\varepsilon}^{(i)} = \ln \sqrt{\bar{I}_4^{(i)}}$ in all directions are calculated, permitting to calculate the stresses in each of the 42 directions. The stress tensor can be therefore calculated using equations 4.12 to 4.14. Using the results for the stress component which has to be equal to zero, the corresponding elongation is calculated by means of a Newton-Raphson (N-R) algorithm. A new deformation gradient tensor is so obtained, and this process is again iterated, until the values of the stress which have to be equal to zero reach values inferior or equal to 10^{-10} .

This algorithm is schematically summarized in figure 4.5 for the case of planar tension with two imposed elongations (λ_1 imposed, $\lambda_2 = 1/\lambda_1$), and one stress component imposed ($\sigma_3 = 0$).

4.2.2.4 Simulations

Several simulations are presented in this part to illustrate the proposed model. The parameters used for these simulations are presented in table 4.2.

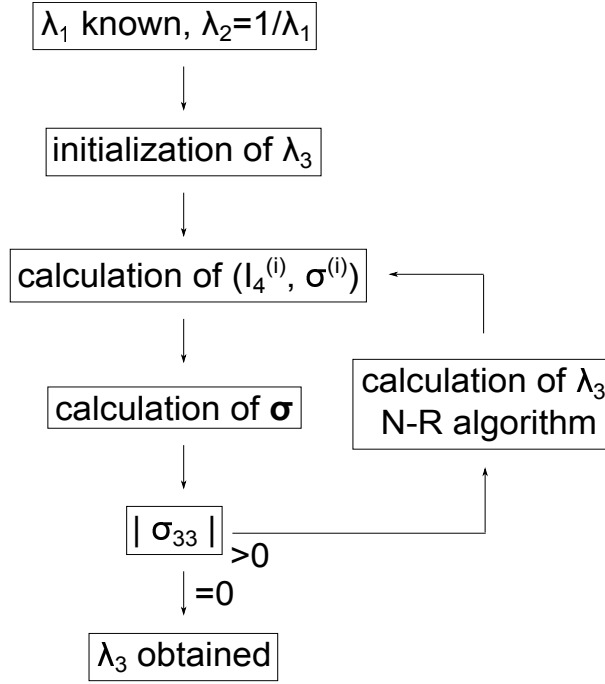


Figure 4.5: Resolution algorithm used in the case of a planar tension.

E (GPa)	S_0 (GPa)	K (GPa)
200	1	100

Table 4.2: Values of the parameters used for the simulations using the elasto-plasticity model.

Figure 4.6 presents the simulation of an uniaxial tension-compression test (table 4.1). The loading for this simulation is composed of a first load of 6% of strain ($\varepsilon_{11} = \ln \lambda_1$), an unload from 6 to -6%, and finally a reload from -6 to 6%. Figure 4.6 a) presents the tensile stress-strain curve of this simulation. The derivative of the tensile stress by the tensile strain, the strain in the orthogonal direction and the derivative of the lateral strain by the tensile strain are represented as function of the tensile strain in figure 4.6 b), c) and d) respectively.

An additional simulation of a complex cyclic uniaxial tensile test is performed. The results, presented in figure 4.7, show that the subloops of load are well represented, and that successive or interlocked subloops can easily be simulated with this model.

The same simulation as figure 4.6 was done for equibiaxial and planar tension (table 4.1), and the results are presented in figure 4.8 and 4.9, respectively.

A lot of observations can be done from these simulations, concerning i) the elasticity, ii) the plasticity and iii) some undesirable effects.

i) First, concerning the elasticity:

The compressibility coefficient K is known and equal to 100 GPa. The Young modulus (E) for the uniaxial test is observed in figure 4.6 b) to be equal to 73,5 GPa at the beginning of the simulation. By means of classical isotropic elasticity theory, the Young modulus (E) and Poisson's ratio (ν) values can easily be calculated for each test. The indice b denotes the variables concerning the equibiaxial test, and the shear modulus is noted G.

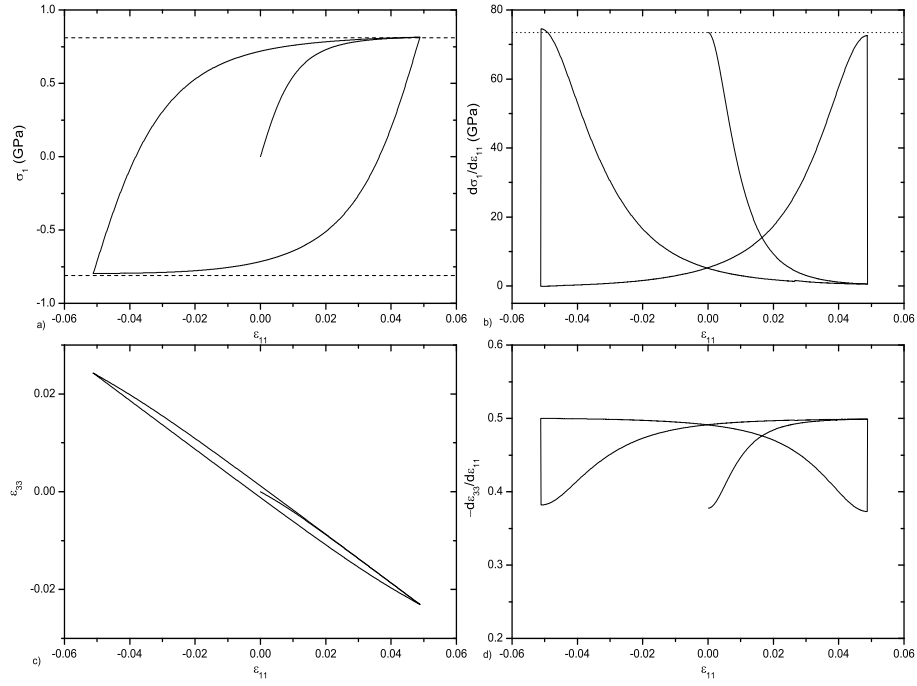


Figure 4.6: Simulation of an uniaxial tension compression test. Representation of a) the stress σ_{11} , b) the slope $d\sigma_{11}/d\epsilon_{11}$, c) the strain in the transverse direction ϵ_{33} and d) the slope $-d\epsilon_{33}/d\epsilon_{11}$ versus the strain ϵ_{11} .

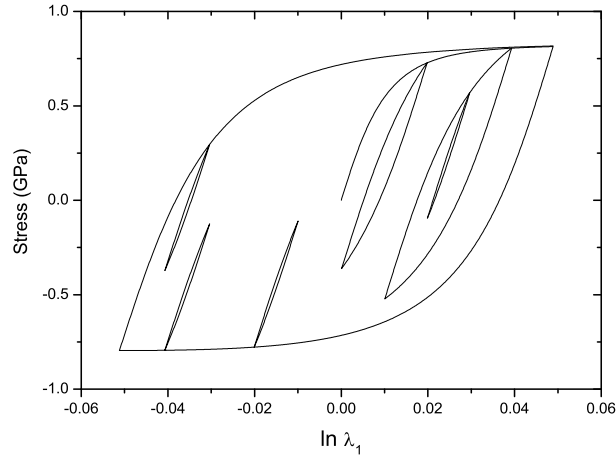


Figure 4.7: Simulation of an uniaxial cyclic tensile test with subloops of load.

The relations between these parameters are the following:

$$\begin{aligned}
 \nu &= \frac{3K - E}{6K} \\
 E_b &= E \frac{1}{(1 - \nu)} \quad \text{and} \quad \nu_b = \frac{2\nu}{1 - \nu} \\
 G &= \frac{6KE}{9K - E}
 \end{aligned} \tag{4.16}$$

These values are calculated for the first point of each test, and the results are summarized in table 4.3 and compared to the values observed in figures 4.6 d), 4.8 b), 4.8 d) and 4.9 b) respectively.

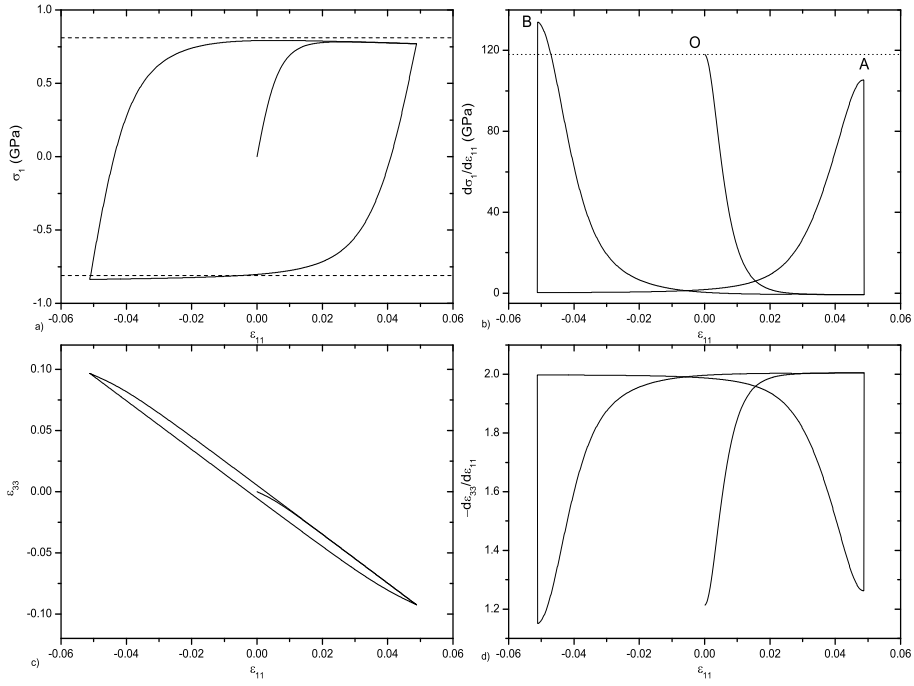


Figure 4.8: Simulation of an equibiaxial tension compression test. Representation of a) the stress σ_{11} , b) the slope $d\sigma_{11}/d\epsilon_{11}$, c) the strain in the transverse direction ϵ_{33} and d) the slope $-d\epsilon_{33}/d\epsilon_{11}$ versus the strain ϵ_{11} .

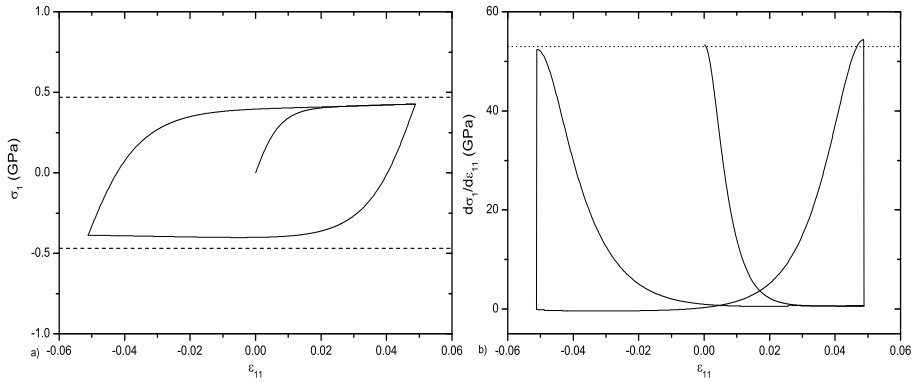


Figure 4.9: Simulation of a planar tension compression test. Representation of a) the stress σ_{11} and b) the slope $d\sigma_{11}/d\epsilon_{11}$ versus the strain ϵ_{11} .

	Calculation	Measure
ν	0.38	0.38
E_b (GPa)	118	118
ν_b	1.23	1.21
G (GPa)	53	53

Table 4.3: Comparison between the values of the parameters calculated and observed used for the simulations using the elasto-plasticity model.

The values observed in the different figures (dotted lines) are observed to be equal or nearly equal to the ones calculated by means of the relations given by the classical isotropic

elasticity theory. It was observed on these three simulations that the linear elasticity rules are validated for the three different cases.

ii) Second, concerning the plasticity:

As shown in figure 4.6 a), the behavior in tension is almost perfectly plastic for strain of the order of 4% with a yield stress equal to 0.81 GPa, being represented by the dashed line. During unload, the behavior in compression is also almost perfectly plastic for strain of the order of -4% with a yield stress equal to -0.81 GPa. The similarity ratio of 2 between the first load and the unload is well observed. It is also well observed that in the plastic regions the ratio $-d\varepsilon_{33}/d\varepsilon_{11}$ is equal to 0.5 due to the fact that there is no volume change in plasticity.

The yield stresses predicted by the von Mises criterion are plotted in dashed line in figures 4.8 and 4.9 for equibiaxial and planar tension compression tests, respectively. This criterion is verified with some problems, detailed in the following. Concerning the equibiaxial tension, in the plastic regions, the ratio $-d\varepsilon_{33}/d\varepsilon_{11}$ is equal to 2, since there is no volume change in plasticity.

iii) Third, concerning the undesirable effects:

It can be observed on three stress strain curves (figures 4.6 a), 4.8 a) and 4.9 a)) that there is a weak increase or decrease of the plateau during the tension and compression, especially for the equibiaxial (figure 4.8 a)) and planar case (figure 4.9 a)). Figure 4.10 presents the monodimensional behavior in each direction presented in figure 4.4 during the simulation of the equibiaxial tension compression test in directions 1 and 3 (figure 4.8). It can be observed that the plateaus are reached for all directions and that they are perfectly horizontal. Thus, the slope observed on the stress plateau in figure 4.8 a) is not induced by the monodimensional behavior of each direction.

Moreover, the same simulations are done in these two cases but with an initial compression, and represented in figure 4.11. This undesirable effect is observed with both initial tension and compression. Therefore, it can be concluded that it is not due to the load history. It is probably due to the term $\left(\mathbf{A}_{\mathbf{n}}^{(i)} - \frac{1}{3} \mathbf{I}\right)$ in the formula 4.12 of the deviatoric stress. Moreover, the slopes are observed to be slightly different between the beginning of the simulation (O) and the end of the load (A) and unload (B), especially for the equibiaxial simulation. Further investigations have to be done about this effect.

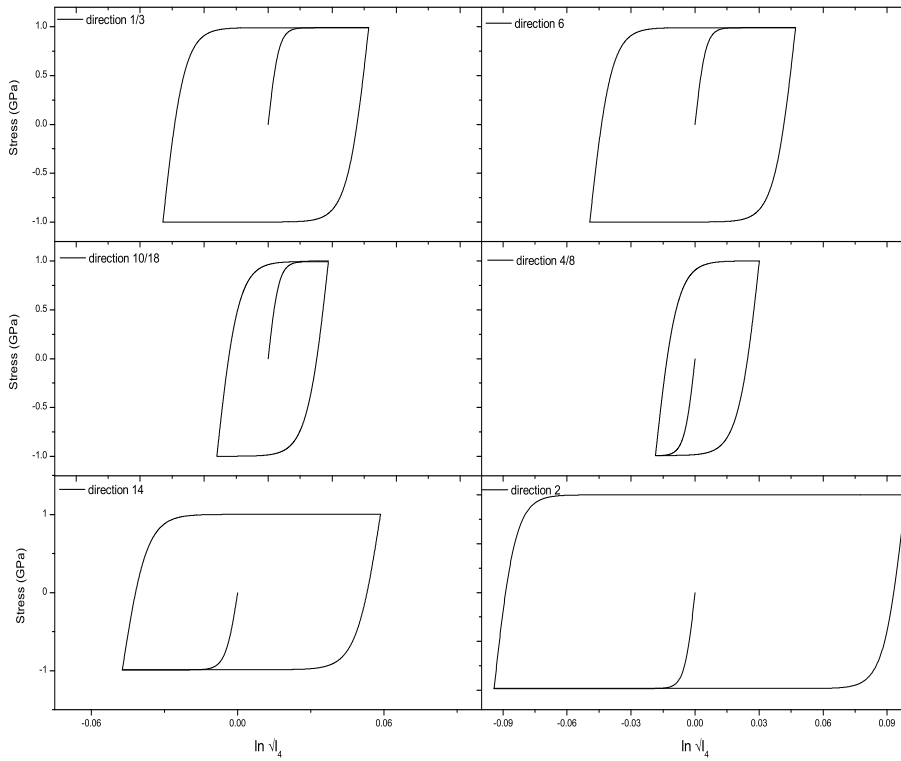


Figure 4.10: Representation of the monodimensional behavior in each direction of the eighth of the unit sphere during an equibiaxial tension compression test along the directions 1 and 3.

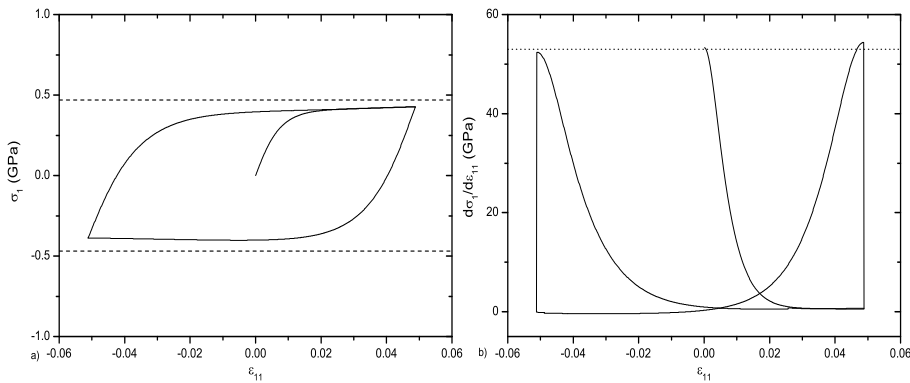


Figure 4.11: Simulation of a) an equibiaxial and b) a planar tension compression test initially loaded in compression.

4.3 Model of superelasticity

4.3.1 Deformations mechanisms

The superelastic behavior of SMAs is a combination of deformations due to the elasto-plasticity and deformations due to the phase transformation between austenite and martensite. A second contribution is added to the elasto-plastic model presented in the previous section, in order to represent the transformation mechanisms of SMAs. The mechanistic model of this model is presented in figure 4.12. The elasto-plastic part previously

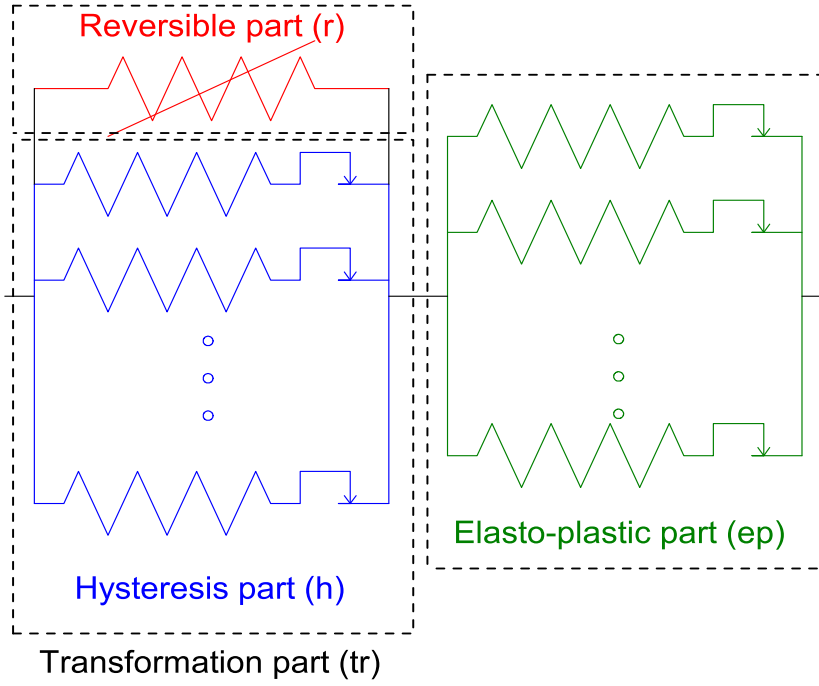


Figure 4.12: Rheological model.

presented in figure 4.1 is still present in this 1D model, and on the left was added the second part, detailed in the following. In the following, the indices ep and tr denote the elasto-plastic and transformation variables, respectively.

As seen in this figure, the transformation and elasto-plastic parts are linked in series, therefore the following equations can be written:

$$\begin{aligned}\dot{\sigma} &= \dot{\sigma}_{ep} = \dot{\sigma}_{tr} \\ \dot{\varepsilon} &= \dot{\varepsilon}_{ep} + \dot{\varepsilon}_{tr}\end{aligned}\tag{4.17}$$

4.3.2 1D modeling of the transformation contribution

As previously explained, this contribution is introduced to represent the behavior of SMAs during the phase transition.

The material is assumed to be composed of only two different phases, i.e. austenitic and martensitic (A and M). Even if a third phase can be sometimes observed (the rhombohedral phase in the NiTi), this is not taken into account in this model. The material is assumed to be austenitic at the beginning of a test. Martensitic fraction f_m is introduced, representing the volume of the material which is transformed in martensite. It is considered that the material is totally transformed when the strain reaches a limit value $\Delta\varepsilon_{tr}$. As the mechanical behavior of the NiTi was often observed to exhibit an asymmetry between tension and compression [Orgéas and Favier, 1998], the limit value $\Delta\varepsilon_{tr}$ can be different in tension and in compression. The transformation strain is so defined as:

$$\begin{aligned}\varepsilon_{tr} &= f_m \Delta\varepsilon_{tr}^t \quad \text{with } \Delta\varepsilon_{tr}^t > 0 \quad \text{if } \varepsilon_{tr} > 0 \\ \text{or } \varepsilon_{tr} &= f_m \Delta\varepsilon_{tr}^c \quad \text{with } \Delta\varepsilon_{tr}^c < 0 \quad \text{if } \varepsilon_{tr} < 0\end{aligned}\tag{4.18}$$

where the index t and c mean tension and compression respectively.

The mechanical stress σ of the transformation part is obtained by adding two contributions, a reversible σ_r and a hysteresis σ_h one:

$$\sigma_{tr} = \sigma_r + \sigma_h \quad (4.19)$$

The reversible contribution gives the same mechanical response during a load and an unload, and can be represented by a non-linear spring, as seen in figure 4.13. This part is governed by the following equation:

$$\dot{\sigma}_r = E_r \left(1 - \left(\frac{\sigma_r}{S_{0r}} \right)^c \right) \dot{\varepsilon}_{tr} \quad (4.20)$$

where E_r is the initial slope, similar to a Young modulus, S_{0r} the threshold stress of the function, c a constant allowing to have a transition more or less smooth between the first slope and the plateau. Written in direct formulation, and taking $c = 2$, the equation for the reversible stress is:

$$\sigma_r = S_{0r} \tanh \left(\frac{E_r \varepsilon_{tr}}{S_{0r}} \right) \quad \text{with} \quad \varepsilon_{tr} = f_m \Delta \varepsilon_{tr} \quad (4.21)$$

In order to represent the asymmetry between tension and compression, different values for S_{0r} can be taken in tension and compression, there are so two different parameters S_{0r}^t and S_{0r}^c , as presented in Figure 4.13.

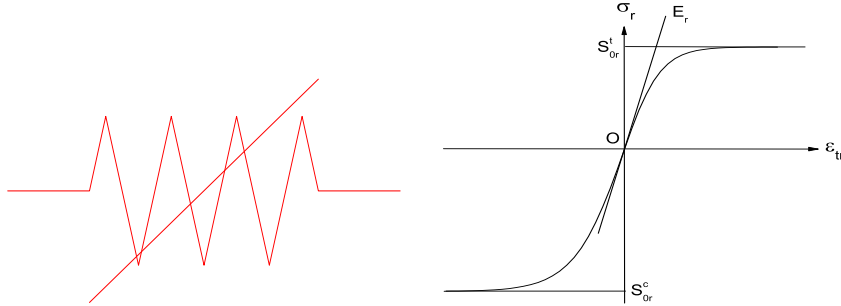


Figure 4.13: Rheological model and mechanical response of the reversible contribution of the transformation part.

The hysteresis contribution of the transformation part is almost similar to the elasto-plastic model previously presented. The difference is that the similarity ratio ω is equal to 1. Thus, it is governed by the following equation:

$$\dot{\sigma}_h = E_h \left(1 - \left(\frac{\sigma_h - \sigma_h^{inv}}{S_{0h}} \right)^c \right) \dot{\varepsilon}_{tr} \quad (4.22)$$

where E_h is an initial slope, S_{0h} the threshold stress of the function, I the number of inversion points still memorized, σ_h^{inv} the stress value of the last inversion point recorded.

Figure 4.14 presents the behavior of this part.

4.3.3 Modeling of the plasticity of SMAs

Deformations due to transformations will be large compared to elasto-plastic deformations as long as $S_{0ep} > S_{0tr} = S_{0r} + S_{0h}$.

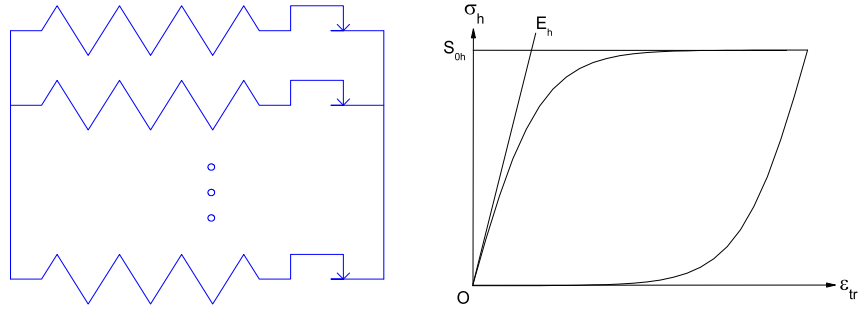


Figure 4.14: Hysteretic contribution of the transformation part with $\omega = 1$.

Like the martensite fraction f_m cannot be superior to one, a penalization function is introduced in order to reduce and stop the transformation part when f_m approaches a value equal to 1. The following form is chosen:

$$\sigma_{pen} = S_{0ep} c_1 \exp(f_m/c_2) \quad \text{and} \quad \sigma_{tr} = \sigma_h + \sigma_r + \sigma_{pen} \quad (4.23)$$

where c_1 and c_2 are two parameters (taken in the following equal to 10^{-6} and 0.07 respectively) in order to ensure that this contribution is superior to S_{0ep} for a martensite fraction equal to 1. This function is shown in figure 4.15, with $S_{0ep} = 1$ and it is observed that its contribution is negligible while the martensite fraction is weak, *i.e.* inferior to almost 0.7. Then, the response of this function is no more zero and is more and more important until the martensite fraction reaches 1. The threshold stress S_{0ep} is reached for a value of the martensite fraction just inferior to 1.

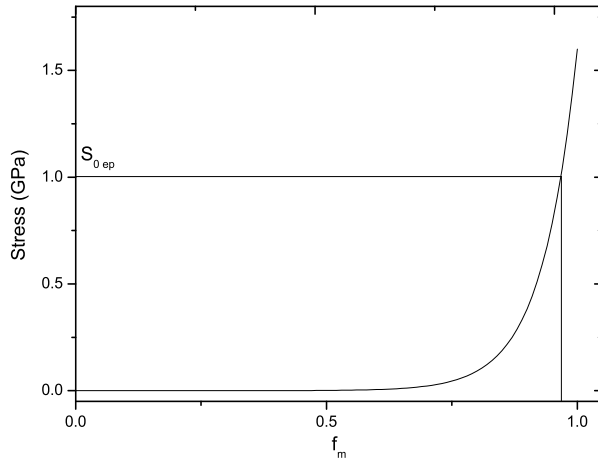


Figure 4.15: Limitation of the evolution of the martensite fraction.

4.3.4 Monodimensional simulations

The 1D mechanistic model of figure 4.12 can be loaded with controlled force or controlled deformation. If a force is imposed, the kinematic of transformation and elasto-plastic parts is simply deduced by the relation between force and strain in each point. Once the two parts of the strain are calculated, the total strain is simply deduced by adding them. If a strain is imposed, its repartition into a transformation and an elasto-plastic part is

estimated, and the two corresponding stresses are calculated. If these two stresses are not equal (or nearly equal, *i.e.* a difference inferior to 10^{-10} for numerical reasons), a Newton-Raphson algorithm is used to calculate again the repartition of the strain. This process is used until equality between the two stresses is obtained. The resolution algorithm in this case (strain imposed) is presented in figure 4.16.

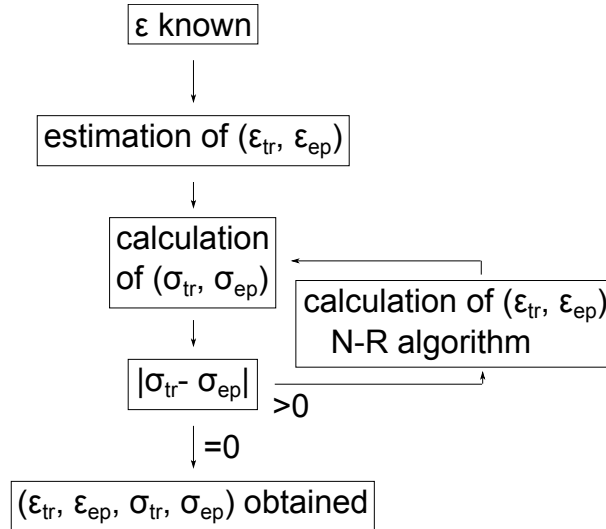


Figure 4.16: Resolution algorithm in each direction to determine the strain repartition and the stress.

In order to illustrate the capacities of the 1D model, three simulations are presented in figure 4.17, whose parameters are given in table 4.4.

E_{ep} (GPa)	S_{0ep} (GPa)	E_h (GPa)	S_{0h} (GPa)	ω
500	1	150	0.2	1
E_r (GPa)	S_{0rt} (GPa)	S_{0rc} (GPa)	$\Delta\varepsilon_{tr}^t$	$\Delta\varepsilon_{tr}^c$
150	0.2	0.36	0.08	0.05

Table 4.4: Values of the parameters used for the 1D simulations presented in figure 4.17.

Figure 4.17 a) shows a simulation with different values for S_{0r} in tension and in compression, and it is observed that the total response of the model presents an asymmetry between tension and compression. A load unload simulation with a major loop and subloops is presented in figure 4.17 b). The subloops are well represented with this model. Figure 4.17 c) shows the simulation of a load until the plasticity. The transformation plateau is well observed, followed by a second elastic part, and then finally a second plateau is observed, corresponding to plasticity of the material.

4.3.5 3D modeling of the superelasticity of SMAs

The 3D extension of this 1D model is performed by the same way than for elasto-plasticity, the deformation previously presented ($\bar{\varepsilon}^{(i)} = \ln(\bar{\lambda}^{(i)}) = \ln\sqrt{\bar{I}_4^{(i)}}$) being the sum of the elasto-plastic and transformation strains in each direction.

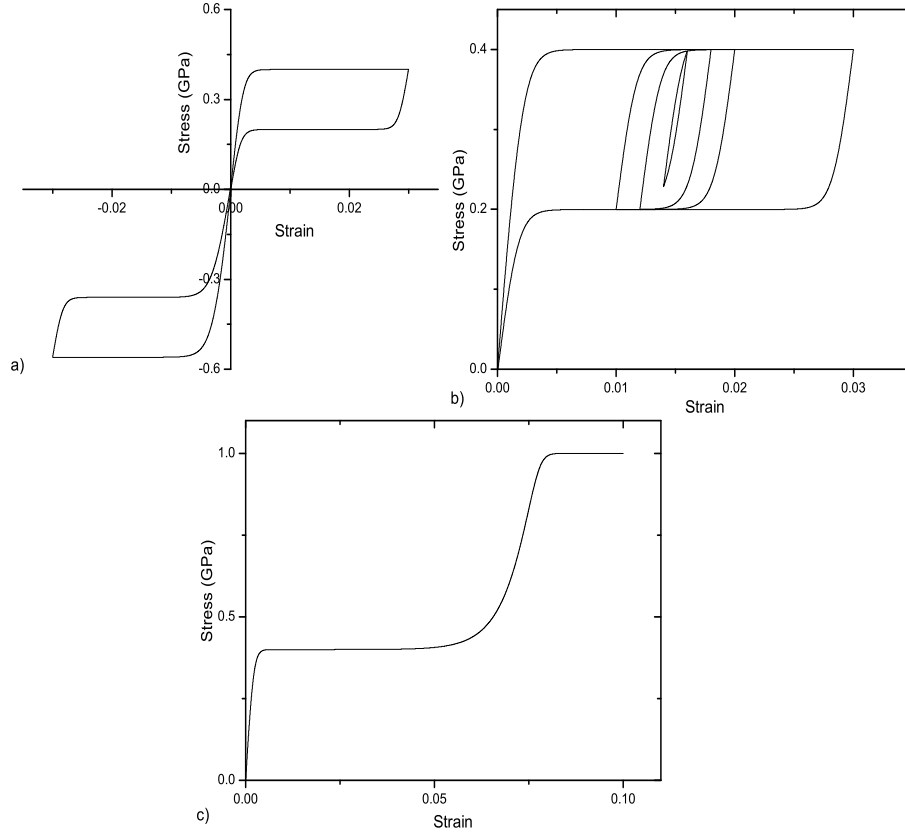


Figure 4.17: Simulations of a) asymmetry of the tension compression response, b) load unload with subloops of loading and c) a load reaching the plasticity.

The monodimensional model previously presented has to be adapted to represent the 3D superelastic behavior of SMAs, especially for the plasticity. The plasticity function presented in the monodimensional description of the model depended on the martensitic fraction. However, considering the 3D model, it is the total martensitic fraction which cannot be superior to 1. Thus, the total martensitic fraction F_m is calculated by summing all the direction contributions:

$$F_m = \sum_{i=1}^n f_m^{(i)} \quad (4.24)$$

The equation used for the evolution of the stress due to the total martensitic fraction is so written as follows:

$$\sigma_{pen} = S_{0ep} c_1 \exp(F_m/c_2) \quad (4.25)$$

This penalization function is the same for all directions. Hence, it comes that:

$$\sigma_{tr}^{(i)} = \sigma_{pen} + \sigma_r^{(i)} + \sigma_h^{(i)} = \sigma_{ep}^{(i)} \quad (4.26)$$

The resolution algorithm to find the repartition of the strain in each direction in the case of an imposed strain (presented in figure 4.16) is also modified since the local stress in each direction depends on the total martensitic fraction, and so on all the local strains. The strains are imposed in each direction, and the repartition of these strains is estimated for the 42 directions. The total martensitic fraction is then calculated, by means of the transformation strains. Then, the local stresses are calculated, and the test of equality

is done in each direction like previously. If this equality is not ensured, new values of the two contributions of the 42 strains are calculated by means of the Newton-Raphson algorithm, generalized for equations systems. The new resolution algorithm in this case (strain imposed) is presented in figure 4.18.

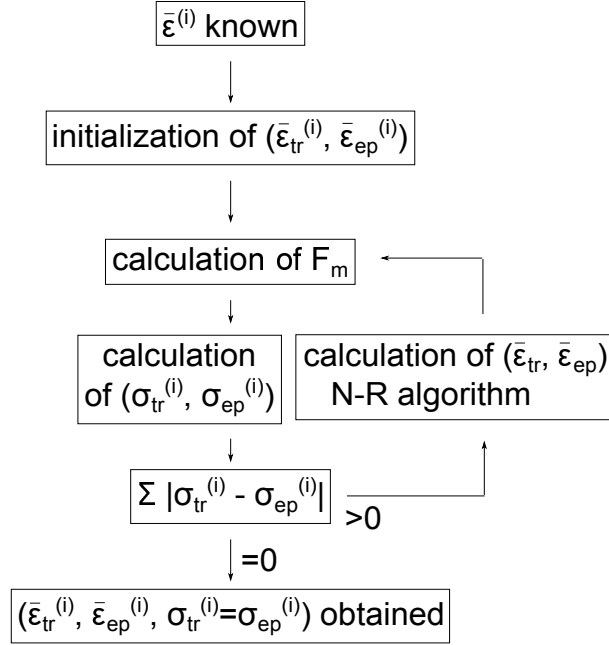


Figure 4.18: Resolution algorithm to determine the strains repartition and the stresses in each direction.

4.4 Simulation of an experimental result of the literature

An experimental test of the literature is presented and then simulated in this section.

A pure shear test performed on a NiTi specimen is presented [Orgéas, 1997]. This test is composed of one symmetric load-unload major loop, with subloops inside the major loop. Figure 4.19 presents a) the results of the experimental pure shear test, b) the result of the planar tension simulation of it, and c) the evolution of the martensitic fraction during the simulation. The parameters used to fit this test are given in table 4.5.

E_{ep} (GPa)	S_{0ep} (GPa)	E_h (GPa)	S_{0h} (GPa)	
150	1	150	0.36	
E_r (GPa)	S_{0rt} (GPa)	S_{0rc} (GPa)	$\Delta\epsilon_{tr}^t$	$\Delta\epsilon_{tr}^c$
50	0.34	0.34	1	1

Table 4.5: Values of the material parameters fitted on experimental pure shear data.

The mechanical response of the material during such a test is well predicted by the model, as the experimental and simulation curves are very similar. The hysteresis subloops are also well represented by the model. The martensitic ratio is observed to reach a maximal value of 0.5, meaning that a half of the material is transformed from austenite to martensite when the strain is maximal during this test. Moreover, the martensitic ratio

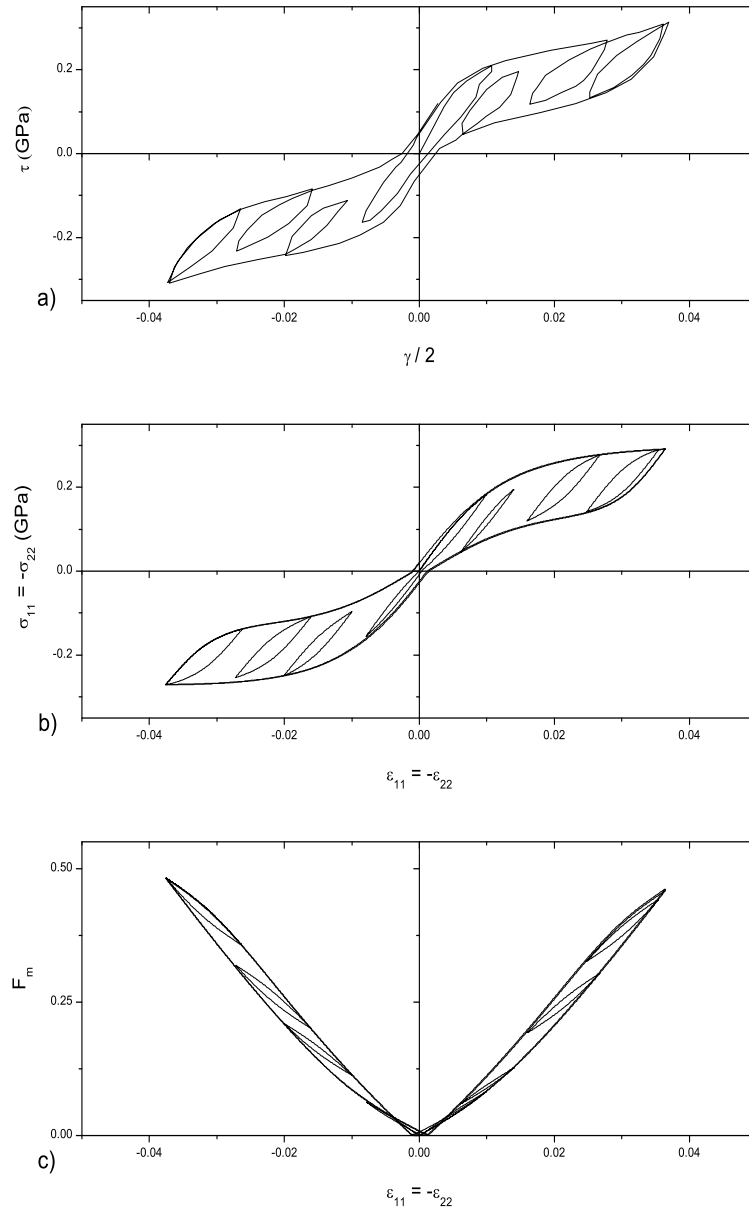


Figure 4.19: Results of a) an experimental pure shear test [Orgéas, 1997], b) the simulation of this test with planar tension conditions and c) the evolution of the martensitic fraction during the simulation.

immediately increases or decreases when an inversion or load occurs, well representing what happens in NiTi shape memory alloys. These results are qualitatively in agreement with experimental results. However, a lot of developments are still necessary, concerning both experiments and model.

4.5 Conclusions

A model for SMAs was proposed in this chapter. This is a model of elasto-plasticity, whose originality is to use a formalism which is classical to model elastomers but not for metallic materials. This model was then extended for the superelasticity of SMAs, so

including the mechanical response of the phase transition. Several typical phenomena of the mechanical behavior of SMAs were taken into account in the monodimensional proposed, as the mechanical hysteresis, the plasticity and the asymmetry between tension and compression. A test of the literature was simulated with this model, and its result was well predicted using the proposed model, showing its good performance. However, works is still to do to obtain a model taking into account more phenomena and some undesirable effects were observed and have to be investigated.



Conclusion and perspectives

This manuscript presents the first investigations on an architected NiTi/silicone composite. The first part of the study (chapter 1) is devoted to the fabrication of an architected NiTi silicone rubber composite. Several solutions for the improvement of the adhesion between NiTi shape memory alloy and silicone rubbers were tested. In the present study, plasma treatment and adhesion promoter were used to the mechanical properties of the interface between these two materials. The mechanical resistance of the interface has been evaluated by means of pull out tests using a self-developed device. Results have shown that the use of both primer and plasma treatment gives an enhancement of the adhesion between NiTi wires and silicone rubber. In order to focus on biomedical applications, only plasma treatment was then considered. Investigations were carried out to study the effects of treatment parameters on the mechanical resistance of the interface. Results showed that the argon gave the best improvement of the adhesion at the interface between NiTi and silicone rubber compared to oxygen and air. This treatment was used to elaborate an architected NiTi silicone rubber composite. For this purpose, a knitted tube of NiTi wires was embedded. This composite was mechanically characterized by means of bulge tests. Variations in the composite length were found to be low compared to the radial extension, showing that it is well adapted to fabricate artificial vessels. Moreover, the mechanical behavior of such a composite can be easily modified, by changing the mesh knitting or use the shape memory effect, non exhaustively. Also, the silicone rubber ensures both the impermeability of the composite and the isolation of the NiTi from the external environment. These results are very promising to address biomedical applications.

The mechanical behavior of NiTi strongly depends on temperature. Moreover, the mechanical behavior of silicone rubber is also influenced by the temperature. For this reason, mechanical tests were performed at different temperatures on two silicone rubbers (filled and unfilled). Significant changes in the mechanical response of the two silicones were observed when the temperature is close to the crystallization or the melting temperature, especially their stiffness. Far from these temperatures, changes in the mechanical behavior of the silicone rubbers were also observed with changes of temperature, as well as changes in the stress softening and in the mechanical hysteresis.

The second part of this PhD Thesis (chapters 3 and 4) deals with the prediction of the mechanical behavior of silicone rubber and of NiTi. As the architected composite is expected to undergo cyclic mechanical loadings, the mechanical hysteresis in the response of both materials has been modeled. For silicone rubbers, a model has been proposed to account for the rate-independent mechanical hysteresis. A directional method was used in order to model both isotropic and anisotropic materials. A mechanistic model with associations of springs and sliders was proposed, and the inversion points method was used to model hysteresis loops. The interest of the proposed model is that it can be used with any existing hyperelastic model. A classical hyperelastic model was employed to simulate uniaxial and planar tensile tests performed on a filled silicone rubber. The mechanical hysteresis of the material was satisfactorily predicted by the proposed model. The model was then implemented in the finite elements software Abaqus by means of a UMAT subroutine. Good predictions of the mechanical hysteresis of rubberlike materials and convergence were obtained.

A model was also developed for NiTi SMAs. An elasto-plastic model was proposed and extended to the superelastic behavior of shape memory alloys. The same formalism as for the model developed for rubberlike materials was used. A monodimensional model has been developed, taking into account several phenomena observed in NiTi: tension compression asymmetry, residual strain or mechanical hysteresis, non exhaustively. This monodimensional model was shown to predict satisfactorily both elasto-plastic and superelastic behaviors. The model was then extended in three directions by means of the directional approach to simulate a pure shear test of the literature.

This PhD Thesis is an exploratory study and numerous perspectives can be mentioned. Additional mechanical and thermo-mechanical tests have to be carried out in order to fully characterize the behavior of NiTi silicone rubber composite. The temperature influence on silicone rubbers could be modeled by means of the results of chapter 2. Also, an association of the model proposed in chapter 3 with models recently developed in the literature taking into account of several phenomena, especially the rate-dependent hysteresis, could be investigated. Concerning the modeling of SMAs, their thermomechanical behavior has to be investigated. In order to model the behavior of a NiTi silicone rubber composite, these two models could be associated or a model proposing an equivalent behavior could be proposed.

APPENDIX

A

Tensile tests performed on NiTi silicone rubber composite

Once the architected NiTi silicone rubber composite presented in chapter 1 was elaborated, its mechanical properties were first characterized by means of classical cyclic tensile tests. The tests were performed using a Gabo Eplexor 500N machine. Several increasing loading cycles were carried out on the specimen in large deformations. Figure A.1 presents 3 pictures of the tube, at the beginning of the test (figure A.1 a)), during the last loading, at a strain nearly equal to 40% (figure A.1 b)), and at the end of the test (figure A.1 c)). During the test, the tubular structure diameter strongly decreased when a great extension

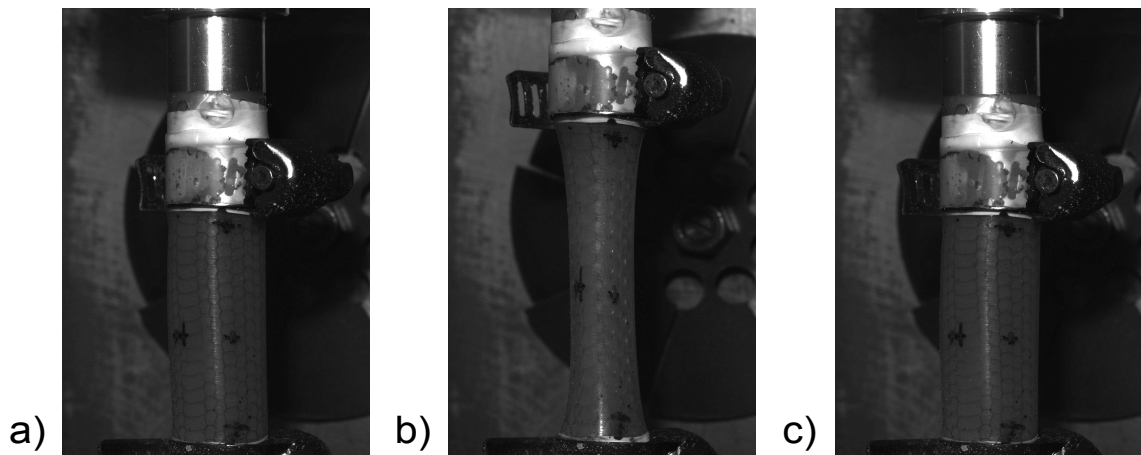


Figure A.1: Pictures of the tube a) at the beginning of the tensile test, b) during the last loading and c) and at the end of the tensile test.

of the length occurred (cf figure A.1 b)). Figure A.2 shows the results of this tensile test.

It can be observed that even if large deformations were reached, no plasticity was observed, whereas the NiTi was supposed to reach plasticity for deformation inferior to 20%. This larger reversible behavior can be explained by structural effects. Moreover, mechanical hysteresis was observed for each deformation cycle, and a few softening between the first and second loads (for equal strain) for each cycle. To analyze the accommodation of the mechanical behavior of the architected composite, the same test is performed

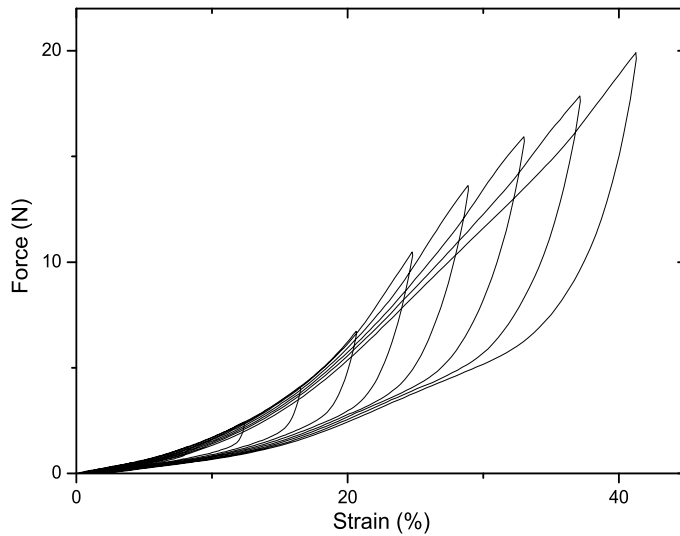


Figure A.2: Results of a tensile test with increasing loading cycles.

once again on the same specimen. The results of this test are presented in figure A.3, and compared to the results of the previous test. The same type of mechanical response as

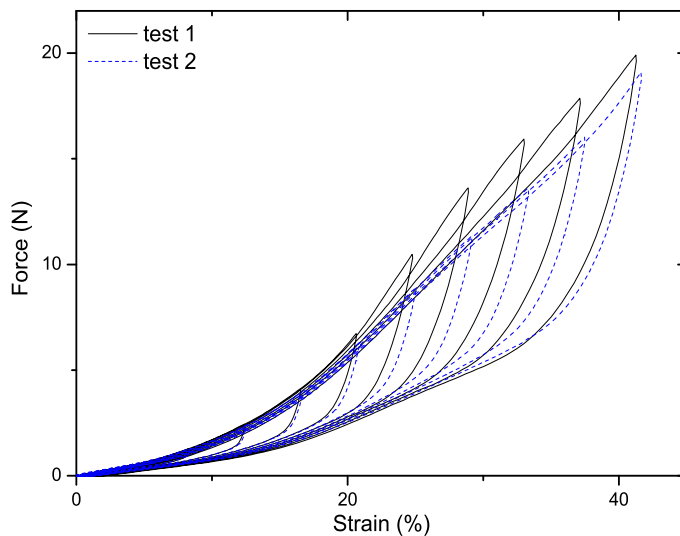


Figure A.3: Results of successive tensile tests with increasing loading cycles.

previously is observed, *i.e.* large deformations without plasticity and mechanical hysteresis. Nevertheless, the mechanical response is softened compared to the first test and nearly corresponds to the last cycle of the first test. Moreover, the cyclic mechanical response is nearly equal for this test. Hence, it can be concluded that such a composite presents a mechanical behavior different between the first and the following loadings, meaning that an accommodation occurs after the first cycle. This phenomenon could be due to different effects: stress softening of NiTi and/or silicone rubber, structural effects, interface accommodation... Further investigations have to be carried out to determine it.

As the mechanical behavior of NiTi is well known to depend on react with temperature, this mechanical test is performed a third time on the same specimen, but at a

temperature equal to 37°C , whereas the first tests were performed at room temperature, *i.e.* equal to 20°C . Figure A.4 shows the results of this test, and one can observe that the mechanical behavior of the composite is still accommodated but its stiffness is higher at 37°C than at 20°C . These observations can be explained by the temperature dependence of the mechanical behavior of NiTi, *i.e.* the increase of its stiffness with the increase of temperature.

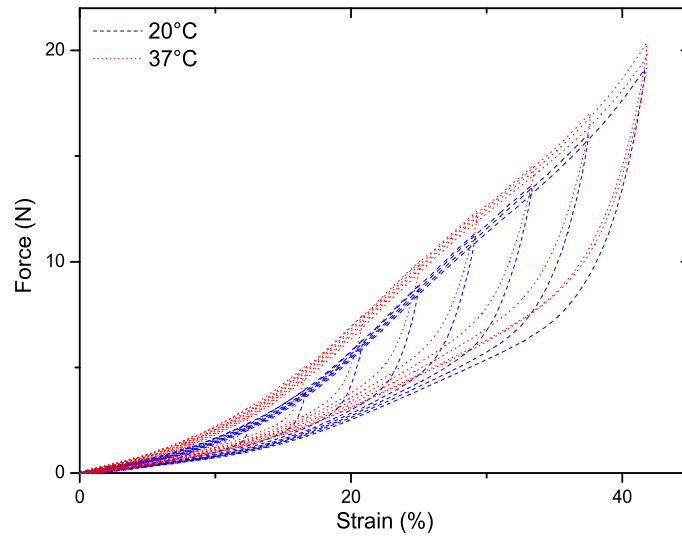


Figure A.4: Accommodated behavior of the NiTi silicone rubber composite, at different temperatures.

Finally, these tensile tests highlight that the composite presents a reversible mechanical behavior, being accommodated after a few cycles. As a conclusion, this mechanical behavior depends on the temperature, and also exhibits large mechanical hysteresis.



Bibliography

- Ambacher, H., Straub, M., Kilian, N., and Wolff, S. (1991). Reinforcement in filler loaded rubbers. *Kaut. Gummi Kunstst.*, **44**, 1111–1118.
- Amin, A. F. M. S., Lion, A., Sekita, S., and Okui, Y. (2006). Nonlinear dependence of viscosity in modeling the rate-dependent response of natural and high damping rubbers in compression and shear: experimental identification and numerical verification. *Int. J. Plast.*, **22**, 1610–1657.
- Bansiddhi, A., Sargeant, T., Stupp, S., and Dunand, D. (2008). Porous NiTi for bone implants. *Acta Biomater.*, **4**, 773–782.
- Bažant, P. and Oh, B. (1986). Efficient numerical integration on the surface of a sphere. *ZAMM-J. Appl. Math. Mec.*, **66**(1), 37–49.
- Beatty, M. F. and Krishnaswamy, S. (2000). A theory of stress-softening in incompressible isotropic materials. *J. Mech. Phys. Solids*, **48**, 1931–1965.
- Berger-Gorbet, M., Broxup, B., Rivard, C., and Yahia, L. (1996). Biocompatibility testing of NiTi screws using immunohistochemistry on sections containing metallic implants. *J. Biomed. Mater. Res.*, **32**, 243–248.
- Bergstrom, J. S. and Boyce, M. C. (1998). Constitutive modeling of the large strain time dependant behavior of elastomers. *J. Mech. Phys. Solids*, **46**(5), 931–954.
- Biderman, V. L. (1958). Calculations of rubber parts (in russian). *Rascheti na Prochnost*, page 40.
- Brailovski, V., Prokoshkin, S., Gauthier, M., Inaekyan, K., Dubinskiy, S., Petrzhik, M., and Filonov, M. (2011). Bulk and porous metastable beta Ti-Nb-Zr(Ta) alloys for biomedical applications. *Mat. Sci. Eng. C*, **31**(3), 643–657.
- Brechet, Y. and Embury, J. (2013). Architected material: expanding materials space. *Sci Mat.*, **68**, 1–3.

- Chagnon, G., Verron, E., Gornet, L., Marckmann, G., and Charrier, P. (2004). On the relevance of continuum damage mechanics as applied to the Mullins effect: theory, experiments and numerical implementation. *J. Mech. Phys. Solids*, **52**, 1627–1650.
- Chang, P. P., Hansen, N. A., Phoenix, R. D., and Schneid, T. R. (2009). The effects of primers and surface bonding characteristics on the adhesion of polyurethane to two commonly used silicone elastomers. *J. Prosthodont.*, **18**, 23–31.
- Chean, V., Robin, E., Abdi, R. E., Sangleboeuf, J.-C., and Houizot, P. (2011). Use of the mark-tracking method for optical fiber characterization. *Opt. Laser Technol.*, **43**, 1172 – 1178.
- Chemisky (2009). *Modélisation du comportement macroscopique des alliages à mémoire de forme - Application aux matériaux composites*. Ph.D. thesis, Université Paul Verlaine de Metz.
- D’Ambrosio, P., De Tommasi, D., Ferri, D., and Puglisi, G. (2008). A phenomenological model for healing and hysteresis in rubber-like materials. *Int. J. Eng. Sci.*, **46**, 293–305.
- de Araùjo, C. J., Rodrigues, L. F. A., Coutinho Neto, J. F., and Reis, R. P. B. (2008). Fabrication and static characterization of carbon-fiber-reinforced polymers with embedded NiTi shape memory wire actuators. *Smart Mater. Struct.*, **17**, 065004.
- Delobelle, V., Delobelle, P., Liu, Y., Favier, D., and Louche, H. (2013). Resistance welding of NiTi shape memory alloy tubes. *J. Mater. Process. Tech.*, **213**, 1139–1145.
- DeSimone, A., Marigo, J. J., and Teresi, L. (2001). A damage mechanics approach to stress softening and its application to rubber. *Eur. J. Mech. A/Solids*, **20**, 873–892.
- Diani, J., Brieu, M., and Vacherand, J. (2006a). A damage directional constitutive model for Mullins effect with permanent set and induced anisotropy. *Eur. J. Mech.-A/Solids*, **25**(3), 483–496.
- Diani, J., Brieu, M., and Gilormini, P. (2006b). Observation and modeling of the anisotropic visco-hyperelastic behavior of a rubberlike material. *Int. J. Solids Struct.*, **43**, 3044–3056.
- Diani, J., Fayolle, B., and Gilormini, P. (2009). A review on the Mullins effect. *Eur. Polym. J.*, **45**, 601–612.
- Dorfmann, A. and Ogden, R. (2003). A pseudo-elastic model for loading, partial unloading and reloading of particle-reinforced rubber. *Int. J. Solids Struct.*, **40**(11), 2699–2714.
- Dorfmann, A. and Ogden, R. (2004). A constitutive model for the Mullins effect with permanent set in particle-reinforced rubber. *Int. J. Solids Struct.*, **41**(7), 1855–1878.
- Duerig, T., Pelton, A., and Stöckel, D. (1999). An overview of nitinol medical applications. *Mater. Sci. Eng A*, **273**, 149–160.
- Dunlop, J. and Fratzl, P. (2013). Multilevel architectures in natural materials. *Sci Mat.*, **68**, 8–12.

- Es-Souni, M., Es-Souni, M., and Fischer-Brandies, H. (2005). Assessing the biocompatibility of NiTi shape memory alloys used for medical applications. *Anal. Bioanal. Chem.*, **381**, 557–567.
- Everaert, E., Van de Belt-Gritter, B., Van der Mei, H., Busscher, H., Verkerke, G., and Dijk, F. (1998). In vitro and in vivo microbial adhesion and growth on argon plasma-treated silicone rubber voice prostheses. *J. Mater. Sci.-Mater. M.*, **9**, 147–157.
- Favier, D. (1988). *Contribution à l'étude théorique de l'élastohystérésis à température variable, application aux propriétés de mémoire de forme*. Habilitation thesis, University of Grenoble.
- Favier, D. and Guélin, P. (1985). A discrete memory constitutive scheme for mild steel type material theory and experiment. *Arch. Mech.*, **37**, 201–19.
- Favier, D. and Liu, Y. (2000). Restoration by rapid overheating of thermally stabilised martensite of NiTi shape memory alloys. *J. Alloy. Compd.*, **297**, 114–121.
- Favier, D., Guélin, P., and Cammarano, R. (1992). Application of a phenomenological elastohysteretic theory to the modeling of magnetization. In *Seventh International Symposium on Magnetic Anisotropy and Coercivity in Rare-Earth Transition Metal Alloys*, pages 137–150, Canberra (Australia).
- Favier, D., Rio, G., and Manach, P. Y. (1997). Grandes déformations et loi d'élastohystérésis appliquées au calcul par éléments finis d'élastomères. In *Génie Mécanique des caoutchoucs et des élastomères thermoplastiques*.
- Favier, D., Liu, Y., Orgéas, L., Sandel, A., Debove, L., and Comte-Gaz, P. (2006). Influence of thermomechanical processing on the superelastic properties of a Ni-rich nitinol shape memory alloy. *Mater. Sci. Eng A*, **429**, 130–136.
- Federico, S., Grillo, A., Imatani, S., Giaquinta, G., and Herzog, W. (2008). An energetic approach to the analysis of anisotropic hyperelastic materials. *Int. J. Eng. Sci.*, **46**, 164–181.
- Fletcher, W. P. and Gent, A. N. (1953). Non-linearity in the dynamic properties of vulcanised rubber compounds. *Trans. Instn. Rubber Industr.*, **29**, 266–280.
- Flory, P. J. (1947). Thermodynamics of crystallisation in high polymers. 1. Crystallization induced by stretching. *J. Chem. Phys.*, **15**(6), 397–408.
- Garner, L. J., Wilson, L. N., Lagoudas, D. C., and Rediniotis, O. K. (2000). Development of a shape memory alloy actuated biomimetic vehicle. *Smart Mater. Struct.*, **9**, 673–683.
- Golaz, B., Michaud, V., and Manson, J.-A. (2011). Adhesion of thermoplastic polyurethane elastomer to galvanized steel. *Int. J. Adhes. Adhes.*, **31**, 805 – 815.
- Guélin (1980). Remarque sur l'hystérésis mécanique: les bases dun schéma thermo-mécanique à structure héréditaire. *Journal de mécanique*, **19**, 217–247.

- Hamming, L., Fan, X., Messersmith, P., and Brinson, L. (2008). Mimicking mussel adhesion to improve interfacial properties in composites. *Compos. Sci. Technol.*, **68**, 2042 – 2048.
- Hauser, J., Zietlow, J., Köller, M., Esenwein, S. A., Halfmann, H., Awakowicz, P., and Steinau, H. U. (2009). Enhanced cell adhesion to silicone implant material through plasma surface modification. *J. Mater. Sci.: Mater. Med.*, **20**, 2541–2548.
- Heller, L., Vokoun, D., Šittner, P., and Finckh, H. (2012). 3D flexible NiTi-braided elastomer composites for smart structure applications. *Smart Mater. Struct.*, **21**, 045016.
- Holzapfel, G. A. and Gasser, T. C. (2001). A viscoelastic model for fiber-reinforced composites at finite strains: continuum basis, computational aspects and applications. *Comput. Methods Appl. Mech. Engrg*, **190**, 4379–4403.
- Hou, S.-S., Chung, Y.-P., Chan, C.-K., and Kuo, P.-L. (1999). Function and performance of silicone copolymer. Part IV. Curing behavior and characterization of epoxysiloxane copolymers blended with diglycidyl ether of bisphenol-A. *Polymer*, **41**, 3263–3272.
- Itskov, M., Haberstroh, E., Ehret, A. E., and Vohringer, M. C. (2006). Experimental observation of the deformation induced anisotropy of the Mullins effect in rubber. *KGK-Kautschuk Gummi Kunststoffe*, **59**(3), 93–96.
- Jani, J. M., Leary, M., Subic, A., and Gibson, M. A. (2014). A review of shape memory alloy research, applications and opportunities. *Mater. Design*, **56**, 1078–1113.
- Jonnalagadda, K., Kline, G., and Sottos, N. (1997). Local displacements and load transfer in shape memory alloy composites. *Exp. Mech.*, **37**, 78–86.
- Ju, X. and Dong, H. (2006). Plasma surface modification of NiTi shape memory alloy. *Surf. Coat. Technol.*, **201**, 1542 – 1547.
- Kaliske, M. (2000). A formulation of elasticity and viscoelasticity for fibre reinforced material at small and finite strains. *Comput. Methods Appl. Mech. Engrg*, **185**, 225–243.
- Kaliske, M. and Rothert, H. (1998). Constitutive approach to rate independent properties of filled elastomers. *Int. J. Solids Struct.*, **35**(17), 2057–2071.
- Khalil-Allafi, J., Amin-Ahmadi, B., and Zare, M. (2010). Biocompatibility and corrosion behavior of the shape memory NiTi alloy in the physiological environments simulated with body fluids for medical applications. *Mat. Sci. Eng. C*, **30**, 1112–1117.
- Khandelwal, A. and Vidyashankar, B. (2009). Models for Shape Memory Alloy Behavior: An overview of modeling approaches. *Int. J. Str. Changes Solids*, **1**(1), 111–148.
- Korochkina, T. V., Jewell, E. H., Claypole, T. C., and Gethin, D. T. (2008). Experimental and numerical investigation into nonlinear deformation of silicone rubber pads during ink transfer process. *Polym. Test.*, **27**, 778–791.

- Lau, K., Tam, W., Meng, W., and Zhou, L. (2002). Morphological study on twisted NiTi wires for smart composite systems. *Mater. Lett.*, **57**, 364–368.
- Laurent, H., Vandenbroucke, A., Couedo, S., and Rio, G. (2008). An hyper-visco-hysteretic model for elastomeric behaviour under low and high temperatures: Experimental and numerical investigations. In *Constitutive models for rubber V*.
- Linder, C., Tkachuk, M., and Miehe, C. (2011). A micromechanically motivated diffusion-based transient network model and its incorporation into finite rubber viscoelasticity. *J. Mech. Phys. Solids*, **59**, 2134–2156.
- Lion, A. (1996). A constitutive model for carbon black filled rubber: experimental investigations and mathematical representation. *Continuum Mech. Therm.*, **8**(3), 153–169.
- Lion, A. (1997). A physically based method to represent the thermo-mechanical behavior of elastomers. *Acta Mech.*, **123**, 1–25.
- Lorenz, H. and Klüppel, M. (2012). Microstructure-based modelling of arbitrary deformation histories of filler-reinforced elastomers. *J. Mech. Phys. Solids*, **60**, 1842–1861.
- Machado, G., Chagnon, G., and Favier, D. (2010). Analysis of the isotropic models of the Mullins effect based on filled silicone rubber experimental results. *Mech. Mater.*, **42**, 841–851.
- Machado, G., Chagnon, G., and Favier, D. (2012). Induced anisotropy by the Mullins effect in filled silicone rubber. *Mech. Mater.*, **50**, 70–80.
- Machado, G., Louche, H., Do Than, D., Favier, D., and Liu, Y. (2013). Experimental characterization and modeling of the mechanical behavior of architected tube-based NiTi materials. In *The International Conference on Shape Memory and Superelastic Technologies*.
- Machado, G., Chagnon, G., and Favier, D. (2014). Theory and identification of a constitutive model of induced anisotropy by the Mullins effect. *J. Mech. Phys. Solids*, **63**, 29–39.
- Marckmann, G. and Verron, E. (2006). Comparison of hyperelastic models for rubber-like materials. *Rubber Chem. Technol.*, **79**, 835–858.
- Masing, G. (1926). Self-stretching and hardening for brass. In *Proceedings of the 2nd International Congress for Applied Mechanics*.
- Matsuzaki, Y. and Naito, H. (2004). Macroscopic and microscopic constitutive models of shape memory alloys based on phase interaction energy function: a review. *J. Intel. Mat. Syst. Str.*, **15**(2), 141–155.
- Meunier, L., Chagnon, G., Favier, D., Orgéas, L., and Vacher, P. (2008). Mechanical experimental characterisation and numerical modelling of an unfilled silicone rubber. *Polym. Test.*, **27**, 765–777.

- Miehe, C. and Göktepe, S. (2005). A micro-macro approach to rubber-like materials. Part II: The micro-sphere model of finite rubber viscoelasticity. *J. Mech. Phys. Solids*, **53**(10), 2231–2258.
- Miehe, C. and Keck, J. (2000). Superimposed finite elastic-viscoelastic-plastoelastic stress response with damage in filled rubbery polymers. experiments, modelling and algorithmic implementation. *J. Mech. Phys. Solids*, **48**, 323–365.
- Montes, H., Chaussée, T., Papon, A., Lequeux, F., and Guy, L. (2010). Particles in model filled rubber: Dispersion and mechanical properties. *Eur. Phys. J. E*, **31**, 263–268.
- Morgan, N. (2004). Medical shape memory alloy applications-the market and its products. *Mater. Sci. Eng A*, **378**, 16–23.
- Mullins, L. (1948). Effect of stretching on the properties of rubber. *Rubb. Chem. Technol.*, **21**, 281–300.
- Nespoli, A., Dallolio, V., Stortiero, F., Besseghini, S., Passaretti, F., and Villa, E. (2014). Design and thermo-mechanical analysis of a new NiTi shape memory alloy fixing clip. *Mat. Sci. Eng. C*, **37**, 171–176.
- Neuking, K., Abu-Zarifa, A., Youcheu-Kemtchou, S., and Eggeler, G. (2005). Polymer/NiTi-composites: Fundamental aspects, processing and properties. *Adv. Eng. Mater.*, **7**, 1014–1023.
- Neuking, K., Abu-Zarifa, A., and Eggeler, G. (2008). Surface engineering of shape memory alloy/polymer-composites: Improvement of the adhesion between polymers and pseudoelastic shape memory alloys. *Mater. Sci. Eng., A*, **481**, 606–611.
- Oehr, C. (2003). Plasma surface modification of polymers for biomedical use. *Nucl. Instrum. Meth. B*, **208**, 40–47.
- Ogden, R. W. (2003). *Nonlinear elasticity, anisotropy, material stability and residual stresses in soft tissue.*, chapter Holzapfel GA, Ogden RW (eds) Biomechanics of soft tissue in cardiovascular system. CISM Courses and lecture Series, vol 441. Springer, Wien New York.
- Oppenheim, T., Knowles, T., Lacour, S., and Welland, M. (2010). Fabrication and characterisation of protein fibril-elastomer composites. *Acta Biomater.*, **6**, 1337–1341.
- Orgéas, L. (1997). *Etude expérimentale et numérique du comportement thermomécanique d'un alliage à mémoire de forme industriel NiTi.* Ph.D. thesis, Université Joseph Fourier.
- Orgéas, L. and Favier, D. (1998). Stress-induced martensitic transformation of a NiTi alloy in isothermal shear, tension and compression. *Acta Mater.*, **46**, 5579–5591.
- Orgéas, L., Liu, Y., and Favier, D. (1997). Experimental study of mechanical hysteresis of NiTi during ferroelastic and superelastic deformation. *J. Phys. IV*, **7**, 477–482.

- Otsuka, K. and Ren, X. (2005). Physical metallurgy of TiNi-based shape memory alloys. *Prog. Mater. Sci.*, **50**, 511–678.
- Owens, D. and Wendt, R. (1969). Estimation of the surface free energy of polymers. *J. Appl. Polym. Sci.*, **13**, 1741–1747.
- Payandeh, Y., Meraghni, F., Patoor, E., and Eberhardt, A. (2012). Study of the martensitic transformation in NiTi-epoxy smart composite and its effect on the overall behavior. *Mater. Design*, **39**, 104 – 110.
- Payne, A. P. (1962). The dynamic properties of carbon black loaded natural rubber vulcanizates. Part II. *J. Appl. Polym.*, **6**, 368–372.
- Petrini, L. and Migliavacca, F. (2011). Biomedical applications of shape memory alloys. *J. Metal.*, **2011**, ID 501483.
- Rebouah, M. and Chagnon, G. (2013). Permanent set and stress-softening constitutive equation applied to rubber-like materials and soft tissues. *Acta Mech.*, **224**, 1–14.
- Rebouah, M. and Chagnon, G. (2014). Development and modeling of filled silicone architected membranes. *Meccanica*, page submitted.
- Rebouah, M., Machado, G., Chagnon, G., and Favier, D. (2013). Anisotropic modeling of the Mullins effect based on an invariant formulation. *Mech. Res. Commun.*, **49**, 36–43.
- Reese, S. and Govindjee, S. (1998). A theory of finite viscoelasticity and numerical aspects. *Int. J. Solids Struct.*, **35**(26-27), 3455–3482.
- Rendek, M. and Lion, A. (2010). Amplitude dependence of filler-reinforced rubber: Experiments, constitutive modelling and FEM implementation. *Int. J. Solids Struct.*, **47**, 2918–2936.
- Rey, T., Chagnon, G., Le Cam, J.-B., and Favier, D. (2013a). Influence of the temperature on the mechanical behaviour of filled and unfilled silicone rubbers. *Polym. Test.*, **32**, 492–501.
- Rey, T., Chagnon, G., Favier, D., and Le Cam, J.-B. (2013b). Modeling of hysteresis by means of a directional approach. In *Constitutive Models for Rubber VIII*.
- Rey, T., Chagnon, G., Favier, D., and Le Cam, J.-B. (2014a). Hyperelasticity with rate-independent microsphere hysteresis model for rubberlike materials. *Comp. Mater. Sci.*, **90**, 89–98.
- Rey, T., Razan, F., Robin, E., Faure, S., Le Cam, J.-B., Chagnon, G., Girard, A., and Favier, D. (2014b). Mechanical characterization and comparison of different NiTi/silicone rubber interfaces. *Int. J. Adhes. Adhes.*, **48**, 67–74.
- Rey, T., Le Cam, J.-B., Chagnon, G., Favier, D., Rebouah, M., Razan, F., Robin, E., Didier, P., Heller, L., Faure, S., and Janouchova, K. (2014c). An original architected NiTi silicone rubber structure for biomedical applications. *Mat. Sci. Eng. C*, (accepted manuscript).

- Rigbi, Z. (1980). Reinforcement of rubber by carbon black. *Adv. Polym. Sci.*, **36**, 21–68.
- Rogero, S. O., Sousa, J. S., Jr., D. A., Lopérgolo, L., and Lugao, A. B. (2005). Silicone crosslinked by ionizing radiation as potential polymeric matrix for drug delivery. *Nucl. Instrum. Methods Phys. Res., Sect. B.*, **236**, 521–525.
- Rossnagel, S., Cuomo, J., and Westwood, W. (1990). *Handbook of plasma processing technology: fundamentals, etching, deposition, and surface interactions*. Park Ridge, N.J.
- Rothon, R. N. (2001). Particulate fillers for polymers. In *Smithers Rapra Technology*.
- Sadrnezhaad, S., Nemati, N., and Bagheri, R. (2009). Improved adhesion of NiTi wire to silicone matrix for smart composite medical applications. *Mater. Design*, **30**(9), 3667–3672.
- Samaca Martinez, J., Le Cam, J.-B., Balandraud, X., Toussaint, E., and Caillard, J. (2013a). Mechanisms of deformation in crystallizable natural rubber. Part 1: Thermal characterization. *Polymer*, **54**, 2717–2726.
- Samaca Martinez, J., Le Cam, J.-B., Balandraud, X., Toussaint, E., and Caillard, J. (2013b). Mechanisms of deformation in crystallizable natural rubber. Part 2: Quantitative calorimetric analysis. *Polymer*, **54**, 2727–2736.
- Simo, J. (1987). On a fully three-dimensional finite-strain viscoelastic damage model: formulation and computational aspects. *Comput. Methods Appl. Mech. Eng.*, **60**, 153–173.
- Smith, N., Antoun, G., Ellis, A., and Crone, W. (2004). Improved adhesion between nickel–titanium shape memory alloy and a polymer matrix via silane coupling agents. *Compos. Part A-Appl. S.*, **35**, 1307–1312.
- Stathi, K., Tarantili, P. A., and Polyzois, G. (2010). The effect of accelerated ageing on performance properties of addition type silicone biomaterials. *J. Mater. Sci.: Mater. Med.*, **21**, 1403–1411.
- Stevenson, I., David, L., Gauthier, C., Arambourg, L., and Vigier, J. D. G. (2001). Influence of SiO₂ fillers on the irradiation ageing of silicone rubbers. *Polymer*, **42**, 9287–9292.
- Sui, J., Gao, Z., Cai, W., and Zhang, Z. (2007). DLC films fabricated by plasma immersion ion implantation and deposition on the NiTi alloys for improving their corrosion resistance and biocompatibility. *Mater. Sci. Eng., A*, **454**, 472–476.
- Sun, W. S. M. (2005). Finite element implementation of a generalized Fung-elastic constitutive model for planar soft tissues. *Biomech Model Mechanobiol.*, **4**, 190–199.
- Tan, L. and Crone, W. (2002). Surface characterization of NiTi modified by plasma source ion implantation. *Acta Mater.*, **50**, 4449 – 4460.

- Thein-Han, W., Shah, J., and Misra, R. (2009). Superior in vitro biological response and mechanical properties of an implantable nanostructured biomaterial: Nanohydroxyapatite-silicone rubber composite. *Acta Biomater.*, **5**, 2668–2679.
- Ting, J. A. S., Rosario, L. M. D., Lacdan, M. C. C., Lee Jr., H. V., De Vero, J. C., Ramos, H. J., and Tumlos, R. B. (2013). Enhanced adhesion of epoxy-bonded steel surfaces using O₂/Ar microwave plasma treatment. *Int. J. Adhes. Adhes.*, **40**, 64 – 69.
- Tissot, F., Rey, T., Heller, L., Connesson, N., Chagnon, G., Payan, Y., Favier, D., and Sittner, P. (2012). Experiments and modeling of smart silicone elastomer membranes reinforced with shaped NiTi textiles. In *8th EUROMECH - Solid Mechanics Conference*.
- Trabelsi, S., Albouy, P. A., and Rault, J. (2003). Crystallization and melting processes in vulcanized stretched natural rubber. *Macromolecules*, **36**, 7624–7639.
- Treloar, L. R. G. (1943). The elasticity of a network of long chain molecules (I and II). *Trans. Faraday Soc.*, **39**, 36–64 ; 241–246.
- Vandenbroucke, A. (2010). *Etude du comportement mécanique pour différentes températures d'un élastomère : caractérisation expérimentale et numérique*. Ph.D. thesis, Université de Bretagne Sud.
- Vandenbroucke, A., Laurent, H., Aït Hocine, N., and Rio, G. (2010). A hyperelasto-visco-hysteresis model for an elastomeric behaviour: Experimental and numerical investigations. *Comp. Mater. Sci.*, **48**(3), 495–503.
- Wack, B., Terriez, J.-M., and Guélin, P. (1983). A hereditary type, discrete memory, constitutive equation with applications to simple geometries. *Arch. Mech.*, **50**, 9–37.
- Wang, X. and Hu, G. (2005). Stress transfer for a SMA fiber pulled out from an elastic matrix and related bridging effect. *Compos. Part A-Appl. S.*, **36**, 1142 – 1151.
- Winters, H. and Coburn, J. (1992). Surface science aspects of etching reactions. *Surf. Sci. Rep.*, **14**, 161–269.
- Wu, P. and Van der Giessen, E. (1993). On improved network models for rubber elasticity and their applications to orientation hardening in glassy polymers. *J. Mech. Phys. Solids*, **41**(3), 427–456.
- Yeoh, O. H. (1990). Characterization of elastic properties of carbon black filled rubber vulcanizates. *Rubber Chem. Technol.*, **63**(5), 792–805.
- Zéhil, G.-P. and Gavin, H. P. (2013). Unified constitutive modeling of rubber-like materials under diverse loading conditions. *Int. J. Eng. Sci.*, **62**, 90–105.